THE UNIVERSITY OF CHICAGO

RESOURCE-EFFICIENT QUANTUM SIMULATIONS OF LATTICE GAUGE THEORIES

A DISSERTATION SUBMITTED TO
THE FACULTY OF THE DIVISION OF THE PHYSICAL SCIENCES
IN CANDIDACY FOR THE DEGREE OF
DOCTOR OF PHILOSOPHY

DEPARTMENT OF PHYSICS

BY
WANQIANG LIU

CHICAGO, ILLINOIS
JUNE 2025

Copyright © 2025 by Wanqiang Liu

TABLE OF CONTENTS

LIST OF FIGURES v

LIST OF TABLES vii

ACKNOWLEDGMENTS viii

ABSTRACT ix

1 INTRODUCTION 1
- 1.1 Recipes for a quantum computer 3
- 1.2 Towards quantum simulations of lattice gauge theories 8
  - 1.2.1 Representing QFTs with qubits: discretization and digitization 8
  - 1.2.2 Simulating real-time evolutions 10
  - 1.2.3 Initial state preparation 13
  - 1.2.4 Measurement of time-dependent operators 15
  - 1.2.5 Dealing with quantum noise 15

2 RENORMALIZATION OF QUANTUM SIMULATIONS 16
- 2.1 Basics of lattice gauge theories 17
- 2.2 Renormalization of LGTs in classical simulations 22
- 2.3 Trotterization and Time-Evolution 24
- 2.4 The errors of scale-setting in Minkowski metric 29
- 2.5 Numerical Results 34
  - 2.5.1 Scale Setting in Minkowski Spacetime 39
  - 2.5.2 Comparison of Schemes for Scale Setting 40
  - 2.5.3 Approaching the Continuum 44
- 2.6 Continuous limit for discrete group with Wilson action 47
- 2.7 The approximation of truncating at leading order commutators in Eq. (2.38) 51
- 2.8 The proof of the error bound for Scheme B 52
- 2.9 Conclusions 54

3 QUANTUM SIMULATIONS OF IMPROVED HAMILTONIANS 60
- 3.1 Derivation for the improved potential term 63
- 3.2 Circuit Design for improved Hamiltonians 64
- 3.3 Kinetic Term Circuit Derivation 67
- 3.4 Demonstration a real quantum computer 70
- 3.5 Conclusions 73

4 GAUGE SYMMETRY AS QUANTUM ERROR CORRECTION CODES 75
- 4.1 Gauge symmetry and fixing 77
  - 4.1.1 Counting gauge orbits 83
- 4.2 Lattice gauge symmetries as stabilizer codes 85

4.2.1 Stabilizer codes . . . 86
4.2.2 The set of correctable errors . . . 87
4.2.3 Correctability of $\hat{\Gamma}_\sigma$ . . . 90
4.2.4 The encoding and decoding circuits . . . 92
4.2.5 Derivation of Eq. (4.48) in the group element basis . . . 97
4.3 Clebsch-Gordan sum in the group element basis . . . 99
4.4 Comparison of quantum fidelities . . . 101
4.4.1 Group-agnostic thresholds . . . 101
4.4.2 Correctable errors and independence polynomials . . . 103
4.4.3 ϵ, ϵ_c from error models . . . 107
4.5 Conclusions . . . 111

5 OUTLOOK . . . 112

BIBLIOGRAPHY . . . 114

LIST OF FIGURES

1.1 The quantum circuit to produce a maximally entangled state $(|00\rangle + |11\rangle)/\sqrt{2}$ from the computational basis state $|00\rangle$ 5
1.2 Quantum circuits for the time evolution of $\hat{H}_{\rm KS}$. 13

2.1 Schematic relations between Euclidean LGT and quantum simulations. 21
2.2 Ratio of the error bounds of **Scheme B** in Eq. (2.42) to that of **Scheme A** in Eq. (2.41). The black line indicates when the bounds are equal. 33
2.3 The lattice geometry used for the D_4 gauge simulation. The plaquettes are given by $U_2^\dagger U_0^\dagger U_3 U_0$ and $U_3^\dagger U_1^\dagger U_2 U_1$. Dash lines are used to indicate repeated links due to the periodic boundary conditions. 35
2.4 Expectation value of the plaquette $\langle \mathcal{O}_{1\times1}(N\delta_t)\rangle$ vs $N\delta_t$ for different δ_t with fixed $g_H^2 = 1.11$. The green line indicated the $\delta_t \to 0$ exact results 38
2.5 $a_t m_{1\times1}$ vs δ_t for $g_H^2 = 1.25$. The dashed (solid) lines indicate a linear (quadratic) fit to the data. The poor linear fit (χ^2/d.o.f = 40.2) demonstrates that a_t is not proportional to δ_t as might be naively expected. χ^2/d.o.f = 1.1 for the quadratic fit. 41
2.6 $a_t m_{1\times1}$ vs δ_t for different g_H^2. Notice that renormalization of a_t is clearly g_H^2 dependent. 42
2.7 Errors with respect to the truth scale in a Minkowski calculation using **Scheme A** (left) and **Scheme B** (right), with the band showing the error from the 1σ region in the Euclidean fitting. We have assumed that the measurement precision in Euclidean spacetime could reach 1%. Together with fitting errors, we have $\epsilon \leq 2\%$ at 68% C.L. for the g_H^2 and $\delta_\tau = \delta_t$ used in this figure. For **Scheme A** we use $\Delta a_t m_{1\times1}$ from the fit, as ϵ is barely affected by the fitting procedure. . . 57
2.8 $a_t m_{2\times1}/a_t m_{1\times1}$ as a function of $a_t m_{1\times1}$ for a variety of $g_H^2(a, a_t)$. The data points are extracted from fixed δ_t results from a `qasm` calculation. For each g_H^2, we have $\delta_t = \{0.1, 0.25, 0.5\}$ from left to right. The solid lines reflect the best fit for a fixed $g_H^2(a, a_t)$. The colored bands are the 1σ uncertainties on the fits. . . 58
2.9 $a_t m_{2\times1}/a_t m_{1\times1}$ as a function of $a_t m_{1\times1}$ for a variety of $g_H^2(a, a_t)$. The data points are extracted from fixed δ_t results from a `state_vector` calculation. For each g_H^2, we have $\delta_t = \{0.01, 0.05, 0.1\}$ from left to right. The solid lines reflect the best fit for a fixed $g_H^2(a, a_t)$. The colored bands are the 1σ uncertainties on the fits. 59
2.10 $am_{2\times1}/am_{1\times1}$ vs $g_H^2(a, a_t)$ for three continuum trajectories where ξ_t is approximately fixed. Closed and open symbols indicate `qasm` and `state_vector` results respectively. The black line is a best fit to the $\xi = \infty$ points with a 1σ uncertainty band. 59

3.1 3d lattice with example contributions to H_I: the plaquette P_{xy}, rectangles R_{yz} and R_{zx}, and the bent loop C_{xyz}, and the two links U_1 and U_2 used for K_{2L}. . . 62
3.2 Quantum circuits for the time evolution of $\hat{H}_I$. 65

3.3 $\mathcal{U}_{V_{\rm rect}}$ (a) and $\mathcal{U}_{K_{2L}}$ (b) for $\mathbb{Z}_2$ gauge theory. (c) Link-to-qubit map on `ibm_perth`. 70
3.4 $\mathcal{U}_{\rm circ}^{|n\rangle}$ for studying the errors of $\mathcal{U}_{V_{\rm rect}}$. 71
3.5 Probability of measuring Hamming weights for selected $|\Psi_n\rangle$ compared to the noise-dominated results. In the noiseless limit, $P(w_H) = \delta_{w_H,0}$ for all $|\Psi_n\rangle$. . . 73

4.1 Maximal trees (dashed lattice links) of lattices with (left) OBC and (right) PBC. The site at the lower left corner is chosen as the root of the maximal tree. . . . 82
4.2 Schematic circuit of LGT as QEC. **g** represents a color-neutral state. 85
4.3 Examples of correctable error distributed on the lattice to satisfy the MED (upper-right) or the local KL condition (lower-left). The orange links are Γ-type errors, which must break gauge symmetry at the orange squares. The conditions require the green links to be error-less. For the MED condition, the adjacent sites (blue circles) must be charge-neutral. For the local KL condition, the error links are allowed to extend in a straight line, which is the shortest path to connect a pair of charges. 91
4.4 Encoding and decoding circuits for the patch in Fig. 4.1. (top) Circuit for preparing gauge-invariant states, and (bottom) Gauss's law measurement and recovery circuit, where measuring a pair of charges $\sigma, \bar{\sigma}$ on the two ancillae indicates a gauge-violating error on $|U_2\rangle$. 96
4.5 Quantum circuits implementing Clebsch-Gordan sums for generic finite groups. (left) $\mathfrak{U}_{CG}^{L}$ and (right) $\mathfrak{U}_{CG}^{R}$ 99
4.6 Error threshold lines in the $\epsilon - \epsilon_c/\epsilon$ plane below which $F_{\rm restored} > F_{\rm fixed}$, indicating that using gauge redundancy to detect and correct the errors is advantageous, for 2d lattices for (top) MED condition and (bottom) local KL condition. The shaded region is the infinite volume limit. 104
4.7 Error threshold lines in the $\epsilon - \epsilon_c/\epsilon$ plane below which $F_{\rm restored} > F_{\rm fixed}$, indicating that using gauge redundancy to detect and correct the errors is advantageous, for 3d lattices for (top) MED condition and (bottom) local KL condition. 105

LIST OF TABLES

1.1 The definition and notation of some frequently used gates. A single line in the notations denotes a qubit in circuit diagrams 6

1.2 Primitive gates to construct the quantum circuits for the time evolution of generic gauge theories, with examples for the Z_2 group. 12

2.1 Benchmark values for D_4 models in $2+1D$ and $3+1D$ with periodic conditions. Assuming $\epsilon = 0.02$ and demanding the errors in Eq. (2.41) and Eq. (2.42) to be below 0.1, δ_t^A, δ_t^B are largest possible δ_t for **Scheme A** and **Scheme B**. When $g_H^2 = 0.1$, $M < 0.1$ and we take $\delta_t^A = \delta_t^B = \max \delta$. The first three rows use the same parameters as in Fig. 2.7. The absolute error in Tab. 2.1 can be converted to the relative error in Fig. 2.7 by use of a factor $\delta_t / a_t m_{1\times 1} \approx 1$ from Tab. 2.2. . 34

2.2 Numerical results for lattice masses $a_t m_{1\times 1}$ and $a_t m_{2\times 1}$ for the bare couplings g_H^2 and δ_t studied here. Rows above (below) the line indicate `qasm` (`state_vector`) results. 56

2.3 Numerical results for the dimensionless ratio of lattice masses $a_t m_{2\times 1}/a_t m_{1\times 1}$ after extrapolating for fixed g_H^2 to the Hamiltonian limit, in comparison with the same quantities calculated using direct diagonalization of $V_{\rm KS} + K_{\rm KS}$. Rows above (below) the line indicate `qasm` (`state_vector`) results. 58

3.1 Number of primitive gates per link register per trotter step neglecting boundary effects (columns 2-3), implementation for $\mathbb{Z}_2$ (last column). 67

3.2 Measured state-dependent quantum fidelities with Pauli twirling and without it for $|\Psi_6\rangle_{\rm no\,PT}$. 72

4.1 The number of degrees of freedom in a lattice with L links per side in d dimensions. $b = 0, 1$ for PBC and OBC respectively. 83

4.2 Correctable errors $\hat{\Gamma}_\sigma$ for the quaternion group $\mathbb{Q}_8$ encoded in 3 qubits via $(-1)^a \mathbf{i}^b \mathbf{j}^c \to |abc\rangle$. 110

ACKNOWLEDGMENTS

First and foremost, I thank my advisor Marcela Carena for introducing me to the exhilarating research in the intersection of particle physics and quantum computing and for leading the research community in this frontier. The thesis research is supported by Department of Energy through the Fermilab QuantiSED program in the area of "Intersections of QIS and Theoretical Particle Physics". It has been a great pleasure working with my mentors and collaborators in Fermilab, Hank Lamm and Ying-Ying Li, and I cannot thank you enough for the projects and memories we have created together.

I would like to thank the other members of my thesis committee, Peter Littlewood, Linda Young, and LianTao Wang. I thank the support and education from the Department of Physics at the University of Chicago.

Thank you to scientists and friends in the Fermilab theory group, Roni Harnik, Erik Gustafson, Ruth Van de Water, Hersh Singh, Innes Bigaran, Arushi Bodas, and Judah Unmuth-Yockey for your warmest welcome and enthusiastic discussions.

Thank you to my dear friends Rayne Liu and Zhaoning Liu. You have been my family in the past few years, half the world away from my original family.

Thank you to my partner Seth Koren.

Last but no the least, I would like to thank my mother and my first teacher Mi Qin.

ABSTRACT

Future large-scale quantum computers (QCs) can be a revolutionary tool for first-principle calculations in strongly coupled quantum field theories, which are essential in many scenarios in particle physics. Meanwhile, due to the unique features of our problems, many theoretical and algorithmic challenges need to be addressed before particle physics can take advantage of the ongoing quantum revolution. This thesis discusses how to efficiently utilize QCs for real-time simulations of gauge interactions in quantum field theories, focusing on two aspects.

The first aspect is the reduction of space-time discretization errors via renormalization and improved Hamiltonians. We show that trotterization entails renormalization of the temporal and spatial lattice spacings. Based on the tools of Euclidean lattice field theory, we propose two schemes to determine Minkowski lattice spacings, using Euclidean data and thereby overcoming the demands on quantum resources for scale setting. In addition, Hamiltonians with improved discretization errors will reduce the number of qubits required by a factor of $\gtrsim 2^d$ in quantum simulations for lattices with d spatial dimensions. We consider $\mathcal{O}(a^2)$-improved Hamiltonians for pure gauge theories and design the corresponding quantum circuits for its real-time evolution in terms of primitive gates. Numerical demonstrations with real and classically simulated quantum computers are included.

The second aspect concerns gauge symmetries, which can be either fixed or encoded as a redundancy of the Hilbert space in quantum simulations. While gauge-fixing reduces the number of qubits, keeping the gauge redundancy enables quantum error corrections by checking and restoring Gauss's law. In this work, we consider generic finite gauge groups and design the quantum circuits to detect and correct the symmetry-violating errors. We calculate the error thresholds below which the gauge-redundant digitization with Gauss's law error correction has better fidelity than the gauge-fixed digitization. Our results provide guidance for fault-tolerant quantum simulations of lattice gauge theories.

CHAPTER 1

INTRODUCTION

Quantum field theories (QFTs) provide us with the most successful tools to describe and predict microscopic Nature. However, their rich structures also pose serious computational challenges, especially in the strongly coupled theories where perturbative methods are not applicable. To date, lattice field theories (LFTs) in Euclidean spacetime are the essential method in making predictions with strongly-coupled quantum field theories. In LFTs, the target is to compute the expectation values of operators

$$\langle O \rangle = Z^{-1} \int D\phi \, e^{-S_E(\phi)} O(\phi), \tag{1.1}$$

where S_E is the Euclidean action. Stochastic samples of the fields on spacetime lattices are created via Monte Carlo methods, according to the Boltzmann weight e^{-S_E}. Then the expectation values of operators are calculated among the samples. With N_s samples, the precision ϵ of the expectation values typically improves as $1/\sqrt{N_s}$. This enables reliable calculations of observables with sample numbers $N_s \sim \epsilon^{-2}$, far smaller than the dimension of the Hilbert space that grows exponentially with the size of the system.

However, LFTs on classical computers meet inherent obstacles in two types of problems. One type involves real-time dynamics, such as out-of-equilibrium evolution in the early universe [1–4], transport coefficients of the quark-gluon plasma [5] and parton physics in hadron collisions [6–11]. They require real-time correlators such as

$$C_{AB}(t) = \langle A(t)B(0) \rangle = Z^{-1} \int D\phi \, e^{iS_M(\phi)} A(\phi_t) B(\phi_0), \tag{1.2}$$

where S_M is the Minkowski action, and ϕ_0, ϕ_t are the field values at real times 0 and t. The real-time path integral cannot be calculated directly with the Monte Carlo method since the weight e^{iS_M} is complex. This is the *dynamical sign problem* . The other class is the *fermionic*

sign problem, which requires calculations at a finite fermion chemical potential, which causes the effective action to have an imaginary part and thus the Euclidean probability amplitude e^{-S_E} to be complex [12–14]. The search for efficient solutions to sign problems is very active in the field of LGTs. Within the means of classical computations, some promising methods are being developed to suit specific calculations with sign problems, including analytic continuations that work for small real time and chemical potentials, the large-momentum effective field theory for parton distribution functions [15], reweighing methods [16], and contour deformations [17, 18] to optimize calculations at finite fermion chemical potentials.

Meanwhile, future, large-scale quantum computers (QCs) can provide a more universal solution. For a lattice in d spatial dimensions with L lattice sites in each direction, and a m-level system at every site, the wave function consists of m^{L^d} complex numbers. Therefore, in most classical methods, directly solving the Hamiltonian evolution $|\psi(t)\rangle = e^{-iHt}\,|\psi(0)\rangle$ is not realistic due to the exponential scaling of the dimension of the Hilbert space with the size of the system. QCs store the information in the wavefunction of qubits, the dimension of which also scales exponentially with the number of qubits. Thus, the number of qubits required to represent the Hilbert space of LFTs scales linearly with the spatial volume L^d. Provided that the unitary operator e^{iHt} can be performed efficiently on such states, QCs avoid the dynamical sign problem by directly simulating real-time evolutions in the Hamiltonian formalism. [19–23]. The quantum simulations can also include the fermion degrees of freedom by matching them to qubits, with additional dressing such as the Jordan-Wigner transform to implement the anti-commutation. [24] This avoids the fermionic sign problem as one can directly implement the chemical potential [25].

For now, quantum computers are limited to hundreds of non-error-corrected qubits with circuit depths less than 1000 gates– the so-called Noisy Intermediate-Scale Quantum (NISQ) era. Despite this, toy calculations in high energy physics [26–34] and nuclear physics [35–37] have been performed using existing quantum computers, representing the first step towards

quantum simulating field theories.

Even if a beyond-NISQ computer were available tomorrow, it would not be immediately clear how to utilize it for problems in strongly-coupled quantum systems that are relevant to particle physics. To take advantage of the advancement of QCs, there are theoretical and algorithmic challenges. This thesis covers recent original efforts tackling these challenges. The rest of this chapter provides an introduction to quantum computing and its applications to lattice gauge theories in the Hamiltonian formalism.

1.1 Recipes for a quantum computer

What is a quantum computer? Roughly speaking,it is a quantum system that obeys commands and performs computations in its Hilbert space. A more descriptive answer is DiVincenzo's five criteria for any quantum system to be a quantum computer [38] . Here I briefly review the criteria along with some experimental realizations and introduce important concepts. Most of the definitions and theorems can be found in [39].

(1) It is a quantum system with a definite number of degrees of freedom. Each degree of freedom has two or more quantum levels; it is called a *qubit* or *qudit* respectively. Physically, it can be a superconducting circuit, an ion or neutral atom trapped by electromagnetic fields, or a photon. For every physical system there exist some well-defined quantum numbers, the eigenbasis of which is usually referred to as the *computational basis* with the labels $|0\rangle, \ldots |d_q - 1\rangle$ for where d_q is the dimension of the qudit). In superconducting circuits, the quantum numbers can be the charge in a capacitor, the magnetic flux, or the electric current. Trapped ion or neutral atom systems utilize the energy levels of the particles.

Ideally, we want to scale up the number of qubit or qudits. With n qubits, the dimension of the Hilbert space is 2^n. The data is stored as the wavefunction

$$|\varphi\rangle = \varphi_0 |0 \ldots 0\rangle + \cdots + \varphi_{2^n-1} |1 \ldots 1\rangle , \tag{1.3}$$

where $|0\ldots0\rangle$ stands for the tensor product state of n qubits $|0\rangle \otimes \cdots \otimes |0\rangle$, and similarly for the other basis states.

In trapped ion systems, a limiting factor for n is the number of particles that can be reliably kept in a trap, which is on the order of hundreds in the state-of-art experiments to date [40]. Similarly for superconducting circuit systems, the number of qubits that can exist on one chip is also limited to similar orders of magnitude. To scale beyond $O(10^3)$ qubits, *quantum networking* is a promising paradigm. It distributes the qubits to a number of different chips or traps, with means of quantum communication among them [41, 42].

(2) The system can be initialized to a fiducial state, such as $|0\ldots0\rangle$ in the computational basis. In principle, this can be achieved by cooling the system to the ground state. Other device-dependent techniques can be more efficient. The state *fidelity* is defined as

$$\mathcal{F}(\rho) = \langle\psi|\,\rho\,|\psi\rangle\,, \tag{1.4}$$

where ρ is the density matrix of the realistic state of the system and $|\psi\rangle$ is the fiducial state.

(3) The system can perform unitary evolutions as one demands. In digital quantum computers, this is achieved by the application of *quantum gates*–some elementary unitary operators that involve a small number of qubits. Some frequently used gates are listed in Tab. 1.1. More complicated unitary operators can be achieved by applying such elementary operators in sequence and in parallel, which is often denoted as *quantum circuits*.

An essential step towards this criterion is to entangle arbitrary pairs of qubits, which can be achieved via the circuit in Fig. 1.1. The Hadamard gate turns the computational basis state $|0\rangle$ into the quantum superposition $(|0\rangle + |1\rangle)/\sqrt{2}$; then the `CNOT` creates a Bell pair $(|00\rangle + |11\rangle)/\sqrt{2}$. It exhibits non-classical behavior and is the foundation of quantum cryptography. Currently, it is often the ability to entangle the qubits that limits the size of the QCs.

However, creating entanglement alone is not yet enough for QCs to achieve advantages

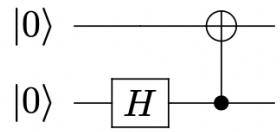

Figure 1.1: The quantum circuit to produce a maximally entangled state $(|00\rangle + |11\rangle)/\sqrt{2}$ from the computational basis state $|00\rangle$

over classical computers. An example is the *Clifford gates* that are generated by the set {`H, S, CNOT`}. Despite the ability of Clifford gates to entangle qubits, it only takes polynomial space and time for classical computers to simulate any quantum circuits composed solely of them. This is the *Gottesman-Knill theorem*. To create quantum circuits that cannot be simulated efficiently on classical computers, a *universal quantum gate set* is needed. A set of gates is *universal* if the quantum circuits that are composed of them can arbitrarily well approximate any unitary operator. The Clifford gate with the addition of any non-Clifford gate form a universal set. Examples of universal quantum gate sets are Clifford+`T` or Clifford + `CCNOT`. Further, the Solovay–Kitaev theorem guarantees that such approximations are efficient: for quantum circuits composed of any universal gate set, it takes at most $O(\log^c \epsilon)$ gates to approximate arbitrary unitary operators on one qubit with ϵ precision, where c is a constant smaller than 4. See [43] for a pedagogical review.

In NISQ computers, the multi-qubit gates are less reliable than the single-qubit gates; thus the number of `CNOT` gates is often limiting factor for the realistic implementation of quantum circuits.

(4) The qubits must be able to stay in quantum superpositions for a long enough time to perform the calculations. *Decoherence* is the process that a quantum system loses its information to the environment. This can happen in the form of the spontaneous decay to the ground state or a random state dominated by noise, or the loss of a qubit. To achieve long coherence time, the qubits must be in a low-noise physical environment.

Quantum error correction (QEC) codes can be used in such low-noise environment to

Name	Notation in circuit diagrams	Matrix
Pauli-X (X)	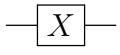	$\begin{pmatrix} 0 & 1 \\ 1 & 0 \end{pmatrix}$
Pauli-Y (Y)	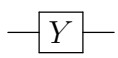	$\begin{pmatrix} 0 & -i \\ i & 0 \end{pmatrix}$
Pauli-Z (Z)	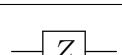	$\begin{pmatrix} 1 & 0 \\ 0 & -1 \end{pmatrix}$
Hadamard (H)	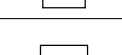	$\frac{1}{\sqrt{2}}\begin{pmatrix} 1 & 1 \\ 1 & -1 \end{pmatrix}$
Phase (S)	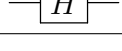	$\begin{pmatrix} 1 & 0 \\ 0 & i \end{pmatrix}$
$\pi/8$-gate (T)	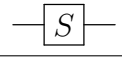	$\begin{pmatrix} 1 & 0 \\ 0 & e^{i\pi/4} \end{pmatrix}$
Z-rotation gate	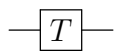	$\begin{pmatrix} e^{i\theta/2} & 0 \\ 0 & e^{-i\theta/2} \end{pmatrix}$
CNOT		$\begin{pmatrix} 1 & 0 & 0 & 0 \\ 0 & 1 & 0 & 0 \\ 0 & 0 & 0 & 1 \\ 0 & 0 & 1 & 0 \end{pmatrix}$
SWAP		$\begin{pmatrix} 1 & 0 & 0 & 0 \\ 0 & 0 & 1 & 0 \\ 0 & 1 & 0 & 0 \\ 0 & 0 & 0 & 1 \end{pmatrix}$
Toffoli (CCNOT)		$\begin{pmatrix} 1 & 0 & 0 & 0 & 0 & 0 & 0 & 0 \\ 0 & 1 & 0 & 0 & 0 & 0 & 0 & 0 \\ 0 & 0 & 1 & 0 & 0 & 0 & 0 & 0 \\ 0 & 0 & 0 & 1 & 0 & 0 & 0 & 0 \\ 0 & 0 & 0 & 0 & 1 & 0 & 0 & 0 \\ 0 & 0 & 0 & 0 & 0 & 1 & 0 & 0 \\ 0 & 0 & 0 & 0 & 0 & 0 & 0 & 1 \\ 0 & 0 & 0 & 0 & 0 & 0 & 1 & 0 \end{pmatrix}$

Table 1.1: The definition and notation of some frequently used gates. A single line in the notations denotes a qubit in circuit diagrams .

facilitate fault-tolerant quantum computations. QEC deliberately designs a redundant full Hilbert space $\mathcal{H}_{\text{full}}$ on the physical qubits and encodes quantum information in a much smaller code subspace $\mathcal{H}_{\text{code}}$ on logical qubits with certain symmetries, thus allowing for correction without disrupting the coherent quantum information in $\mathcal{H}_{\text{code}}$ [44, 45]. As an active field of research, estimates for the overhead – the physical to logical qubit ratio – vary from $\mathcal{O}(10)$ to $\mathcal{O}(10^5)$ [46–48]. Currently with NISQ computers, there are methods to mitigate errors and improve the accuracy under the limitations of the current coherence time and physical noise level. Quantum error mitigation (QEM) uses the existing symmetries without introducing redundancy to mitigate errors [49]. The topics of quantum error correction and mitigation will be discussed in more details in Chapter 4.

(5) The quantum states can be measured in the computational basis. For a quantum state like Eq. (1.3), the measurement process reads out a string of qubits $q_1 q_2 \dots q_n$ with the probability $|\varphi_i|^2$, where $q_1 q_2 \dots q_n$ is the binary format of i. This is the "strong measurement" in quantum mechanics in the sense that it completely collapses the state.

If quantum systems that meet all the above criteria are available, what are they useful for? Theoretically, it is conjectured that QCs can break the complexity hierarchy of classical computations by introducing the class of bounded-error quantum polynomial-time (BQP) problems, which are solvable by QCs in polynomial time with bounded error probabilities. In practice, it is not trivial to identify problems in the BQP class that also take exponential space or time on classical computers. Thus the current opinion regarding the utilization of QCs is to use them as accelerators to tackle certain hard problems, instead of universal machines to replace classical computers.

Among the conjectured BQP problems, *quantum simulation*– the prediction of microscopic phenomena based on quantum mechanics is arguably the most straightforward application. Indeed, it is exactly this problem that motivated the proposal of QCs by Feynman[19]. In classical computations, the number of classical bits required to store a many-body quan-

tum wavefunction scales exponentially with the number of particles. In a QC, the Hilbert space of the target system is be represented by that of the qubits; the number of qubits scales linearly with the number of quantum particles. The dynamical evolution of the target system is a unitary operator e^{iHt}, which can be realized as a quantum circuit in the QC. The initialization and measurement needs extra attention, as we usually need to initialize and measure states in a basis different from the computational basis. Thus, we also need to design and implement the transformations between the computational basis and the ones of our interest.

1.2 Towards quantum simulations of lattice gauge theories

In the application of quantum simulation to problems in strongly-interacting quantum field theories, one long-term goal is the real-time dynamics of quantum chromo dynamics (QCD) – the interaction of quarks (fermions) and gluons ($SU(3)$ gauge bosons). This section reviews the generic formalism and challenges as the background for the main contents of this thesis, published in [50–52], and outlines their contribution to the bigger picture.

1.2.1 Representing QFTs with qubits: discretization and digitization

Following LGTs on classical computers, we approximate the continuous space as spatial lattices, with matter fields on the vertices and gauge fields on the links. To maintain gauge-symmetries, we construct the lattice Hamiltonians with Wilson lines on the links:

$$U_{\mathbf{x},i} = \mathbf{P} \exp\left(-i \int_{\mathbf{x}}^{\mathbf{x}+\mathbf{i}} d\mathbf{l} \cdot \mathbf{A} \right) \approx e^{-iaA_i(\mathbf{x})}, \tag{1.5}$$

where $A_i(\mathbf{x})$ is the vector potential and $\mathbf{P}$ represents path ordering. In terms of the color components in non-Abelian gauge theories, $A_i(\mathbf{x}) = A_i(\mathbf{x})^b \lambda_b$, with λ_b being generators of the gauge group. Thus, $U_{\mathbf{x},i}$ is an element of the gauge group G that corresponds to the

gauge parallel transport from the lattice site $\mathbf{x}$ to its neighbor $\mathbf{x}+\mathbf{i}$. The group elements form a complete basis of the local Hilbert space on each lattice link:

$$\mathcal{H}^G_{\text{link}} = \text{span}\{|U\rangle, U \in G\}. \tag{1.6}$$

We refer to the set of qubits (qudits) that store a group element as a *link register*. For continuous groups such as $U(N), SU(N)$, the dimension of $\mathcal{H}^G_{\text{link}}$ is infinite. In quantum simulations, the local degrees of freedom need to be matched to a finite number of qubits. This matching is the *digitization* of quantum fields. To digitize the link variables, it is sometimes useful to consider the group representation basis, $|\sigma_{mn}\rangle$, which is the group Fourier transform of the group element basis:

$$\langle \sigma_{mn}|U\rangle = \sqrt{d_\sigma/|G|}\Gamma^{(\sigma)}_{mn}(U), \tag{1.7}$$

where $\Gamma^{(\sigma)}_{mn}(U)$ is the m,n matrix element of the unitary irreducible representation (irrep) σ for U, d_σ is the dimension of σ.

For a continuous compact group G, the representation basis is discrete but infinite. One can truncate the infinite tower of representations to match them to a finite number of qubits. Another common method is to use a finite subgroup of G as an approximation. In this way, both the group element basis and the group representation basis are finite and discrete, and the exact subgroup gauge symmetry is kept. To approximate the $SU(3)$ group of strong interaction, the largest "crystal-like" subgroup has 1080 elements, which are evenly distributed in the group manifold of $SU(3)$ [53]. Thus it takes 11 qubits to approximate one link variable. Understanding the theoretical errors introduced by various digitization methods is an area of active research [54–61]. In Chapter 4, I discuss one such aspect that is gauge symmetry breaking.

For lattice fermions, the number of particles is limited by the Pauli exclusion principle.

Thus, we can naturally assign at each lattice site one qubit per spin and flavor to represent whether the state is occupied. To implement the anti-commutation relations, extra steps are needed in mapping between fermion operators and qubit operators. The Jordan-Wigner transformation [62], the most widely known method, is highly efficient in $1+1$ dimensions, but introduces nonlocal qubit operators in higher dimensions. To address this problem, there are other methods such as the Bravyi-Kitaev method and Bosonization. [63, 64]. Further proposals discuss how to map lattice fermions (e.g. Wilson and staggered) onto these encodings [65]. Alternatively, one can use gauge symmetry to eliminate the fermions [66, 67]. The relative merits of each are only starting to be understood.

The number of qubits is proportional to $(L/a)^d$ for a d spatial dimensional lattice of length L and lattice spacing a. A Hamiltonian $\hat{H}$ constructed at finite lattice spacing a introduces discretization errors compared to the continuum theory in positive powers of a. Crucially, the lattice spacing a is not known a priori, but calculated via the *scale setting* process by comparing observables such as particle masses on lattices with their physical counterparts measured in real experiments. Scale setting is a standard step in LGTs on classical computers to obtain physical observables. The continuum limit can be obtained via the extrapolation toward the $a \to 0$ limit from a series of calculations at different finite lattice spacings. Chapter 2 adapts scale setting and the continuum extrapolation methods to quantum simulations and proposes methods of using classical calculations to assist the scale setting on quantum computers.

1.2.2 Simulating real-time evolutions

The digitization of QFTs naturally induces a mapping from the Hamiltonian of QFTs to qubit operators. To study the full QCD, the Hamiltonian consists of the pure gauge field energy H_{gauge}, the mass term for the matter field H_m, and the gauge-matter coupling terms H_I. For H_{gauge}, most quantum simulations implement the Kogut-Susskind Hamiltonian

[68] formulated with the link variables Eq. (1.5):

$$H_{\mathrm{KS}} = K_{\mathrm{KS}} + V_{\mathrm{KS}}, \tag{1.8}$$
$$K_{\mathrm{KS}} = \sum_{\mathbf{x},i} \frac{g_t^2}{a} \operatorname{Tr} L_i^2(\mathbf{x}),\ V_{\mathrm{KS}} = -\sum_{\mathbf{x},i<j} \frac{2}{g_s^2 a} \operatorname{Re}\operatorname{Tr} P_{ij}(\mathbf{x}).$$

where $L_i(\mathbf{x})$, the lattice electric field operator, is the conjugate momentum operator of $A_i(\mathbf{x})$; the plaquette operator $P_{ij}(\mathbf{x})$ is path-ordered the product of the link variables around the 1×1 square:

$$P_{ij(\mathbf{x})} = U_{\mathbf{x},j}^{-1} U_{\mathbf{x}+\mathbf{j},i}^{-1} U_{\mathbf{x}+\mathbf{i},j} U_{\mathbf{x},i}. \tag{1.9}$$

As temporal and spatial directions are treated differently, coupling g_t and g_s are introduced for the kinetic term K_{KS} and potential term V_{KS}, respectively. In the limit $a \to 0$, H_{KS} approaches the continuous Yang-Mills Hamiltonian, with K_{KS} approximating the electric energy density and V_{KS} approximating the magnetic energy density.

Propagating for a time t requires the unitary operator of $\mathcal{U}(t) = e^{-iHt}$ – a generically dense matrix – which cannot be efficiently constructed on a quantum computer. Instead, it must be approximated in digital quantum simulations. A common method is trotter approximation, which breaks down a long-time evolution into small steps and uses the product formula to approximate each step. For some H, this allows for efficient simulations [20, 69–77]. In the case of H_{KS}, the one-step evolution in the first-order approximation is

$$U(a_t) = \mathcal{U}_{K_{\mathrm{KS}}} \mathcal{U}_{V_{\mathrm{KS}}},\ \mathcal{U}_{K_{\mathrm{KS}}} = e^{-ia_t K_{\mathrm{KS}}},\ \mathcal{U}_{V_{\mathrm{KS}}} = e^{-ia_t V_{\mathrm{KS}}}, \tag{1.10}$$

where $a_t = t/N$ is the size of one time step and N is the number of steps. This approximates $\mathcal{U}(t) \approx U(a_t)^N$ with trotter errors that are proportional to a_t and vanish in the limit $N \to \infty$.

The implementation of $U(a_t)$ in digital quantum computers benefits from the fact that V_{KS} and K_{KS} are diagonal in the group element basis and the group representation basis,

respectively, and that the quantum group Fourier transformation between the two basis can be realized efficiently. For the Abelian group Z_{2^n}, the quantum Fourier transformation is the famous quantum adaptation of the classical fast Fourier transform algorithm [78, 79]. Similar quantum algorithms have been developed for non-Abelian groups [80, 81].

To formulate quantum simulation algorithms of gauge theories in a hardware-agnostic way, we define the following set of primitive gates on link registers, and build quantum circuits from them [82]. Apart from the Fourier transform, we also need the gates $\mathfrak{U}_{\times}^{L,R}$ to perform group multiplications, $\mathfrak{U}_{\mathrm{Tr}}$ and $\mathfrak{U}_{\mathrm{phase}}(\theta)$ to rotate by diagonal phases according to the magnetic or electric energy in their eigenbasis respectively, and $\mathfrak{U}_{-1}$ to inverse the group elements. The definitions of these primitive gates are listed in Tab. 1.2. For the Z_2 theory, they have straightforward correspondence with the one-qubit or two-qubit gates listed in Tab. 1.1. For bigger groups, the primitive gates are usually multi-qubit operators, which can be synthesized with the universal gate set.

Name	Definition	Z_2 example
left and right multiplication gates	$\mathfrak{U}_{\times}^{L}\lvert U_i\rangle\lvert U_j\rangle = \lvert U_i\rangle\lvert U_iU_j\rangle$, $\mathfrak{U}_{\times}^{R}\lvert U_i\rangle\lvert U_j\rangle = \lvert U_i\rangle\lvert U_jU_i\rangle$	CNOT
trace gate	$\mathfrak{U}_{\mathrm{Tr}}(\theta)\lvert U\rangle = e^{i\theta\,\mathrm{Re}\,\mathrm{Tr}\,U}\lvert U\rangle$	$R_Z(\theta)$
Fourier gate	$\mathfrak{U}_F\lvert U\rangle = \sum_{\sigma,m,n}\sqrt{d_\sigma/\lvert G\rvert}\Gamma^{(\sigma)}_{mn}(U)\lvert\sigma_{mn}\rangle$	Hadamard
L-phase gate	$\mathfrak{U}_{\mathrm{phase}}(\theta)\lvert\sigma_{mn}\rangle = e^{i\theta f(\sigma)}\lvert\sigma_{mn}\rangle$	$R_Z(\theta)$
inverse gate	$\mathfrak{U}_{-1}\lvert U\rangle = \lvert U^{-1}\rangle$	Identity ($\mathbb{I}$)

Table 1.2: Primitive gates to construct the quantum circuits for the time evolution of generic gauge theories, with examples for the Z_2 group.

With these primitive gates, we can construct the circuits in Fig. 1.2a and Fig. 1.2b to implement the one-step unitary operators $\mathcal{U}_{V_{\mathrm{KS}}}$ and $\mathcal{U}_{K_{\mathrm{KS}}}$. For $\mathcal{U}_{V_{\mathrm{KS}}}$, we use the inverse gates and group multiplication gates to compute the plaquette group element P_{ij} Eq. (1.9) on one of the four links, then use the trace gate to perform the unitary evolution with the magnetic energy, and finally un-compute the multiplications to return to the original group elements

on each link. For $\mathcal{U}_{K_{\rm KS}}$, we use the Fourier gate to transform to the group representation basis, and use the L-phase gate to perform the unitary evolution with the electric energy.

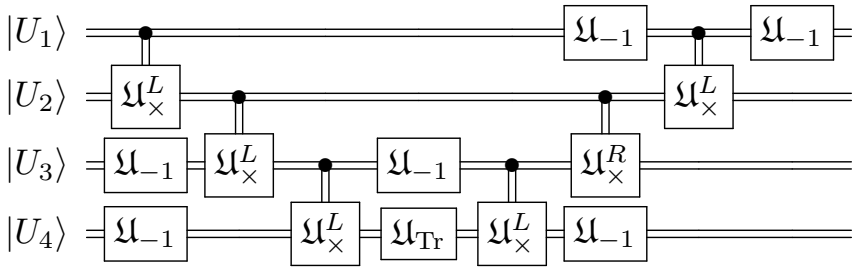

(a) $\mathcal{U}_{V_{\rm KS}}$ assuming linear register connectivity.

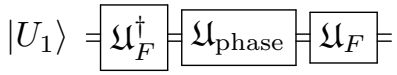

(b) $\mathcal{U}_{K_{\rm KS}}$.

Figure 1.2: Quantum circuits for the time evolution of $\hat{H}_{\rm KS}$.

At finite a, $H_{\rm KS}$ has discretization errors that scale as a^2. By introducing counter-terms to cancel the leading order errors, improved Hamiltonians have discretization errors that scale as a^4 [83, 84]. Chapter 3 studies the implementation of such improved Hamiltonians and their efficiency in saving quantum resources.

Besides trotterization, there are other approximations of $\mathcal{U}(t)$, such as random compilers (QDrift) [85], variational approaches [86–88], Taylor series [89], and qubitization [90]. Although these methods sometimes have better formal bounds for the approximation errors, the errors of trotterization have a clear physical interpretation and correspondence with Euclidean LGTs, which will be discussed in Chapter 2.

1.2.3 Initial state preparation

Typically, we are interested in time evolution of the low-energy subspace in the very high-dimensional Hilbert space of strongly interacting theories. In most digitizations, such states

correspond to highly entangled states in QCs. Thus, initializing such states can be an obstacle. In addition, it is an interesting and significant task to obtain the ground states of Hamiltonians in many scenarios.

Most intuitively, there is the Adiabatic Quantum Computation (AQC). In the parameter region where one type of local operators that mutually commute dominate the Hamiltonian, the ground state of the theory is simply the tensor product state of such local operators. For H_{KS}, the limit of $g \to \infty$ is dominated by the electric operator, and thus the ground state is the tensor product state where all the links are in the ground state of L^2. Thus, it can be prepared with shallow quantum circuits. AQC starts with a product state that is the ground state of $H(\lambda_0)$ and performs unitary evolutions with slowly changing parameters λ_t:

$$i\frac{d}{dt}\left|\psi(t)\right\rangle = H(\lambda_t)\left|\psi(t)\right\rangle . \tag{1.11}$$

According to the adiabatic theorem, $|\psi(t)\rangle$ remains the ground state of the instantaneous Hamiltonian $H(\lambda_t)$ when λ_t changes sufficiently slowly with t. The benefit of AQC is that the circuit is entirely unitary and can be easily designed with the approximation methods in the previous section. However, it requires very deep circuits, which is a big challenge in the NISQ era. [91–93]

To adapt to NISQ devices, there are quantum-classical hybrid methods such as Variation Quantum Eigensolver (VQE). In VQE, one uses finite-depth circuits that are parametrized with a certain ansatz, measures the energy of the outcome states, and then optimizes the parameters with classical computation. Thus, a good ansatz is crucial to the success in obtaining the ground state. [27, 94–96] In addition, there are methods based on Quantum Signal Processing (QSP) that use projection operators to reduce the circuit depth required for the preparation of low energy states. [97, 98]. Further, thermal and particle states have been investigated [3, 20, 29, 32, 33, 69–73, 99–106].

1.2.4 Measurement of time-dependent operators

Once we obtain the time-dependent quantum states $|\psi(t)\rangle$, the measurement of instantaneous hermitian operators simply involves reading out the quantum states in the eigenbasis of the observables. The expectation value is then calculated as the average over multiple measurements:

$$\langle \hat{A}(t) \rangle = \sum_n p_n(t) A_n, \tag{1.12}$$

where p_n is the statistical probability of reading out the computational basis state $|n\rangle$ which corresponds to the eigenvector with eigenvalue A_n. To achieve accuracy ϵ for the expectation value, the number of independent measurements is $O(\epsilon^{-2})$.

Observables dependent on time-separated operators, which are required for parton distribution functions [6–8], particle decays [107], and viscosity [5]) are more complicated. Naively, the first measurement collapses the state, preventing further evolution. Ways to overcome this include ancillary probe-and-control qubits [6, 82, 101, 108, 109] and phase estimation [36, 94].

1.2.5 Dealing with quantum noise

To achieve realistic quantum simulations, noise on the devices needs to be corrected or mitigated. Noisy quantum devices can also be viewed as introducing new operators. The best-studied examples of this are related to gauge-violating operators [110–121]. Which operators are introduced and which symmetries are broken are both hardware and digitization dependent. How to correct and mitigate errors in quantum simulations is an important open question. Chapter 4 uses the similarity between gauge symmetries and QEC codes to detect and correct gauge-symmetry violating errors, and discusses the condition under which such error corrections are advantageous.

CHAPTER 2

RENORMALIZATION OF QUANTUM SIMULATIONS

In this chapter we investigate the renormalization of LGT in Minkoswki spacetime due to trotterizing $\mathcal{U}(t)$. The consequence of this will be shown to be the introduction of a temporal lattice spacing, and new operators depending upon it which vanish in the Hamiltonian limit.

In the continuum limit, Minkowski and Euclidean results are the analytic continuation of each other [122–124]. At finite a_t and finite statistics, this exact relation is complicated, but approximate relations remain [125–129]. While analytic continuation of lattice observables suffer from signal-to-noise problems [128, 130–137], observables suitable for scale setting have been studied [138, 139]. Since knowledge of a, a_t is required for any continuum extrapolation, performing scale setting with classical computations would significantly improve the common error budget of quantum computations as the uncertainties for scale setting could be reduced using Euclidean data. We will explore two different schemes for performing analytic continuation of the renormalized lattice spacings, and demonstrate its capabilities for reliable Minkowski scale setting through classical Euclidean computations.

A crucial part of our study is to explore how Minokowski lattice observables computed with quantum circuits can be extrapolated to the continuum in an efficient manner. We will show that trotterized time-evolution can be understood as a Minkowski path integral on an anisotropic lattice. We present a toy model, a D_4 gauge group in $2+1$D with a two spatial plaquettes, to exemplify the power of a fixed anisotropy trajectory to extrapolate quantities to the continuum limit. This requires as a first step to establish the scale setting for the lattice spacings, a, a_t, that can profit from our analytic continuation schemes.

This chapter is organized as follows. In Sec. 2.1 we briefly review the Euclidean action lattice formalism and its connection through the transfer matrix to the Hamiltonian formalism. In Sec. 2.3 we derive the trotterized real-time evolution operator and relate it to the transfer matrix. Based on this, we propose two schemes to obtain Minkowski lattice spac-

ings via analytic continuation and advocate the use of a fixed-anisotropy approach to the continuum. In Sec. 2.4, we discuss the systematic errors from computing a, a_t via analytic continuation. Further, in Sec. 2.5 we present numerical results in our toy model for these techniques. Finally, we conclude in Sec. 2.9.

2.1 Basics of lattice gauge theories

This section reviews the connection between the Kogut-Susskind Hamiltonian [68] and the Euclidean Wilson action. We summarize the derivation of [140] that begins with the anisotropic Wilson action in Euclidean time $\tau = it$ defined on a spacetime lattice:

$$S_E = -\beta_t \sum_t \mathrm{Re}\,\mathrm{tr}\, U_t - \beta_s \sum_s \mathrm{Re}\,\mathrm{Tr}\, U_s \tag{2.1}$$

where $i = t, s$ refers to temporal and spatial plaquettes U_i formed from gauge links given by elements of the group. The anisotropy comes from using different couplings for spatial and temporal plaquettes, that can be written as

$$\beta_t(a, a_0) = \frac{a}{g_t^2(a, a_0) a_0}, \qquad \beta_s(a, a_0) = \frac{a_0}{g_s^2(a, a_0) a} \tag{2.2}$$

with $\beta_i(a, a_0), g_i(a, a_0)$ depending nonperturbatively on the temporal and spatial lattice spacings, a_0, a.

Euclidean lattice theories satisfying the reflection positivity have a well-defined Hamiltonian with real eigenvalues [122, 141]. To the derive this Hamiltonian, we first define a transfer matrix, $T(a, a_0)$ which takes a state at time τ, $|\tau\rangle$, to $|\tau + 1\rangle$. T is related to the action through the partition function Z:

$$Z = \int DU e^{-S_E} = \mathrm{tr}\, T(a_0)^N \tag{2.3}$$

where N is the number of temporal lattice sites. It follows that the matrix elements of $T(a_0)$ are [140]

$$\begin{aligned}
&\langle \tau+1|T(a_0)|\tau\rangle \\
&\quad = e^{\frac{\beta_s}{2}\sum_s \mathrm{Re\,tr}\, U_s} e^{\beta_t \sum_{\{\tau,\tau+1\}} \mathrm{Re\,tr}\, U_t} e^{\frac{\beta_s}{2}\sum_s \mathrm{Re\,tr}\, U_s} \\
&\quad \equiv \langle \tau+1|T_V^{1/2} T_K T_V^{1/2}|\tau\rangle,
\end{aligned} \tag{2.4}$$

where we have symmetrically split the potential term. In order to extract a Hamiltonian from $T(a_0)$, it is convenient to have $T(a_0)$ only in terms of a single time slice. While for U_s this presents no issues, U_t couples the same link at two times $U_{ij}(\tau), U_{ij}(\tau+1)$ via two time-like links which we fix to the identity by considering the temporal gauge. This yields for the kinetic term in the action

$$S_K = -\beta_t \sum_{\{\tau,\tau+1\}} \mathrm{Re\,Tr}\, U_{ij}(\tau) U_{ij}^\dagger(\tau+1) \tag{2.5}$$

To proceed, we need to remove the dependence on $U_{ij}^\dagger(\tau+1)$ and express $T(a_0)$ in terms of operators. The link operator is easy to define $\hat{U}_{ij}|\tau\rangle = U_{ij}|\tau\rangle$. Therefore

$$T_V^{1/2} = e^{\frac{\beta_s}{2}\sum_s \mathrm{Re\,tr}\, \hat{U}_s}. \tag{2.6}$$

For T_K, we need an operator that changes a given link,

$$R_{ij}(g)|\tau\rangle = |\tau'\rangle, \quad \text{where } U_{ij} \to g U_{ij} \tag{2.7}$$

this operator has the group property of $R_{ij}(g)R_{ij}(h) = R_{ij}(gh)$. This gauge link translation can be used to define a conjugate momentum to $\hat{U}_{ij}$ by performing a rotation on $U_{ij}(\tau)$ to

transform it into $U_{ij}(\tau+1)$. With this, we write

$$T_K = \prod_{\{ij\}} T_{K,ij} = \prod_{\{ij\}} \left[\int Dg R_{ij}(g) e^{\beta_t \operatorname{Re}\operatorname{tr} g} \right], \tag{2.8}$$

where the product is over all spatial links $U_{ij}(\tau)$. Any group element can be written as $g = e^{i\omega\cdot\lambda}$ where λ_i are the adjoint generators, and $R_{ij}(g) = e^{i\omega\cdot\hat{l}_{ij}}$ can be written in terms of the generators $\hat{l}_{ij}$ for that representation. Defining $\prod_\alpha (D\omega^\alpha) J(\omega)$ as the invariant group measure with a Jacobian J, it is possible to rewrite $T_K(a_0)$ as

$$T_{K,ij} = \int \prod_\alpha (D\omega^\alpha) J(\omega) e^{i\omega\cdot\hat{l}_{ij}} e^{\beta_t \operatorname{tr}\cos(\omega\cdot\lambda)} \tag{2.9}$$

This transfer matrix is exact for any a_0. At the cost of a sum over all character functions of the group, it can be performed analytically. This is done in [82] and appears practical for discrete groups. But for continuous group, the summation is over infinite terms which is undesirable.

As $a_0 \to 0$ for unitary continuous group, Eq. (2.9) can be expanded to $O(\omega^2)$:

$$T_{K,ij} = \int \prod_\alpha (D\omega^\alpha) \left(1 + O(\omega^2)\right) e^{i\omega\cdot\hat{l}_{ij} + \beta_t[\operatorname{tr}\mathbb{I} - \frac{1}{4}\omega^2 + O(\omega^4)]} \tag{2.10}$$

leaving Gaussian integrals. Integrating yields

$$T_K \;=\; \mathcal{N} e^{-\beta_t^{-1}\sum_{\{ij\}} \hat{l}_{ij}^2} \tag{2.11}$$

where $\mathcal{N}$ is an overall normalization. For discrete groups, the contribution to T_K is also dominated by group elements close to $\mathbb{I}$ when $a_0 \to 0$. However, since for discrete group g cannot be arbitrarily close to $\mathbb{I}$, a naive limit of taking $a_0 \to 0$ leads to degenerate spectrum for T_K. Special care has to be taken [142] to avoid this degeneracy.

Neglecting the normalization factor $\mathcal{N}$, the final transfer matrix $T(a_0)$ is given by

$$T(a_0) = e^{\frac{\beta_s}{2}\sum_s \mathrm{Re\,tr}\,\hat{U}_s} e^{-\beta_t^{-1}\sum_{\{ij\}}\hat{l}_{ij}^2} e^{\frac{\beta_s}{2}\sum_s \mathrm{Re\,tr}\,\hat{U}_s}. \tag{2.12}$$

Since $T(a_0)$ corresponds to the translation from τ to $\tau+1$, it can be used to define a Hamiltonian $H(a_0, a)$ These steps form the link between S_E and $T(a_0)$ in Fig. 2.1.

$$T(a_0) \equiv e^{-a_0 H(a,a_0)}. \tag{2.13}$$

However, because $\hat{l}_{ij}$ and $\hat{U}_{ij}$ are non-commuting operators, writing Eq. (2.12) as a single exponential requires application of the Baker-Campbell-Hausdorff (BCH) formula:

$$e^{tX}e^{tY}e^{tX} = e^{t(2X+Y)-\frac{t^2}{6}([X,[X,Y]]-[Y,[X,Y]])+\ldots}. \tag{2.14}$$

Using this, we obtain for $H(a, a_0)$:

$$\begin{aligned} H(a,a_0) =& \frac{1}{c(a,a_0)a}\Bigg(g_H^2(a,a_0)\sum_{\{ij\}}\hat{l}_{ij}^2 - g_H^{-2}(a,a_0)\sum_s \mathrm{Re\,tr}\,\hat{U}_s \\ &-\frac{1}{24}\frac{1}{c^2(a,a_0)\xi^2}\sum_{\{ij\},s}\Big(g_H^2(a,a_0)[2\hat{l}_{ij}^2,[\hat{l}_{ij}^2,\mathrm{Re\,tr}\,\hat{U}_s]] - g_H^{-2}(a,a_0)[\mathrm{Re\,tr}\,\hat{U}_s,[\hat{l}_{ij}^2,\mathrm{Re\,tr}\,\hat{U}_s]]\Big) + \ldots \Bigg) \end{aligned} \tag{2.15}$$

For conciseness, we define certain Hamiltonian terms

$$\begin{aligned} K_{\mathrm{KS}}(a,a_0) &= \frac{g_H^2(a,a_0)}{c(a,a_0)a}\sum_{\{ij\}}\hat{l}_{ij}^2 \\ V_{\mathrm{KS}}(a,a_0) &= -\frac{1}{g_H^2(a,a_0)c(a,a_0)a}\sum_s \mathrm{Re\,tr}\,\hat{U}_s \end{aligned} \tag{2.16}$$

It is important to emphasize that varying either a_0 or a requires an adjustment to $c(a, a_0)$

and $g_H(a, a_0)$ to preserve the scale setting condition. Besides the ξ-dependent terms, another difference between $H_{\rm KS}$ and $H(a, a_0)$ is that c, g_H only depend upon a in Eq. (2.18), while in Eq. (2.15) they also depend on a_0.

Taking the continuous-time limit of the transfer matrix:

$$\mathcal{T}(\tau) \equiv \lim_{a_0 \to 0, N \to \infty} T(a_0)^N, \tag{2.17}$$

the BCH terms in $H(a, a_0)$ vanish and we obtain the Kogut-Susskind Hamiltonian [68], $H_{\rm KS} \equiv -\frac{1}{\tau} \log(\mathcal{T}(\tau))$ (See Fig. 2.1):

$$H_{\rm KS} = \frac{1}{c(a)a} \left(g_H^2(a) \sum_{\{ij\}} \hat{l}_{ij}^2 - \frac{1}{g_H^2(a)} \sum_s \mathrm{Re}\,\mathrm{Tr}\, U_s \right). \tag{2.18}$$

Historically, the Hamiltonian formalism with limited success was used to evaluate lattice theory by computing results analytically [143–146], variationally [147–150], and with exact diagonalization [151]. In such cases, there was no benefit to keeping a_0 finite and therefore all were done in the Hamiltonian limit. In contrast, quantum simulations have good reasons to consider the Hamiltonian at finite a_0 as we demonstrate in the next section.

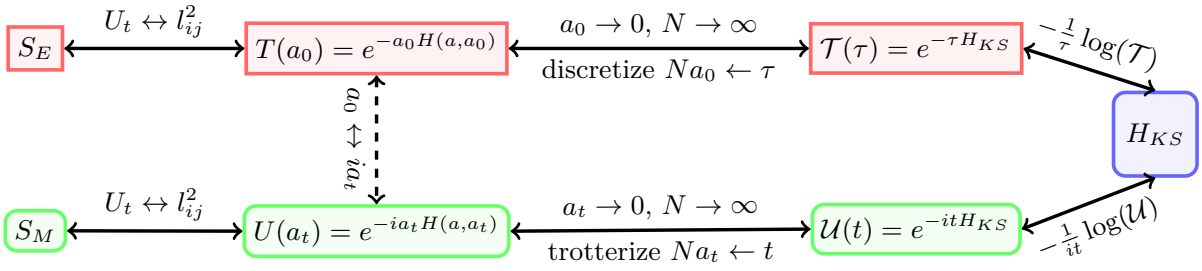

Figure 2.1: Schematic relations between Euclidean LGT and quantum simulations.

2.2 Renormalization of LGTs in classical simulations

The first step in the process of computing physical observables from LGT is the determination of the lattice spacings through *scale setting*. For simplicity we will consider the isotropic case via $\beta_E \equiv \beta_t = \beta_s$, $a = a_0$ and in analogy with Eq. (2.2), define $\beta_E = 2Ng_E^{-2}$ for $SU(N)$ group. The anisotropic case merely requires performing the procedure for both a, a_0 independently. One scale sets by computing a lattice quantity $am(\beta_E)$ where m has a known physical value m^{phys} (e.g. the pion mass). Any lattice $m(\beta_E)$ differs from the true m^{phys} by a dependent errors, but for this one specific observable we set $m(\beta_E) = m^{\text{phys}}$ to obtain a dimensionful value for a

$$a = \frac{[am(\beta_E)]}{m^{\text{phys}}} \tag{2.19}$$

With this, β_E is removed from our theory and we can speak only in terms of a. All other lattice masses can then be written as $am_k(a)$ and their continuum values can be predicted by computing them at multiple lattice spacings and extrapolating to $a \to 0$ via

$$\frac{m_k^{\text{phys}}}{m^{\text{phys}}} = \frac{am_k(a)}{am(a)} + O(a^n) \tag{2.20}$$

When working with continuous gauge theories, there is no theoretical issue with computing at arbitrarily small a, but one is limited by computing resources due to topological freezing and critical slowing-down. On quantum devices, the current resources require dramatic approximations of the continuous group. Here, we will consider the discrete gauge theories. Certain discrete subgroups of continuous groups are effective field theories for the continuous groups [152, 153] which break down below a minimum lattice spacing [56, 154, 155]. Therefore one cannot take a of a discrete group arbitrarily close to zero.

Lattice quantities like $am(\beta_E)$ are obtained from correlation functions, e.g. the temporal correlator $\langle \mathcal{O}_i(na_0)\mathcal{O}_j(0)\rangle$. In the limit where the temporal length of the lattice goes to

infinity, this correlator becomes a vacuum expectation value

$$\langle \mathcal{O}_i(na_0)\mathcal{O}_j(0)\rangle = \sum_k \langle 0|\mathcal{O}_i|k\rangle\langle k|O_j|0\rangle e^{-na_0 m_k} \tag{2.21}$$

From these correlators, one extracts $a_0 m_k$ which correspond to the lattice eigenenergies. For scale setting, one usually wants the lowest energy state $a_0 m_1$ of a specific sector, which can be extracted from the sum by taking n large:

$$\begin{aligned}&\langle \mathcal{O}_i(na_0)\mathcal{O}_j(0)\rangle \\ &\quad = \langle 0|\mathcal{O}_i|1\rangle\langle 1|O_j|0\rangle e^{-na_0 m_1} + O(e^{-na_0\Delta E}).\end{aligned} \tag{2.22}$$

with ΔE the energy gap between the lowest energy state and the next lowest energy state.

An equivalent way of expressing the renormalized parameters is by defining the anisotropic parameter $\xi \equiv a/a_0$ and considering ξ and a as independent parameters. By allowing $\xi \neq 1$ and especially $\xi \gg 1$, lattice practitioners have achieved great success with probing glueballs [156, 157], high temperature thermodynamics [158], etc. As we approach the Hamiltonian limit ($a_0 \to 0$), another couplings, $g_H^2 = g_s g_t$, and the speed of light, $c = g_s g_t^{-1}$, become useful. These bare couplings are related to each other in the weak coupling limit by [159, 160]

$$\begin{aligned}g_s^{-2}(a,a_0) &= g_E^{-2}(a) + c_s(\xi) + O(g_E^2)\\ g_t^{-2}(a,a_0) &= g_E^{-2}(a) + c_t(\xi) + O(g_E^2)\\ g_H^{-2}(a,a_0) &= g_E^{-2}(a) + \frac{c_t(\xi)+c_s(\xi)}{2} + O(g_E^2)\\ c(a,a_0) &= 1 + \frac{c_t(\xi)-c_s(\xi)}{2} g_E^2(a) + O(g_E^4)\end{aligned} \tag{2.23}$$

The $c_i(\xi)$ were computed perturbatively for $SU(N)$ at $\xi = \infty$ for $D = 4$ in [159]. This was generalized in [160] to arbitrary ξ and to arbitrary dimensions in [161].

For typical values of β_i considered in simulations, there are large corrections to these weak coupling results and thus nonperturbative determination of a, ξ is required [162–164]. In pure gauge theory, one method for the determination of ξ is made by comparing ratios of spatial-spatial Wilson loops to spatial-temporal Wilson loops [165]. Once ξ is measured, a could be determined using standard methods such as the Sommer scale r_0 [156, 157, 166] or the Wilson flow [167, 168].

2.3 Trotterization and Time-Evolution

The starting point for real-time evolution on quantum computers is to define $\mathcal{U}(t) = e^{-iHt}$. For gauge theories, one typically takes the lattice Hamiltonian to be H_{KS} in Eq. (2.18). This $\mathcal{U}(t)$ cannot be implemented easily on quantum computers and must be approximated, resulting in effects that have to be renormalized. Trotterization discretizes the evolution into $N = t/a_t$ steps formed of products of $e^{ix_i H_j}$ where different choices of $x_i \propto a_t$ lead to errors at different order of a_t and H_i are a decomposition of H into mutually noncommuting terms. In the case of H_{KS}, there are two $H_i = K_{\text{KS}}, V_{\text{KS}}$, in which case $\mathcal{U}(t)$ is approximated by

$$\begin{aligned}\mathcal{U}(t) &= e^{-iH_{\text{KS}}t} \\ &\approx [e^{ix_1 H_V} e^{ix_2 H_K} e^{ix_3 H_V} e^{ix_4 H_K} \dots]^N + O(a_t^p).\end{aligned} \tag{2.24}$$

The number of terms and x_i for a given $O(a_t^p)$ error can be derived by repeated applications of the BCH relation, Eq. (2.14). In the case of $O(a_t^2)$, this corresponds to

$$U(a_t) \approx e^{-ia_t V_{\text{KS}}/2} e^{-ia_t K_{\text{KS}}} e^{-ia_t V_{\text{KS}}/2} \tag{2.25}$$

Following Fig. 2.1, we see that we have essentially reversed the path taken to derive H_{KS} from $T(a_0)$. With this approximation, we can ask, what Hamiltonian are we actually evolving

with respect to? Analogous to the euclidean derivation of Eq. (2.15) from Eq. (2.12), we can define

$$U(a_t) = e^{-ia_t H(a_t)}, \tag{2.26}$$

finding

$$\begin{aligned} H(a_t) &= K_{\mathrm{KS}} + V_{\mathrm{KS}} \\ &- \frac{a_t^2}{24}\Big([2K_{\mathrm{KS}}, [K_{\mathrm{KS}}, V_{\mathrm{KS}}]] + [V_{\mathrm{KS}}, [K_{\mathrm{KS}}, V_{\mathrm{KS}}]]\Big) + \dots \end{aligned} \tag{2.27}$$

By trotterizating $\mathcal{U}(t)$, we have introduced a temporal lattice spacing a_t. One might be tempted to believe that the renormalized a_t is a parameter that can be directly tuned, but this is incorrect. This can be seen by inserting Eq. (2.16) into Eq. (2.27), from which one observes that in the same way as the Euclidean results, a_t is always multiplied by $[c(a, a_t)a]^{-1}$. Thus, changes in a_t are compensated by modifying the bare speed of light. It it therefore natural to define a lattice bare parameter which we can control in simulations:

$$\delta_t \equiv \frac{a_t}{c(a, a_t)a}. \tag{2.28}$$

Thus we find that a_t must be determined nonperturbatively by scale setting. Naively, a_t, a would be obtained by performing a quantum simulation, which on near-term hardware is likely to be noisy, and therefore the lattice spacings will have large uncertainties. Since all other lattice observables depend upon the scale-setting, minimizing the uncertainties of a, a_t is crucial to the overall program of quantum simulations of LGT. In practice, keeping these uncertainties small require high statistics of very deep circuits with error mitigation. Instead of computing a_t, a on the quantum device, it is possible to utilize classical Euclidean computations of a, a_0 to scale setting in a quantum computer.

If the Minkowski and Euclidean lattice Hamiltonians were the same, we could trivially

set a, a_0 to a and a_t – establishing a link between the lattice results in each metric (See Fig. 2.1). However, the Hamiltonians only match when $a_t, a_0 \to 0$, when they both reduce to $H_{\rm KS}$. Instead, at finite a_t, a_0 they differ as we show explicitly in the following. In analogy to Eq. (2.28), we define the quantity $\delta_\tau \equiv \frac{a_0}{c(a,a_0)a}$ on the Euclidean side. With this, we can recast $T(a_0)$ in Eq. (2.12):

$$T(\delta_\tau, g_H^2) \;=\; e^{-\delta_\tau V_{\rm KS}/2} e^{-\delta_\tau K_{\rm KS}} e^{-\delta_\tau V_{\rm KS}/2} \tag{2.29}$$

with the following Hamiltonian terms:

$$K_{\rm KS} = g_H^2 \sum_{\{ij\}} \hat{l}_{ij}^2, \quad V_{\rm KS} = -g_H^{-2} \sum_s \mathrm{Re}\,\mathrm{Tr}\,\hat{U}_s. \tag{2.30}$$

Taking $\delta_\tau \to i\delta_t$ in Eq. (2.29), we analytically continue $T(\delta_\tau, g_H^2)$, obtaining

$$U(\delta_t, g_H^2) \;= e^{-i\delta_t V_{\rm KS}/2} e^{-i\delta_t K_{\rm KS}} e^{-i\delta_t V_{\rm KS}/2} \tag{2.31}$$

which we recognize as Eq. (2.25) written in terms of bare parameters. From these, we can define the dimensionless Hamiltonians using only bare parameters:

$$\overline{H}(\delta, g_H^2) = K_{\rm KS} + V_{\rm KS} + \frac{\delta^2}{24}\Big([2K_{\rm KS}, [K_{\rm KS}, V_{\rm KS}]] + [V_{\rm KS}, [K_{\rm KS}, V_{\rm KS}]] \Big) + \ldots \tag{2.32}$$

where $\delta = \delta_\tau, i\delta_t$ depending on the metric signature. From this we see that there are differing signs for the BCH terms in real and imaginary time. Given that the Hamiltonians differ, correlation functions and the scale setting observables $a_t m$ and $a_0 m$ must also differ even if we take $\delta_t = \delta_\tau$. But, these differences arise at $O(\delta_t^2, \delta_\tau^2)$ and vanish in the continuous time limit, $\delta_t = \delta_\tau = 0$.

One possible scheme for using a, a_0 to determine a, a_t would be to simply neglect these

$O(\delta_t^2, \delta_\tau^2)$ errors and assume the two sets of scales are equal for the same g_H and $\delta_\tau = \delta_t$:

$$\begin{aligned} \textbf{Scheme A}: \quad & a(\delta_\tau, g_H^2) \to a(\delta_t, g_H^2) \\ & a_0(\delta_\tau, g_H^2) \to a_t(\delta_t, g_H^2) \end{aligned} \tag{2.33}$$

A benefit of this scheme is that only one set of Euclidean couplings is simulated. While this scheme introduces an $O(\delta_t^2, \delta_\tau^2)$ systematic error into the scale setting, one could easily imagine it being tolerable compared to errors from near-term quantum computers.

In principle, this systematic error can be reduced by observing that if one takes $\delta_\tau \to i\delta_t$, then the two Hamiltonians agree. Formally, this means that the eigenvalues $m_k(\delta_t, g_H^2)$ are the analytic continuation of $m_k(\delta_\tau, g_H^2)$.

While the spatial correlators in Minkowski behave exactly like the Euclidean ones of Eq. (2.21) with the replacement of $m_k(\delta_t, g_H^2)$, the temporal correlators require $a_0 \to i a_t$

$$\langle \mathcal{O}_i(n a_t) \mathcal{O}_j(0) \rangle = \sum_k \langle 0|\mathcal{O}_i|k\rangle \langle k|\mathcal{O}_j|0\rangle e^{-i n a_t m_k} \tag{2.34}$$

where $|k\rangle$ are the Minkowski eigenstates. While the excited state contributions do not decrease with $n a_t \to \infty$, provided that we can isolate a single scale setting parameter m then the lattice results $a_t m(a, a_t)$ are the analytic continuation of $a_0 m(a, a_0)$. This suggest that a scale setting scheme with reduced systematic error is through analytical continuation:

$$\begin{aligned} \textbf{Scheme B}: \quad & a(\delta_\tau \to i\delta_t, g_H^2) \to a(\delta_t, g_H^2) \\ & a_0(\delta_\tau \to i\delta_t, g_H^2) \to a_t(\delta_t, g_H^2) \end{aligned} \tag{2.35}$$

In contrast to Scheme A, this procedure requires the determination of the lattice spacings at multiple values of g_H, δ_τ in the region around the desired lattice spacings. With this set of values, one derives a fit function for $a(\delta_\tau, g_H^2), a_0(\delta_\tau, g_H^2)$. This function can then

be analytically continued to Minkowski space, reducing the nonperturbative BCH errors. The effectiveness of this method, like all analytic continuations of lattice results, depends sensitively on the statistics and fitting function, as we will discuss later.

In the preceding discussion, the relation between the lattice spacings depending upon the Hamiltonians being analytical continuations of each other. Traditionally, Euclidean calculations are performed with an action like Eq. (2.1). Different actions correspond to different lattice Hamiltonians. For the Wilson action, we observe that $H(a, a_0)$ of Eq. (2.15) is not the exact lattice Hamiltonian being computed, but arises only when we expand T_K to $O(\omega^2)$. Thus, a systematic mismatch occurs if one tries to scale set a, a_t with Wilson action results. Furthermore, including the higher order ω terms from Eq. (2.1) leads to a non-trivial dependence on δ_τ. This causes a non-Hermitian Hamiltonian upon analytic continuation [169] although this behavior may prove manageable [124]. In contrast, using an action with a heat-kernel kinetic term (the Laplace-Beltrami operator) [170] with a Wilson single plaquette potential term, the higher order ω terms vanish and the mapping is exact. Another approach to obtain a Hermitian lattice Hamiltonian useful in Minkowski space is obtained by analytic continuing the character expansion of $T_K(\delta_\tau = \delta_t, g_H^2)$ term-by-term [129, 169].

With observables computed at multiple a_t, a, one can perform continuum extrapolations analogous to the Euclidean calculations. Influenced by nonrelativistic results, the literature has emphasized first approaching the Hamiltonian limit $a_t \to 0$, then taking $a \to 0$. This procedure introduces two inefficiencies. First, taking a continuum limit as a two-step procedure requires $m \times n$ separate simulations at m values of a_t for n values of a in the (a, a_t) plane, extrapolating each fixed-a set to the $a_t \to 0$, and then extrapolating the remaining a-dependent results to $a \to 0$. Secondly, because uncertainty in the $a \to 0$ extrapolation is controlled by how well each $a_t \to 0$ extrapolation is, one desires smaller a_t. This increases gate costs $\propto \delta_t^{-1}$.

Instead of first approaching the Hamiltonian limit, a more efficient trajectory is to compute a set of points $a, a_t \to 0$ at fixed ξ_t. This clearly reduces the total number of quantum simulations required. Additionally, since only one extrapolation is performed lattice errors are easier to control. This would allow larger a_t. We thus expect the fixed-ξ_t trajectory to avoid deep quantum circuits and suffer less from noise.

2.4 The errors of scale-setting in Minkowski metric

Although the analytic continuation between Euclidean and Minkowski scales proposed in **Scheme B** is formally exact, in practice one can only perform the analytic continuation from fits to discrete, noisy Euclidean data $a(\delta_\tau, g_H^2), a_0(\delta_\tau, g_H^2)$. This leads to a signal-to-noise problem when performing the analytic continuation [133]. Indeed, to achieve a certain precision the Euclidean data has to be exponentially more accurate: intuitively, this is because excitations caused by BCH operators decay exponentially in τ but oscillate in t. As a result, low-energy observables in Euclidean lattices tend to be less sensitive to the variation of δ than their Minkowski counterparts. Hence the analytic continuation is ill-posed [171]. Fortunately, at small δ, the calculations with lower-energy states are less influenced by the higher order BCH operators, and hence one can reasonably tame the errors intrinsic to the Euclidean data. This observation is of crucial relevance for our scale-setting procedure.

On the other hand, the difference between Minkowski and Euclidean renormalized lattice scales must be smaller for smaller trotter steps $\delta_{t,\tau}$ as both $\overline{H}(\delta_\tau, g_H^2)$ and $\overline{H}(i\delta_t, g_H^2)$ are closer to the same Hamiltonian limit. This implies that there might be a parameter space where **Scheme A** yields more accurate results for Minkowski scale-setting, leading to question the feasibility of **Scheme B**. In this section, we give upper bounds for the scale-setting error of both schemes and discuss if the advantage of analytic continuation of a given scheme is balanced out by its errors.

Consider the bare eigenvalue $\lambda(\delta_\tau, g_H^2) \equiv a_0(\delta_\tau, g_H^2) m^{\text{phys}}/\delta_\tau$ of $\overline{H}(\delta_\tau, g_H^2)$. In real time,

the equivalent eigenvalue of $\overline{H}(i\delta_t, g_H^2)$ is $\lambda(i\delta_t, g_H^2) \equiv a_t(\delta_t, g_H^2) m^{\rm phys}/\delta_t$. Let $\lambda_m(\delta_\tau, g_H^2)$ be the measured values of $\lambda(\delta_\tau, g_H^2)$ on Euclidean lattices, with a deviation from the theoretical value $\epsilon_A = |\lambda_m(\delta_\tau, g_H^2) - \lambda(\delta_\tau, g_H^2)|$ from statistical errors of the measurement.

For $\delta_\tau = \delta_t$, **Scheme A** approximates $\lambda(i\delta_t, g_H^2)$ as $\lambda_m(\delta_\tau, g_H^2)$ such that the error is given by

$$\begin{aligned}
&|\lambda(i\delta_t, g_H^2) - \lambda_m(\delta_\tau, g_H^2)| \\
&\quad \le |\lambda(i\delta_t, g_H^2) - \lambda(0, g_H^2)| + |\lambda(\delta_\tau, g_H^2) - \lambda(0, g_H^2)| \\
&\qquad + |\lambda(\delta_\tau, g_H^2) - \lambda_m(\delta_\tau, g_H^2)|
\end{aligned} \tag{2.36}$$

where $\lambda(0, g_H^2)$ is the corresponding energy gap evaluated in the continuous time limit $\delta = 0$.

The first two terms on the RHS of Eq. (2.36) quantify the errors from the BCH contributions. The last term is ϵ_A, the statistical error of the Euclidean temporal scale at δ_τ. We obtain the following constraint on the trotterization error according to the Bauer-Fike theorem [172],

$$|\lambda(\delta, g_H^2) - \lambda(0, g_H^2)| \le 2\|\overline{H}(\delta, g_H^2) - \overline{H}(0, g_H^2)\| \tag{2.37}$$

At small δ, $\|\overline{H}(\delta, g_H^2) - \overline{H}(0, g_H^2)\|$ is dominated by the leading order BCH commutators of order $|\delta|^2$.

$$\begin{aligned}
\|\overline{H}(\delta, g_H^2) - \overline{H}(0, g_H^2)\| &\lesssim \frac{|\delta|^2}{24} \left(2\|[[V_{\rm KS}, K_{\rm KS}], K_{\rm KS}]\| + \|[[V_{\rm KS}, K_{\rm KS}], V_{\rm KS}]\|\right) \\
&\le \frac{|\delta|^2}{3} \mathcal{N}_{link}(d-1) d_U \|\hat{l}^2\| \left(g_H^2 8\|\hat{l}^2\| + g_H^{-2} 2(d-1) d_U\right) \\
&\le \frac{|\delta|^2}{4(\max\delta)^2} M
\end{aligned} \tag{2.38}$$

where d is the number of spacial dimensions, d_U is the dimension of the representation of

the group element U in $V_{\rm KS}$, $\mathcal{N}_{link}$ is the number of links in the spacial lattice, and $\|\hat{l^2}\|$ is the spectral norm of a single link operator $\hat{l}^2_{ij}$. We have introduced additional definitions into the second line,

$$\max\delta \equiv \min\left\{\frac{g_H^2}{4(d-1)d_U}, \frac{1}{g_H^2 8\|\hat{l^2}\|}\right\} \tag{2.39}$$

$$M \equiv 2\mathcal{N}_{link}(d-1)d_U\|\hat{l^2}\|\max\delta \tag{2.40}$$

The inequality of Eq. (2.38) is only guaranteed within the range $|\delta| < \max\delta$ because next to leading order commutators are only negligible within such range, as shown in Appendix 2.7. Thus, Eq. (2.37) is bounded by $M/2$ for $|\delta| \leq \max\delta$. Combining all the above definitions and inequalities, the upper bound of temporal scale-setting errors for **Scheme A** is

$$|\lambda(i\delta_t, g_H^2) - \lambda_m(\delta_\tau, g_H^2)| \lesssim \left(\frac{\delta_t^2}{\max\delta^2} + \frac{\epsilon_A}{M}\right)M \tag{2.41}$$

which is bounded by $M + \epsilon_A$ for $\delta \leq \max\delta$. As M quantifies the upper limit of the trotterization error in Eq. (2.37) and also the error of **Scheme A**, we refer to M as the error bound parameter from the BCH expansion.

As **Scheme B** requires the knowledge of the functional dependence of the scales on g_H and δ_τ, we assume that the theoretical $\lambda(\delta, g_H^2)$ is both analytic and even in power of δ within the radius $|\delta| \leq \max\delta$, i.e. $\lambda(\delta, g_H^2) = \lambda(-\delta, g_H^2)$. This is based on the following perturbative argument: for small $|\delta|$, the BCH commutators $\overline{H}(\delta, g_H^2) - \overline{H}(0, g_H^2)$ can be treated as perturbations to the Hamiltonian limit $\overline{H}(0, g_H^2)$. With the second-order trotterization, all the non-vanishing BCH commutators depend on even orders of δ. Therefore, perturbatively, the difference in the spectra of $\overline{H}(\delta, g_H^2)$ and $\overline{H}(0, g_H^2)$ should be analytic and even in powers of δ order by order. One thus fits the functional form $\lambda_f(\delta_\tau, g_H^2)$ for Euclidean temporal scales in even powers of δ_τ. This guarantees that the analytic continuation $\lambda_f(i\delta_t, g_H^2)$ is

real, thus avoiding nonunitarity in the Minkowski metric.

Define ϵ_B as the maximum deviation of $\lambda_f(\delta_\tau, g_H^2)$ from the theoretical $\lambda(\delta_\tau, g_H^2)$ across the Euclidean region, such that $|\lambda_f(\delta_\tau, g_H^2) - \lambda(\delta_\tau, g_H^2)| \leq \epsilon_B$ for all $0 < \delta_\tau \leq \max \delta$. ϵ_B is affected by both the precision of the measurements on the Euclidean data and the fitting procedure. Since the computational resources required grow with decreasing δ_τ, $|\lambda_f(0, g_H^2) - \lambda(0, g_H^2)|$ is likely to be the largest deviation. The region $\delta \leq \max \delta$ is defined such that $O(\delta^4)$ terms are at most equal to the $O(\delta^2)$ terms. Therefore within this region, a quartic $\lambda_f(\delta_\tau, g_H^2)$ should reasonably approximate $\lambda(\delta_\tau, g_H^2)$. By performing calculations at three or more δ_τ each with ϵ_A, one would expect the value of $|\lambda_f(0, g_H^2) - \lambda(0, g_H^2)|$ and therefore ϵ_B to be larger than ϵ_A only by an order-one factor. In addition, we will require the condition in Eq. (2.70): $|\lambda_f(\delta, g_H^2) - \lambda(\delta, g_H^2)| \leq M + \epsilon_B$ in the whole complex plane satisfying $|\delta| < \max \delta$. As shown in Appendix 2.8, we derive an upper bound on the error of the temporal scale-setting for **Scheme B**:

$$|\lambda(i\delta_t, g_H^2) - \lambda_f(i\delta_t, g_H^2)| \lesssim \epsilon_B \left(\frac{M + \epsilon_B}{\epsilon_B} \right)^{\omega(\delta_t)} \tag{2.42}$$

with $0 < \omega(\delta_t) = \frac{4}{\pi} \arctan \frac{\delta_t}{\max \delta} < 1$ following the Lemma 1 in [171].

The advantage of using **Scheme B** could be seen from comparing the ratio of Eq. (2.42) to Eq. (2.41) when setting $\epsilon_A = \epsilon_B = \epsilon$. The error in **Scheme A** has a quadratic dependence on δ_t. When $\epsilon/M \ll 1$, the growth of the errors in **Scheme B** is delayed with respect to that in **Scheme A**, until δ_t is very close to $\max \delta$, as shown in Fig. 2.2. It results that such advantage of **Scheme B** over **Scheme A** requires $\epsilon/M < 0.053$, where around $\epsilon/M = 0.053$, the derivatives of the two prefactors respective to δ_t are the same at $\delta_t = \max \delta$. Ultimately, the overall accuracy of the scale setting in both schemes is controlled by the magnitude of the error bound parameter M. All the above holds, unless the error bound parameter M is too large such that simulations at very small δ_t values are necessary to have the overall

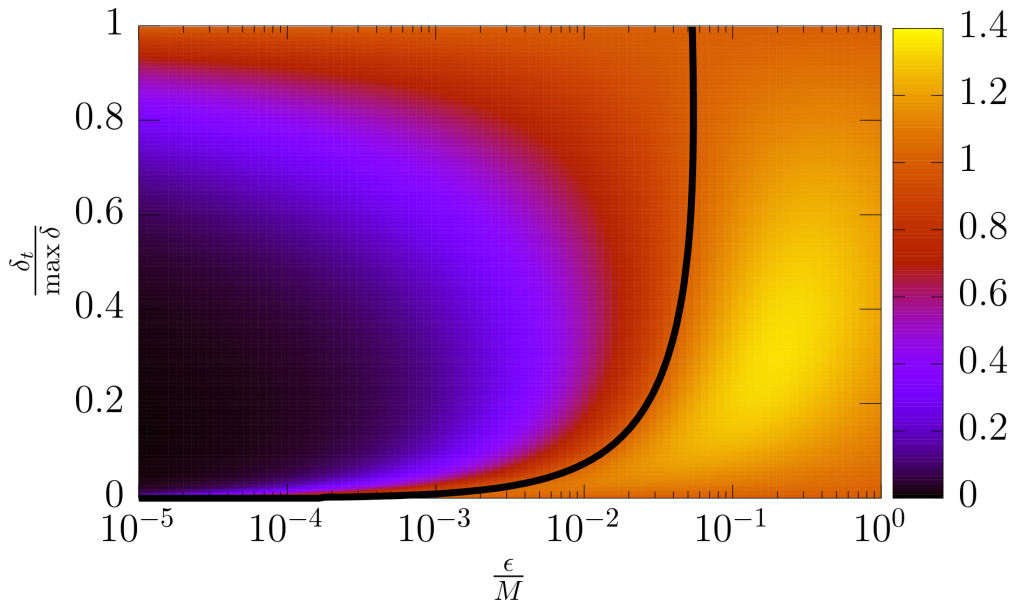

Figure 2.2: Ratio of the error bounds of **Scheme B** in Eq. (2.42) to that of **Scheme A** in Eq. (2.41). The black line indicates when the bounds are equal.

accuracy under control, which are computationally very expensive.

The result that **Scheme B** performs better at small ϵ/M ratio has clear physical interpretations. Correcting BCH errors as **Scheme B** does via analytic continuation becomes more important when the error bound parameter M is larger. On the other hand, in the **Scheme B**, the analytic continuation is sensitive to the Euclidean precision ϵ as seen from Eq. (2.42), while **Scheme A** is less affected. For **Scheme B** to yield a smaller error, certain accuracy of the functional form $\lambda_f(\delta_\tau, g_H^2)$ has to be achieved. This leads to the practical concern that a large amount of resources on the Euclidean calculation might be required at small couplings as the signals become weaker. In addition, for the low energy states involved in the scale-setting procedure, the error bound parameter M could be smaller than the estimation using Eq. (2.39). Therefore, we expect both Eq. (2.41) and Eq. (2.42) to be conservative bounds, as one can confirm by comparing Tab. 2.1 and Fig. 2.7. In such cases, a smaller error ϵ would be required to obtain the same values of ϵ/M that govern the suppression of the errors in **Scheme B**.

In Table 2.1 we estimate for D_4 models with 2 and 3 spatial dimensions and different number of plaquettes/number of links/different values of the bare coupling g_H, the largest possible trotter step compatible with 0.1 errors on the temporal-scale-setting for **Scheme A** and **Scheme B**, assuming $\epsilon = 0.02$. We observe that as expected, the advantage of **Scheme B** to allow the use of relative large trotter step at a given systematic error level is remarkable for larger systems and stronger couplings, that in turn corresponds to larger values of M.

d	$\mathcal{N}_{\text{plaquette}}$	$\mathcal{N}_{\text{link}}$	g_H^2	$\max \delta$	M	δ_t^A	δ_t^B
			0.33	0.041	0.23	0.024	0.022
2	2	4	0.71	0.089	2.1	0.017	0.025
			1.0	0.059	2.0	0.012	0.017
			0.1	0.013	5.8×10^{-4}	0.013	0.013
2	4^2	32	0.5	0.063	7.2	0.0066	0.014
			1.0	0.059	16	0.0042	0.011
			0.1	0.0063	3.5×10^{-3}	0.0063	0.0063
3	4^3	192	0.5	0.032	43	0.0013	0.0052
			1.0	0.059	192	0.0012	0.0082

Table 2.1: Benchmark values for D_4 models in $2+1D$ and $3+1D$ with periodic conditions. Assuming $\epsilon = 0.02$ and demanding the errors in Eq. (2.41) and Eq. (2.42) to be below 0.1, δ_t^A, δ_t^B are largest possible δ_t for **Scheme A** and **Scheme B**. When $g_H^2 = 0.1$, $M < 0.1$ and we take $\delta_t^A = \delta_t^B = \max \delta$. The first three rows use the same parameters as in Fig. 2.7. The absolute error in Tab. 2.1 can be converted to the relative error in Fig. 2.7 by use of a factor $\delta_t / a_t m_{1\times 1} \approx 1$ from Tab. 2.2.

2.5 Numerical Results

In this section we present a concrete demonstration of some of the theoretical perspectives discussed above by using a two-plaquette theory with the discrete, non-Abelian gauge group D_4. We perform classical simulations of a quantum computer using `qiskit` [173, 174]. These calculations are performed without modeling of realistic noise sources, corresponding to a perfect, error-free quantum computer.

We simulate the D_4 gauge field on the two-dimensional lattice shown in Fig. 2.3. This lattice represents the smallest two-dimensional lattice which cannot be reduced to a one-

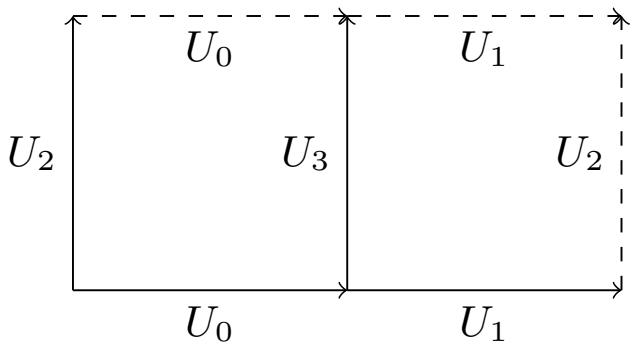

Figure 2.3: The lattice geometry used for the D_4 gauge simulation. The plaquettes are given by $U_2^\dagger U_0^\dagger U_3 U_0$ and $U_3^\dagger U_1^\dagger U_2 U_1$. Dash lines are used to indicate repeated links due to the periodic boundary conditions.

dimensional theory. The simulations requires a five D_4 registers, and uses a total of 17 qubits: 12 for physical degrees of freedom, 3 for an ancillary group register, and 2 ancillary qubits. Note that, for brevity, we have broken with the notation of previous sections, in referring to a link not by the source and sink sites, but instead with a single direct index $i = 0 \ldots 3$.

We define a trace on D_4 (not uniquely specified by the group structure) by embedding D_4 into $U(2)$, and defining the trace via the fundamental representation of that Lie group. The embedding of $D_4 < U(2)$ is generated by the elements σ_x and $i\sigma_z$. The Hamiltonian terms are

$$\begin{aligned} V_{\mathrm{KS}} &= -\frac{1}{\delta_t} \log T_V \\ &= -\frac{1}{g_H^2} \Big(\operatorname{Re} \operatorname{Tr} \left[U_2^\dagger(t) U_0^\dagger(t) U_3(t) U_0(t) \right] \\ &\qquad + \operatorname{Re} \operatorname{Tr} \left[U_3^\dagger(t) U_1^\dagger(t) U_2(t) U_1(t) \right] \Big) \\ K_{\mathrm{KS}} &= -\frac{1}{\delta_t} \sum_{i=0..3} \log T_K^{(i)} \end{aligned} \tag{2.43}$$

where $\log T_K^{(i)}$ is the one-link kinetic term for the i-th link, determined as discussed in

Appendix 2.55. [1] In total, the quantum simulations entailed ~ 200 entangling gates per δ [82]. This is roughly the resources recently used in [175–177], suggesting that a single step of time evolution may be possible on current quantum devices.

Stochastic state preparation has been demonstrated for thermal states in D_4 [100] and particle-like states in $\mathbb{Z}_2$ [101]. While these results are promising, the initial states are found to have contamination from excited states that complicates the analysis. Therefore, to simplify the study of trotterization and the continuum limit, we use exact diagonalization of the Kogut-Susskind Hamiltonian to compute the eigenvalues and then construct our initial state as

$$|\psi(0)\rangle = \frac{1}{\sqrt{2}}|\psi_0\rangle + \frac{1}{\sqrt{2}}|\psi_i\rangle \tag{2.44}$$

where $|\psi_i\rangle$ correspond to the $i-$th excited state which is non-degenerate. By preparing such initial states, the corresponding time-dependent state should be

$$|\psi(t)\rangle_{\rm KS} = \frac{e^{iE_0 t}}{\sqrt{2}}|\psi_0\rangle + \frac{e^{iE_i t}}{\sqrt{2}}|\psi_i\rangle. \tag{2.45}$$

As pointed out in [101] at finite a_t, trotterization mixes Kogut-Susskind eigenstates through nonzero transition matrix elements $\langle\psi_k|H(a,a_t)|\psi(0)\rangle$:

$$\begin{aligned} |\psi(t)\rangle &= e^{iH(a,a_t)t}|\psi(0)\rangle \\ &= \sum_k e^{iE_k(a_t)t}|\psi_k(a_t)\rangle\langle\psi_k(a_t)|\psi(0)\rangle \\ &= \sum_k \lambda_k e^{iE_k(a_t)t}|\psi_k(a_t)\rangle \end{aligned} \tag{2.46}$$

As $a_t \to 0$, one can show that the time-dependent state in Eq. (2.46) reduces to Eq. (2.45).

1. For the numerical calculations, we take $\delta_t = 1$ in $K_{\rm KS}$ specifically for the discrete group, such that the eigenvalues of the kinetic Hamiltonian are sufficiently differentiated when the system is evolved with small trotterization step. This trajectory is adequate since, using the character expansion for the kinetic part of the transfer matrix in Appendix. 2.6, one can show that this construction captures the kinetic energy in the continuous time limit taken for a discrete group.

Performing measurements of the operator $\mathcal{O}$ on this state with a quantum computer yields

$$\begin{aligned}&\langle\mathcal{O}(t)\rangle \equiv \langle\psi(t)|\mathcal{O}|\psi(t)\rangle \\ =&c_0 + \sum_{k\neq j}\left[c_{k,j}\cos\big(a_t(E_j - E_k)l\big) + s_{k,j}\sin\big(a_t(E_j - E_k)l\big)\right]\end{aligned} \tag{2.47}$$

where $l = [0, N]$ is the integer trotter step. $c_{k,j}, s_{k,j}$ incorporate both the mixing effects entailed in λ_k and the matrix elements of $\mathcal{O}$. The E_k here and in the following are eigenvalues of $H(a, a_t)$ and have explicit dependence on a_t. This expression, analogous to euclidean lattice field theory operators, can be used to fit the energies of states $a_t m_i \equiv a_t(E_i - E_0)$ where E_0 is the ground state energy, corresponding to a non-degenerate ground state. As we decrease δ_t, the coefficients of excited-states which can only be non-zero due to contamination, should vanish. Therefore, by performing the fit in Eq. (2.47) for multiple values of δ_t and comparing the results for the coefficients, it is possible to distinguish the physical gap from the other gaps appearing due to contamination.

It is useful here to compare the fitting procedure to that of Euclidean LFT. In Euclidean space, $\langle\mathcal{O}(\tau)\rangle \sim \sum_i \alpha_i e^{-E_i\tau}$ and thus taking $\tau \to \infty$ acts as a low-pass filter which removes higher energy states. In this way, for sufficiently large τ, $\langle\mathcal{O}(\tau)\rangle$ should be exponentially dominated by a single state E_1 and one can extract $a_0 E_1$. In contrast, $\langle\mathcal{O}(t)\rangle \sim \sum_i \beta_i e^{-iE_i t}$ and thus the excited-state contribution to the lattice matrix element doesn't decrease as $t \to \infty$. This lack of a natural low-pass filter is why real-time evolution can access matrix elements that could be inaccessibly to Euclidean LFT; it also means that the excited-state contamination from imprecise state preparation and trotterization cannot be trivially removed. In this sense, the sampling advantage of quantum computers could be jeopardized by errors induced from excited state contamination.

In this chapter, we will use two different spatial Wilson loops as our operators $\mathcal{O}$, which have different quantum numbers, and therefore are sensitive to different eigenstates. The

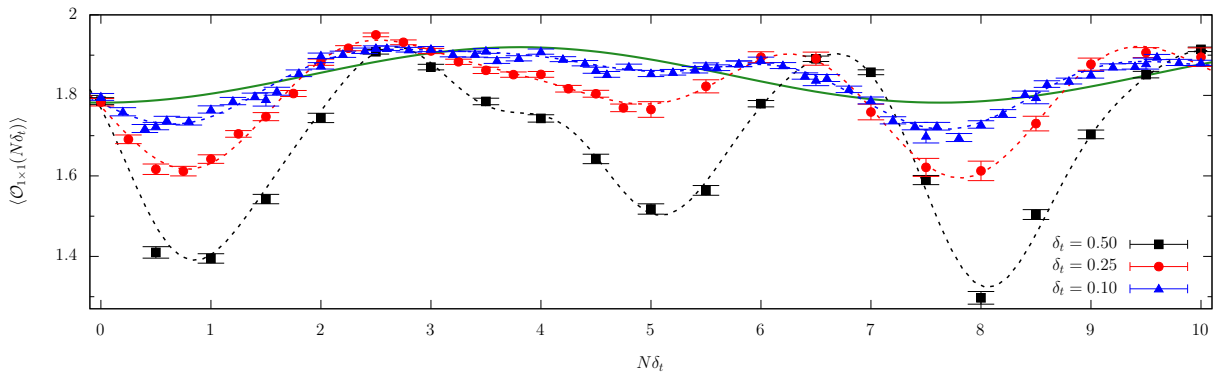

Figure 2.4: Expectation value of the plaquette $\langle \mathcal{O}_{1\times1}(N\delta_t) \rangle$ vs $N\delta_t$ for different δ_t with fixed $g_H^2 = 1.11$. The green line indicated the $\delta_t \to 0$ exact results

first is the left plaquette, $\mathcal{O}_{1\times1} = \mathrm{Re}\,\mathrm{Tr}\, U_0 U_3 U_0^\dagger U_2^\dagger$, and by following the construction of [82] it can be measured without any ancillary qubit. The second is the Wilson loop over the entire lattice, $\mathcal{O}_{2\times1} \sim \mathrm{Re}\,\mathrm{Tr}\, U_0 U_1 U_2 U_1^\dagger U_0^\dagger U_2^\dagger$, which requires an ancillary group register to be computed [178]. For each of these operators, we construct different initial states from Eq. (2.44).

The computations are done for multiple values of $g_H^2(a, a_t) = [0.71, 1.25]$ and $\delta_t = [0.01, 0.7]$ for $N\delta_t = [10, 20]$. The circuits used are detailed in [82]. The BCH contributions vanish for $g_H^2(a, a_t) \to 0$, and as a result, the matrix elements $c_{k,j}, s_{k,j}$ in Eq. (2.47) vanish with only $c_{i,0}$ and $s_{i,0}$ surviving. Further, the statistical errors required to resolve oscillations in $\langle \mathcal{O}(t) \rangle$ must be decreased accordingly, calling for increased number of shots. An additional complication from the continuum limit approach is that the gaps $a_t m_j - a_t m_i \to 0$ as $g_H^2 \to 0$ and thus contamination due to trotterization errors grow unless δ_t is decreased as well. Together, these amount to the cost of the approach to the continuum to scale poorly. For our model, we find that for $g_H^2(a, a_t) > 1$, the required number of shots for the `qiskit` noiseless simulator `qasm` ranged from 1600 to 64000 as we decreased δ_t, g_H^2. For this reason, we utilized `state_vector` simulator – which reports exact probability distributions – for $g_H^2(a, a_t) \leq 1$ in order to investigate the continuum limit at reduced computational cost. This just emphasizes the importance of being able to perform calculations at large

a, a_t on reducing the quantum resources required. For the D_4 theory, the eigenvalues of $V_{\rm KS}$ (Eq. (2.43)) are $1/g_H^2 \times \{-4, -2, 0, 2, 4\}$. States evolved under one-step time evolution operator $e^{i\delta_t V_{\rm KS}/2}$ built from $V_{\rm KS}$ will obtain phases in the range $\delta_t/2g_H^2 \times [-4, 4]$. For the δ_t and g_H^2 chosen, the phase differences are smaller than 2π so that one can resolve states with different potential energies.

2.5.1 Scale Setting in Minkowski Spacetime

We evaluate $\langle \mathcal{O}_{1\times1}(t)\rangle$ to investigate the effect of the renormalization of the temporal scale in Minkowski calculation, by performing fits to Eq. (2.47) and extracting the lowest energy gap $a_t m_{1\times1}$ from $\langle \mathcal{O}_{1\times1}(t)\rangle$. The initial state is constructed from Eq. (2.44) with excited state $i = 2$. An example of these calculations is found in Fig. 2.4 for fixed $g_H^2(a, a_0) = 1.11$ and three different $\delta_t = \{0.5, 0.25, 0.1\}$. Comparing the trotterized results to the continuous-time one calculated using classical computations, the state contamination can be clearly observed and decreases for smaller values of δ_t. The results for $a_t m_{1\times1}$, for the whole range of g_H^2 and δ_t are found in Table 2.2. We observe that the bare mass $a_t m_{1\times1}/\delta_t$ is changed by only 3% when δ_t increases from 0.1 to 0.5 for $g_H^2 = 1.11$, while the mixing effect could be changed by around 20% from comparing the $c_{k,j}, s_{k,j}$ amplitudes in Fig. 2.4.

In the Euclidean lattice calculation, using the relation in Eq. (2.23) obtained in the weak coupling limit [159–161], the perturbative renormalized anisotropy is

$$\begin{aligned}\xi^{-1} = c(a, a_0)\delta_\tau &\sim \left[\frac{1 - c_s(\xi)g_H^2}{1 - \frac{c_t(\xi)+c_s(\xi)}{2}g_H^2}\right]\delta_\tau \\ &\approx \left[1 + \frac{c_t(\xi) - c_s(\xi)}{2}g_H^2(a, a_0) + O(g_H^4)\right]\delta_\tau. \end{aligned} \tag{2.48}$$

Even without a functional form for $c_i(\xi)$, one can see that solving Eq. (2.48) self-consistently for ξ will break $a_0 \propto \delta_\tau$. For $SU(N)$ in 3 and 4 dimensions, $c_+(\xi) \equiv c_t(\xi) + c_s(\xi) \approx O(10^{-2})$ and $c_-(\xi) \equiv c_t(\xi) - c_s(\xi) \approx O(10^{-1})$ [159–161] – suggesting that the nonlinear

renormalization is generically small. While the exact functions $g_H^2(a, a_0), c_i(\xi)$, depend upon the metric, the form of Eq. (2.48) should remain unchanged. It is possible to investigate Eq. (2.48) in Minkowski space by rewriting it as $a_t = c(a, a_t)a\delta_t$. For the case of $g_H^2 = 1.25$ plotted in Fig. 2.5, one sees that a_t has a clear δ_t^2 dependence. Furthermore, Fig. 2.6 shows that the linear dependence of a_t upon δ_t is a g_H^2 dependent function. Together, these demonstrate the renormalization of a_t with respect to the bare coupling g_H and the trotter step δ_t. Although for our toy model with two spatial plaquettes we cannot extract the spatial scale a from numerical results, we can relate a to the running of g using the perturbative results [179]

$$a\Lambda = \exp\left(-\frac{1}{2b_0 g^2}\right)(b_0 g^2)^{-\frac{b_1}{2b_0}}(1 + O(g^2)). \tag{2.49}$$

In the above, b_0, b_1 are the standard g^3, g^5 coefficients in the perturbative β function. Altogether, to extract physical properties from quantum simulations, we must first determine both scales explicitly.

2.5.2 Comparison of Schemes for Scale Setting

To reduce the quantum resources for lattice calculation, we determine the scale using the Euclidean data following the procedure proposed in Sec. 2.3. As a demonstration, we will focus on the temporal lattice spacing and show its determination using **Scheme A** and **Scheme B**.

We solve the eigenvalues of the Euclidean transfer matrix built from K_{KS} and V_{KS} in Eq. (2.43). By taking the logarithm of these eigenvalues, we could extract the energies of the spectra on a Euclidean space-time, with the ground state energy normalized to zero. The observable $a_0 m_{1\times 1}$ is the energy corresponding to the 2nd excited state. With the set of bare couplings $1/g_H^2 = [0.8, 3.0]$ and $\delta_\tau = [0.5, 0.01]$, we obtain $a_0 m_{1\times 1}$ and in addition we apply an error of 1% to $a_0 m_{1\times 1}$ for any bare coupling and a_0 used, in order to mimic the measurement error using classical Monte Carlo simulations. Then we do a 2D fit to get the

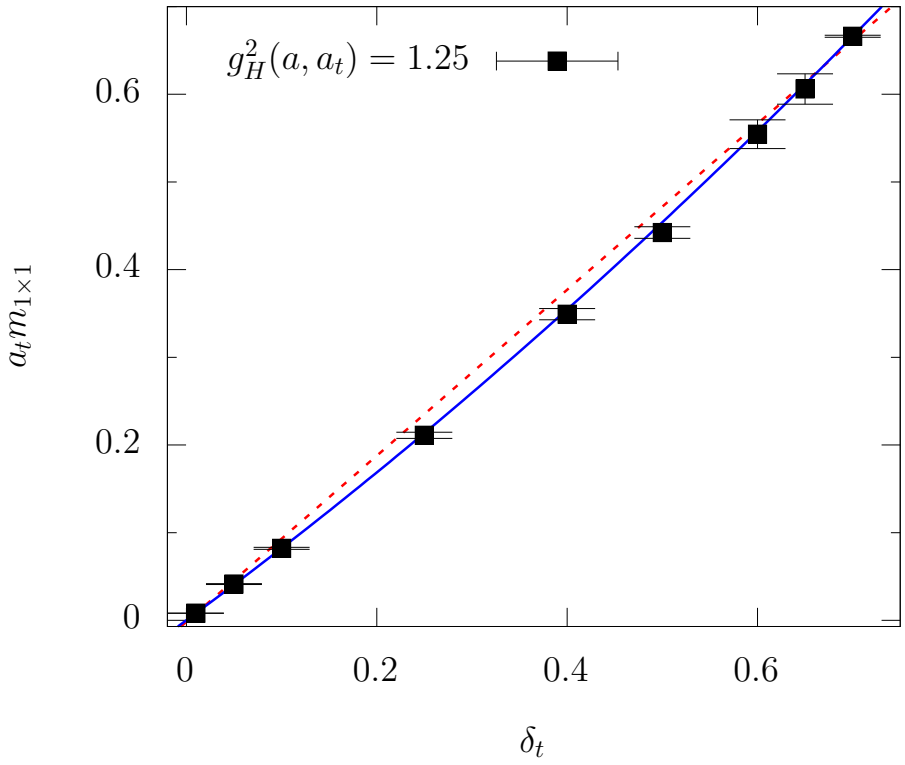

Figure 2.5: $a_t m_{1\times 1}$ vs δ_t for $g_H^2 = 1.25$. The dashed (solid) lines indicate a linear (quadratic) fit to the data. The poor linear fit (χ^2/d.o.f = 40.2) demonstrates that a_t is not proportional to δ_t as might be naively expected. χ^2/d.o.f = 1.1 for the quadratic fit.

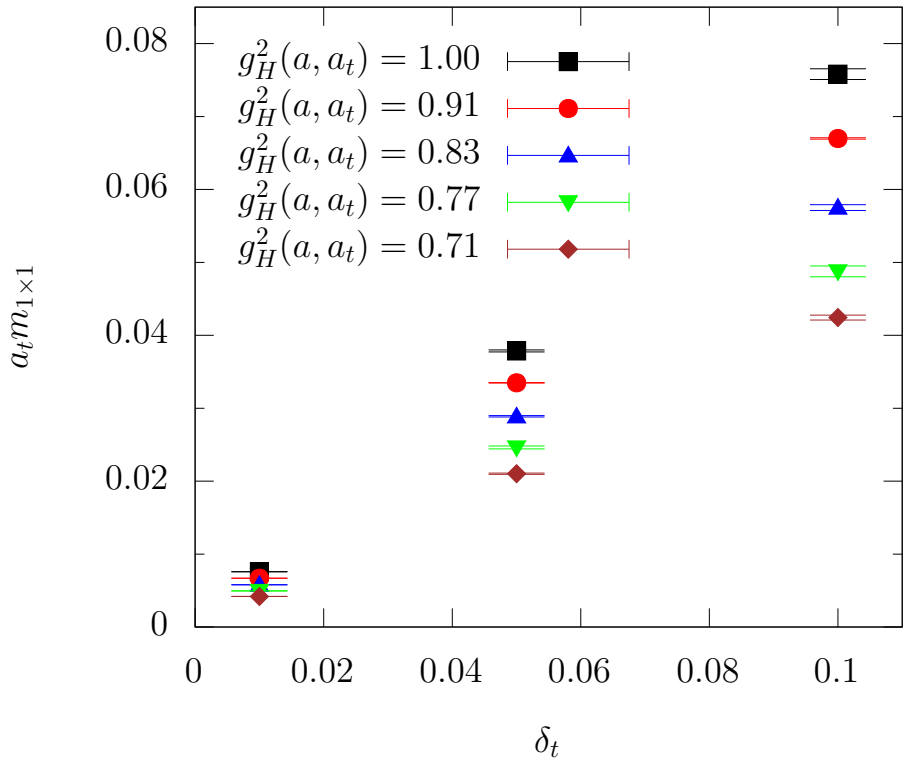

Figure 2.6: $a_t m_{1\times1}$ vs δ_t for different g_H^2. Notice that renormalization of a_t is clearly g_H^2 dependent.

functional dependence of $a_0 m_{1\times 1}$ on both δ_τ, g_H^2 as:

$$a_0 m_{1\times 1}(\delta_\tau, g_H^2) \;=\; \delta_\tau\Big(f_1(g_H^2) + f_2(g_H^2)\delta_\tau^2\Big) \tag{2.50}$$

Given that spatial lattice spacing a is related to g_H^2 via the relation in Eq. (2.49) and f_i functions should be power-law expansions of a, we use the following functional form for the 2D fitting of $a_0 m_{1\times 1}$

$$f_i(g_H^2) = \sum_n a_{i,n}\bigg(\exp\Big(-\kappa_0/g_H^2\Big)\frac{1}{g_H^{2\kappa_1}}\bigg)^n. \tag{2.51}$$

The fitted $a_0 m_{1\times 1}$ (χ^2/d.o.f = 1.3) is at most 3% away from their truth value at 68% C.L.., with n taken to be 3 for f_1 and 2 for f_2 to achieve the aforementioned χ^2/d.o.f. With this, we can then analytically continue with either scheme. In Fig. 2.7, the percent systematic error for both schemes compared to $a_t m_{1\times 1}$ computed by diagonalizing $U(a_t)$ in Sec. 2.5.1 (which agree with Tab. 2.2). The colored region shows the errors from the 1σ band in the Euclidean fitting. For the three g_H^2 used in Fig. 2.7, the errors $\epsilon \leq 2\%$ at 68% C.L., with a weak dependence on δ_τ.

As expected, **Scheme A**, **B** give precise evaluations of $a_t m_{1\times 1}$ at small δ_t. When δ_t gets larger, the BCH errors of **Scheme A** should increase as δ_t^2. BCH errors get smaller for smaller g_H^2, as which lowers the error bound parameter M. As shown in Fig. 2.7, for $g_H^2 \leq 0.33(\epsilon \sim M)$, **Scheme A** provides a better estimation of the lattice scales for the whole region of $\delta_t < 0.5$. The errors from the analytical continuation of **Scheme B** barely increase for larger values of δ_t, and are in principle less sensitive to g_H^2 as expected. For the assumed precision in the Euclidean data and the fitting procedure, the error, ϵ, is slightly larger for the small g_H^2 region and altogether a delayed growth in the errors is maintained for $g_H^2 \geq 0.71$. One can conclude that if g_H^2 is not particularly small, **Scheme B** is more likely to render the lowest errors in the scale determination. In both cases, the observed 2% errors

are well within Eq. (2.41) and Eq. (2.42), which predict a 10% error bound for $\delta_t \leq \delta_t^{A(B)}$ shown in Tab. 2.1.

Once the measurement of the renormalized spatial lattice spacing is allowed when considering sufficiently large systems, one can obtain the renormalized spatial lattice spacing similarly using only Euclidean data.

2.5.3 Approaching the Continuum

In Euclidean LFT, one uses a, a_0 for extrapolating to the continuum limit. This is because performing extrapolations in terms of the bare parameters requires either very higher order fit functions (and therefore many calculations) or calculations with very small g_H and δ_τ (at large computational cost). Instead, using a, a_0 is an extrapolation in nonperturbative variables, so the bare couplings can be much larger and the fit functions simpler. The same should be true in Minkowski spacetime. In principle, one can approach the continuum along any trajectory as a function of a, a_t, but experience from Euclidean LFT [165, 168], suggests that taking a trajectory of fixed-ξ_t would smoothly and efficiently extrapolate to the continuum limit for Minkowski LFT. In approximations to $U(t)$ other than trotterization [85–88], definitions for a nonperturbative scale like a_t are currently unknown, making the extrapolation to the continuum nontrivial.

In the continuum limit $a, a_t \to 0$ and thus $a_t m_i$ vanishes. One must instead explore finite physical quantities such as $a_t m_i / a_t m_{1\times1}$. Due to the smallness of our lattice, the only states which mix with $|\psi_2\rangle$ are from cutoff effects which have $a_t m_i / a_t m_{1\times1} \to \infty$. Therefore, we perform another fit to $\langle \mathcal{O}_{2\times1}(t) \rangle$ from which we extract a second physical mass, $a_t m_{2\times1}$. The initial state for this purpose is constructed with $i = 13$. With these, we can study different approaches to the continuum limit. As the scales set from real-time evolution are already available (Tab. 2.2) and **Scheme B** gives comparable precision, in the following, we use a_t from Tab. 2.2. Observe that, since the difference between **Schemes A** and **B**

are polynomials of the lattice spacing, it is reasonable to expect that formulating **Scheme A** with some assumptions on the extrapolation function would lead to the same continuum limit as the one we are considering here. We point out that the precision of the spacings extracted from real-time evolution would be much worse when noise is included.

Numerically, the first trajectory to approach the continuum is to first take $a_t \to 0$ (the Hamiltonian limit) then take $a \to 0$. Since the lattice spacing errors of $H(a, a_t)$ are $O(a^2, a_t^2)$, we fit the mass ratio to

$$\frac{a_t m_{2\times 1}}{a_t m_{1\times 1}} = \kappa_0 + \kappa_2 (a_t m_{1\times 1})^2 \tag{2.52}$$

In Fig. 2.8 and Fig. 2.9, we show these best fit lines of Eq. (2.52) to the data points extracted from `qasm` and `state_vector`. The values of κ_0 correspond to the Hamiltonian limit value of the mass ratio, and we tabulate them in Table 2.3. We find good agreement between the κ_0 in Tab. 2.3 and those calculated by direct diagonalization of the Hamiltonian with $\delta_t = 0$ for different g_H^2.

From Fig. 2.8, we could see that the difference for $a_t m_{2\times 1}/a_t m_{1\times 1}$ is only 8% between its value at $\delta_t = 0.5$ and the Hamiltonian limit for $g_H^2 = 1.11$, while from Fig. 2.4, for the same value of g_H^2 and δ_t, the $\langle \mathcal{O}_{1\times 1}(t) \rangle$ could differ from the Hamiltonian limit by up to 20%. The deviation in $a_t m_{2\times 1}/a_t m_{1\times 1}$ represents BCH corrections to the eigenvalues and the latter one is the correction to wavefunction. Thus less resources (larger trotterization step) could be needed to control the error of $a_t m_{2\times 1}/a_t m_{1\times 1}$ below certain threshold.

Assuming errors scaling as $O(a^2)$ and using Eq. (2.49), we can fit the κ_0 in Tab. 2.3 to the continuum limit using

$$\left.\frac{a_t m_{2\times 1}}{a_t m_{1\times 1}}\right|_{a_t \to 0} = \lambda_0 + \lambda_1 e^{-\lambda_2/g_H^2} (g_H)^{\lambda_3}. \tag{2.53}$$

In contrast to extrapolating in a_t, the reliability of this extrapolation depends much more sensitively on being in the perturbative regime, otherwise Eq. (2.49) receives large corrections

and our functional form will be inadequate. So from Eq. (2.53), we must perform the nonlinear fit in g_H^2 which introduces complicated correlations between the fitting parameters. Despite these limitations, we find that the continuum limit result of $\lambda_0 = 2.03(4)$ agrees with the continuum value $m_{2\times1}/m_{1\times1} = 2$ computed from the direct diagonalization of the Hamiltonian with $g_H^2 \sim 0$ and $\delta_t = 0$. The mass ratio in the continuous time limit, κ_0 in Tab. 2.3 (black points), and the best fit line using Eq. 2.53 are found in Fig. 2.10 (black line and grey shaded region for 68% C.L..).

The number of trotter steps N (and therefore gate costs) is proportional to δ_t^{-1}. Clearly therefore, it is an undesirable feature to first take the Hamiltonian limit $a_t \to 0$ ($\delta_t \to 0$) and then the continuum limit $a \to 0$. Instead of working at fixed a, while decreasing δ_t, one can work at fixed $\xi_t = \frac{a}{a_t}$ and then one could directly approach the continuum limit $a, a_t \to 0$ through this trajectory. Up to a^2 order, the extrapolation in terms of the bare coupling, would be of analogous functional form as that on the right-hand of Eq. (2.53), with the finite-ξ_t effects entering the fitting parameters. It is thus important to explore how to define the finite ξ_t trajectory. One could perform this tuning on the quantum computer. This would proceed by computing both a_t, a or ξ_t using some physical observables (e.g. Wilson loops or dispersion relations) and then adjust the bare parameters until one has a fixed ξ_t trajectory. This procedure requires multiple quantum simulations to be performed – albeit at larger δ_t then an extrapolation to the Hamiltonian limit requires and only the scale-setting observable needs to be computed. But, as demonstrated, we can reliably extract the dependence of the scales a, a_t on δ_t and g_H^2 by analytical continuation using **Scheme B**. We can then directly invert these relations to find the δ_t and g_H^2 for a fixed ξ_t avoiding the quantum computer entirely for scale-setting.

Given the smallness of our system, we are unable to extract a or the corresponding ξ_t to determine a set of δ_t and g_H^2. This forces us to consider some approximations. While the previous discussions demonstrate renormalization, as the nonperturbative renormalization

effects partially cancel out [160], we expect that the renormalization of ξ_t is milder than that of a, a_t individually. Therefore, we can approximate the fixed ξ_t trajectory as fixed δ_t. In Fig. 2.10, we show altogether the extrapolation to the continuum limit through the Hamiltonian limit (gray line and black dots), as well as two fixed values of $\xi_t \approx \{10, 2\}$ to highlights the power of fixed ξ_t trajectories in achieving the continuum limit results. Indeed, following the trajectory of $\xi_t \approx 10$ (red circle), we can successfully reach the correct continuum limit with clear advantages over the Hamiltonian extrapolation method. For $\xi_t \approx 10$, the needed number of data point simulations is reduced by 67% when comparing to the Hamiltonian limit procedure that requires all the measurements shown in Fig. 2.8 and Fig. 2.9. In addition, the circuit depth is greatly reduced through avoiding small trotterization steps, e.g. $\delta_t < 0.1$. In Fig. 2.10, we further investigate using an even smaller $\xi_t \approx 2$, hence $\delta_t = 0.5$ (blue triangles), which implies a further improvement on the circuits depth demands. Due to the large uncertainties from quantum simulations as represented by the large error bars from Fig. 2.10, we calculate the $\frac{a_t m_{2\times1}}{a_t m_{1\times1}}$ through explicit diagonalization of the time evolution operator at fixed $\xi_t \approx 1/\delta_t = 2$. We find that the continuum limit is also successfully reached for this large value of trotter step. Although multiple simulations are needed to control the measurement uncertainties on a quantum computer, this highlights the advantages of fixed-ξ calculations in avoiding larger errors from enhanced circuit depth.

2.6 Continuous limit for discrete group with Wilson action

In this appendix, we will show the subtleties in taking the Hamiltonian limit $a_0 \to 0$ constructed from the Wilson action of a discrete gauge group, relying on the spectra of the kinetic part of the transfer matrix, which could be solved using the character expansion - Fourier transformation to the character basis. Taking D_n group as an example (with n even),

its irreducible representations ρ_r are as follow:

$$\begin{aligned}
\rho_{1,1}(j,m) &: 1 \qquad \rho_{1,2}(j,m) : (-1)^m \\
\rho_{1,3}(j,m) &: (-1)^j \quad \rho_{1,4}(j,m) : (-1)^{m+j} \\
\rho_{2,k}(j,m) &: \exp\left(i\frac{2\pi j}{n}k\sigma_z\right)\sigma_x^m
\end{aligned} \tag{2.54}$$

with $j \in [0,...,n-1], m \in \{0,1\}$ defining the elements of the group and $k \in \{1,2,...\frac{n}{2}-1\}$ indexing the different dimension-2 irreducible representations.

The kinetic part of transfer matrix is constructed in the faithful irreducible representation of D_n: $\rho_{2,1}(j,m)$, to ensure its positivity [82]. Consider a single link, say the first link U_1, it takes values of $\rho_{2,1}(g_i) \equiv \rho_{2,1}(j,m)$, with $i=1$ representing the identity group element of $j=m=0$. Using character expansion, the kinetic part of the transfer matrix for the first link T_K^1 can be explicitly written as:

$$\begin{aligned}
T_K^1(i,i') &= \exp\left(\beta_t \,\mathrm{Re}\,\mathrm{Tr}\left[\rho_{2,1}^\dagger(g_i)\rho_{2,1}(g_{i'})\right]\right) \\
&= \sum_r d_r c_r \,\mathrm{Tr}\Big[\rho_{2,1}^\dagger(g_i)\rho_{2,1}(g_{i'})\Big],
\end{aligned} \tag{2.55}$$

with d_r the dimension of the r representation. The coefficients for the modes in the irre-

ducible representation r are given by $c_r = \sum_{i=1}^{2n} \frac{1}{d_r} \mathrm{Tr}\Big[\rho_r(g_i^\dagger)\Big] T_K^1(i,1)$, explicitly as:

$$
\begin{aligned}
c_{1,1} &= \sum_{j=0}^{n-1} (e^{2\beta_t \cos\left(\frac{2j\pi}{n}\right)} + 1) \\
c_{1,2} &= \sum_{j=0}^{n-1} (e^{2\beta_t \cos\left(\frac{2j\pi}{n}\right)} - 1) \\
c_{1,3} &= \sum_{j=0}^{n-1} (-1)^j (e^{2\beta_t \cos\left(\frac{2j\pi}{n}\right)} + 1) \\
c_{1,4} &= \sum_{j=0}^{n-1} (-1)^j (e^{2\beta_t \cos\left(\frac{2j\pi}{n}\right)} - 1) \\
c_{2,k} &= \sum_{j=0}^{n-1} \cos\left(\frac{2j\pi}{n} k\right) e^{2\beta_t \cos\left(\frac{2j\pi}{n}\right)}
\end{aligned}
\tag{2.56}
$$

and is inherently positive from the positivity of T_K^1 when $\beta_t > 0$ for finite n. Notice that in Eq. (2.56), the group elements with $m = 1$ contribute only to the second piece in each summation of c_r for $d_r = 1$ and do not contribute to $c_{2,k}$. For the D_4 group considered in Sec. 2.5, we have

$$
\begin{aligned}
c_{1,1} &= 6 + e^{2\beta_t} + e^{-2\beta_t}, \quad c_{2,1} = e^{2\beta_t} - e^{-2\beta_t} \\
c_{1,2} &= c_{1,3} = c_{1,4} = -2 + e^{2\beta_t} + e^{-2\beta_t}.
\end{aligned}
\tag{2.57}
$$

The corresponding K_{KS} after normalizing the ground state energy to zero in the character basis $|r, l\rangle$ is written as:

$$
K_{\mathrm{KS}} = \frac{1}{a_0} \sum_r \sum_{l=1}^{d_r^2} \log\left(\frac{c_{1,1}}{c_r}\right) |r, l\rangle \langle r, l| \tag{2.58}
$$

where l represents the degree of degeneracy of the d_r^2 modes in the r irreducible representation. The trotterization error we discussed in Sec. 2.4 would be proportional to the maximal

eigenvalues of $K_{\rm KS}$.

Recall that $\beta_t = a/(g_t^2 a_0) = 1/(g_H^2 \delta_\tau)$. In the small a_0 region, the contribution to the c_r in Eq. (2.57) are all dominated by the $e^{2\beta_t}$ terms, which quantify the contribution from the identity group element ($j = m = 0$). Taking the limit $a_0 \to 0$ for discrete groups would result in degenerate spectra:

$$\lim_{a_0\to 0} \frac{1}{a_0} \log \frac{c_{1,1}}{c_r} \sim \lim_{a_0\to 0} \frac{f(r)}{a_0} e^{-2\beta_t} = 0 \tag{2.59}$$

with $f(r = \{1,2\},\{1,3\},\{1,4\}) = 8$ and $f(r = \{2,1\}) = 6$. However, related to the observable $\frac{a_t m_{2\times 1}}{a_t m_{1\times 1}}$ in our study of Sec. 2.5, one should consider the energy ratios, say:

$$\lim_{a_0\to 0} \frac{1}{a_0} \log \frac{c_{1,1}}{c_{1,2}} \Big/ \left(\frac{1}{a_0} \log \frac{c_{1,1}}{c_{2,1}} \right) = \frac{4}{3} \tag{2.60}$$

which instead approach a finite value in the $a_0 \to 0$ limit. To obtain non-degenerate spectra and have the above energy ratios fixed, one need to view β_t and β_s as parameters, without referring to their dependence on a and a_0 in Eq. (2.2). The continuous time limit should be taken while keeping [142]:

$$\lim_{a_0\to 0} \frac{1}{\beta_s} \exp(-\beta_t) \;\; = \;\; g_d^2(a) g_s^2, \tag{2.61}$$

where $g_d^2(a)$ is some finite constant for a given spatial lattice spacing. It then follows that:

$$\lim_{a_0\to 0} \frac{1}{a_0} \log \frac{c_{1,1}}{c_r} \sim \lim_{a_0\to 0} \frac{f(r)}{a_0} e^{-2\beta_t} = f(r) \frac{g_d^2(2a)}{2a} \tag{2.62}$$

For the numerical part of our simulation in Sec. 2.5, we fix $\delta_t = \delta_\tau = 1$ and the corresponding

dimensional spectra in the small g_H^2 limit is given by:

$$\frac{1}{ca}\log\left(\frac{c_{1,1}}{c_r}\right) \sim \frac{f(r)}{ca}\exp\left(-\frac{2}{g_H^2}\right) \tag{2.63}$$

which is the spectra in the above Hamiltonian limit by identifying $\exp\left(-\frac{2}{g_H^2(a)}\right)/c = g_d^2(2a)/2$. This relation also indicates that for the same spatial lattice spacing measured, the bare coupling for the the discrete group should be exponentially suppressed than the bare coupling for a continuous group.

2.7 The approximation of truncating at leading order commutators in Eq. (2.38)

In this appendix, we will justify that within the region of Eq.(2.39), the BCH operators beyond the leading order are negligible and therefore Eq. (2.38) holds.

Define $H(k,v)$ as a commutator with k powers of $K_{\rm KS}$ and v powers of $V_{\rm KS}$. There are at most $4v$ links in $K_{\rm KS}$ and $2(d-1)k$ plaquettes in $V_{\rm KS}$ that can contribute to $[\overline{H}_{K,V}, H(k,v)]$. Therefore,

$$\|[K_{\rm KS}, H(k,v)]\| \leq 8vg_H^2\|\hat{l}^2\|\|H(k,v)\| \tag{2.64}$$

$$\|[V_{\rm KS}, H(k,v)]\| \leq 4(d-1)kg_H^{-2}d_U\|H(k,v)\| \tag{2.65}$$

With $r=s=1$, one has $[K_{\rm KS}, V_{\rm KS}]$ which can be bounded with $\|[A,B]\| \leq 2\|A\|\|B\|$,

$$\begin{aligned}\|[K_{\rm KS}, V_{\rm KS}]\| &\leq 2\|K_{\rm KS}\|2(d-1)d_U g_H^{-2} \\ &= \mathcal{N}_{link}4(d-1)d_U\|\hat{l}^2\|\end{aligned} \tag{2.66}$$

When trotterizing $U(t)$ to second order, the leading order (LO) BCH terms in H' are given

by $k+v=3$, with the next-to-leading (NLO) order having $k+v=5$. While each NLO term has a slightly different bound, they all satisfy

$$\begin{aligned}&\|H(k+v=5)\| \leq \\ &4\max\left\{4(d-1)g_H^{-2}d_U, 8g_H^2\|\hat{l}^2\|\right\}^2 \|H(k+v=3)\|\end{aligned} \tag{2.67}$$

The coefficients c_k of $H_{NLO} \equiv \delta^4 \sum_k c_k \|H(k,5-k)\|$ are of $O(10^{-2})$, with the largest being $1/180$ [180]. Therefore the ratio of H_{NLO} to H_{LO} is

$$\frac{H_{NLO}}{H_{LO}} \lesssim O(1)\frac{|\delta|^2}{(\max\delta)^2} \tag{2.68}$$

where $\max\delta = 1/\max\left\{4(d-1)g_H^{-2}d_U, 8g_H^2\|\hat{l}^2\|\right\}$. When $|\delta| \leq \max\delta$ then Eq. (2.68) is smaller than $O(1)$. Thus, the NLO contribution is negligible and the approximation of Eq. (2.38) is valid.

2.8 The proof of the error bound for Scheme B

For any δ within the radius $|\delta| \leq \max\delta$, one can decompose the analytic continuation error:

$$\begin{aligned}|\lambda_f(\delta, g_H^2) - \lambda(\delta, g_H^2)| \leq |\lambda_f(\delta, g_H^2) - \lambda_f(0, g_H^2)| \\ +|\lambda(\delta, g_H^2) - \lambda(0, g_H^2)| + |\lambda_f(0, g_H^2) - \lambda(0, g_H^2)|\end{aligned} \tag{2.69}$$

The term $|\lambda(\delta, g_H^2) - \lambda(0, g_H^2)|$ is simply the trotter error, bounded by $|\lambda(\delta, g_H^2) - \lambda(0, g_H^2)| \lesssim M/2$. We further impose a constraint $|\lambda_f(\delta, g_H^2) - \lambda_f(0, g_H^2)| \leq M/2$ on the fitting function $\lambda_f(\delta, g_H^2)$.

The last term in Eq. (2.69) is bounded by the Euclidean precision, $|\lambda_f(0, g_H^2) - \lambda(0, g_H^2)| \leq$

$\epsilon_B \ll M$. Then there is a loose bound on $|\lambda_f(\delta, g_H^2) - \lambda(\delta, g_H^2)|$:

$$|\lambda_f(\delta, g_H^2) - \lambda(\delta, g_H^2)| \lesssim M + \epsilon_B \tag{2.70}$$

We finish the proof with the following lemma, which is a specific case of Lemma 1 in [171]. Let $\lambda(\delta), \lambda_f(\delta)$ be analytic in the half-disk region $\Omega = \{\delta : \operatorname{Im}\delta \geq 0, |\delta| \leq \max\delta\}$ with the bounds $|\lambda - \lambda_f| \leq A$ for any $\delta \in \Omega$ and $|\lambda - \lambda_f| \leq \epsilon$ on the lower boundary $\operatorname{Im}\delta = 0$. Then for any $\delta \in \Omega$,

$$|\lambda(\delta) - \lambda_f(\delta)| \leq \epsilon \left(\frac{A}{\epsilon}\right)^{\operatorname{Re}\frac{4}{\pi}\arctan\frac{\delta}{i\max\delta}} \tag{2.71}$$

Proof. Define

$$w(\delta) \equiv \frac{4}{\pi}\arctan\frac{\delta}{i\max\delta} \tag{2.72}$$

With $\delta \in \Omega$, the range of w is the infinite strip $S = \{w : 0 \leq \operatorname{Re} w \leq 1\}$. Define v and h as follows

$$v \equiv \ln\frac{A}{\epsilon} \tag{2.73}$$

$$h(\delta) \equiv \frac{e^{-vw(\delta)}}{A}\left[\lambda(\delta) - \lambda_f(\delta)\right] \tag{2.74}$$

The function $h(\delta)$ is analytic in the half-disk region Ω. According to the maximum modulus principle, the maximum $|h(\delta)|$ can only be on the boundary of Ω, which consists of two parts

$\operatorname{Im}\delta = 0$ where $|\lambda_f - \lambda| \leq \epsilon$ and $|\delta| = \max\delta$ where $\operatorname{Re} w(\delta) = 1$.

$$|h(\delta)|_{\operatorname{Im}\delta=0} = \frac{1}{A}|\lambda(\delta) - \lambda_f(\delta)|_{\operatorname{Im}\delta=0} \leq \frac{\epsilon}{A} \tag{2.75}$$

$$\begin{aligned} |h(\delta)|_{|\delta|=\max\delta} &\leq |e^{-vw(\delta)}|_{|\delta|=\max\delta} \\ &= \left(\frac{\epsilon}{A}\right)^{\operatorname{Re} w(\delta)_{|\delta|=\max\delta}} = \frac{\epsilon}{A} \end{aligned} \tag{2.76}$$

Therefore, $|h(\delta)| \leq \frac{\epsilon}{A}$ for any $\delta \in \Omega$. Using the definition 2.74, we obtain the following upper bound.

$$|\lambda(\delta) - \lambda_f(\delta)| = A|h(\delta)|e^{v\operatorname{Re} w(\delta)} \leq \epsilon \left(\frac{A}{\epsilon}\right)^{\operatorname{Re} w(\delta)} \tag{2.77}$$

For $\delta = i\delta_t$, we have $\operatorname{Re} w(i\delta_t) = \frac{4}{\pi}\arctan\frac{\delta_t}{\max\delta}$. In Eq. (2.71), replace ϵ with ϵ_B and the loose upper bound A with $(M + \epsilon_B)$, as Eq. (2.70) suggests, and one gets the result of Eq. (2.42).

2.9 Conclusions

The natural construction of quantum field theories on quantum computers is as a lattice-regularized theory. Any meaningful calculation must therefore be renormalized and taken to the continuum limit before comparison to experiments can be made. As we have discussed, this involves many hurdles and it will not be easy. Typically quantum simulations are constructed within the Hamiltonian formalism where a spatial lattice with spacing a is time-evolved. Further approximations are required, as the time evolution operator $\mathcal{U}(t)$ built from the Hamiltonian usually cannot be efficiently implemented.

In this chapter, we have tackled three important issues related to the simulations of Minkowksi lattice field theories on quantum computers. Firstly, we discussed how renormalization in the form of a temporal lattice spacing a_t arises from trotterizating $\mathcal{U}(t)$. Secondly, by relating this trotterized time evolution operator to the Euclidean transfer matrix, we

propose two different schemes using analytical continuation to set the Minkowski lattice spacings. The most straightforward scheme is to simply equate the Euclidean lattice spacings to those in the real-time calculation (Scheme A). This scheme introduces $O(\delta_t^2)$ errors in addition to the statistical errors in the Euclidean calculations. Our second method (Scheme B) can correct the $O(\delta_t^2)$ errors of Scheme A by analytically continuing the best-fit function of the Euclidean spacings. We have derived conservative bounds on the systematic errors for these schemes for small δ_t, and a loose constraint on the error of the fit to take advantage of Scheme B. This enables us to reduce the requirements for quantum resources in the scale setting procedure. Thirdly, we show that by taking a fixed anisotropic-ξ_t approach to the continuum limit, one can further reduce the number of simulations with the added benefit of shallower circuits and lower required gate fidelities. We demonstrated these ideas for a $2+1$D, discrete non-Abelian D_4 model using `qiskit` noiseless simulators.

Several follow-ups have been made to the results in this chapter. In particular, the scale-setting procedure has been tested for $\mathbb{Z}_2$ gauge theories in 1+1, allowing for the explicit calculation of a[181]. Further, the viability of the analytical continuation has been tested by explicit calculations matching the Euclidean and Minkowski lattice results in the continuous-time limit [57, 182]. Additionally, since the quantum resources increase as $a_t, a \to 0$, improved Hamiltonians that account for both lattice effects and quantum noise could accelerate extrapolation to the continuum approach while reducing the quantum resources required, which is the content of the next chapter.

Table 2.2: Numerical results for lattice masses $a_t m_{1\times1}$ and $a_t m_{2\times1}$ for the bare couplings g_H^2 and δ_t studied here. Rows above (below) the line indicate `qasm` (`state_vector`) results.

g_H^2	δ_t	$a_t m_{1\times1}$	$a_t m_{2\times1}$
1.25	0.70	0.6663(11)	—
1.25	0.65	0.606(17)	—
1.25	0.60	0.554(16)	—
1.25	0.50	0.442(6)	1.120(15)
1.25	0.40	0.349(7)	—
1.25	0.25	0.211(4)	0.575(5)
1.25	0.10	0.0821(11)	0.2332(11)
1.25	0.05	0.0414(5)	—
1.25	0.01	0.00819(11)	—
1.18	0.5	0.446(13)	1.12(4)
1.18	0.25	0.207(3)	0.557(9)
1.18	0.1	0.0838(19)	0.223(3)
1.11	0.5	0.429(11)	1.016(11)
1.11	0.25	0.206(10)	0.518(11)
1.11	0.1	0.0832(7)	0.208(4)
1.05	0.5	0.404(14)	0.918(11)
1.05	0.25	0.1987(4)	0.478(5)
1.05	0.1	0.08103(14)	0.189(3)
1	0.1	0.07580(8)	0.1749 (7)
1	0.05	0.037855(14)	0.0883 (4)
1	0.01	0.007584(4)	0.017572(6)
0.91	0.1	0.06699(9)	0.1474(4)
0.91	0.05	0.03348(3)	0.07402(9)
0.91	0.01	0.0066953(14)	0.014835(4)
0.83	0.1	0.0575(4)	0.1250(6)
0.83	0.05	0.02889(10)	0.06266(16)
0.83	0.01	0.005791(8)	0.012493(14)
0.77	0.1	0.0488(8)	0.1051(8)
0.77	0.05	0.02462(19)	0.05230(15)
0.77	0.01	0.004948(8)	0.01049(3)
0.71	0.1	0.0424(3)	0.0885(3)
0.71	0.05	0.02102(9)	0.04387(7)
0.71	0.01	0.004191(9)	0.008753(7)

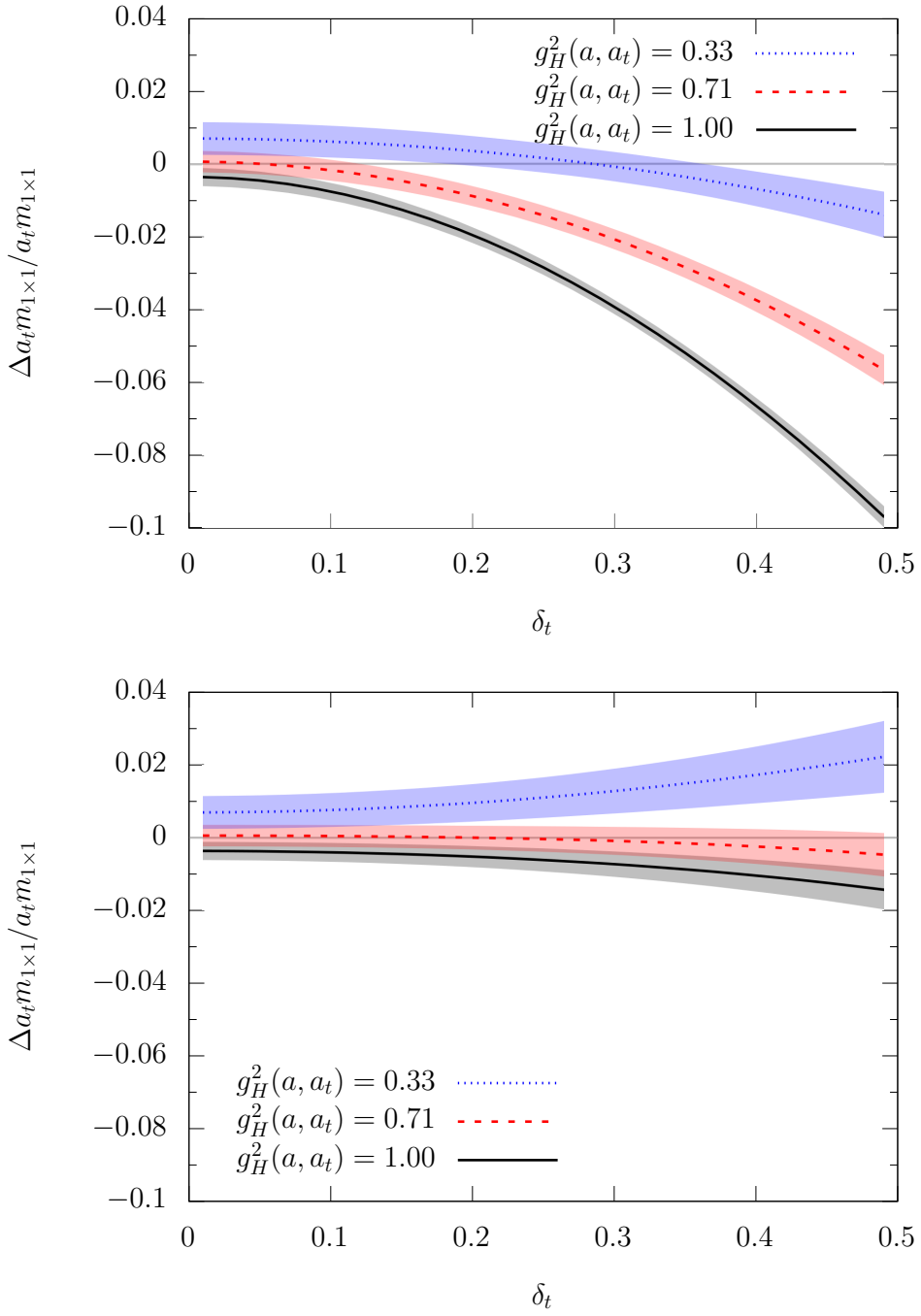

Figure 2.7: Errors with respect to the truth scale in a Minkowski calculation using **Scheme A** (left) and **Scheme B** (right), with the band showing the error from the 1σ region in the Euclidean fitting. We have assumed that the measurement precision in Euclidean spacetime could reach 1%. Together with fitting errors, we have $\epsilon \leq 2\%$ at 68% C.L. for the g_H^2 and $\delta_\tau = \delta_t$ used in this figure. For **Scheme A** we use $\Delta a_t m_{1\times1}$ from the fit, as ϵ is barely affected by the fitting procedure.

Table 2.3: Numerical results for the dimensionless ratio of lattice masses $a_t m_{2\times1}/a_t m_{1\times1}$ after extrapolating for fixed g_H^2 to the Hamiltonian limit, in comparison with the same quantities calculated using direct diagonalization of $V_{\mathrm{KS}} + K_{\mathrm{KS}}$. Rows above (below) the line indicate `qasm` (`state_vector`) results.

g_H^2	$\frac{a_t m_{2\times1}}{a_t m_{1\times1}}\|_{a_t\to0}$	$\frac{m_{2\times1}}{m_{1\times1}}\|_{a_t=0}$
1.25	2.83(4)	2.81
1.18	2.70(4)	2.68
1.11	2.511(13)	2.51
1.05	2.37(6)	2.40
1.00	2.321(9)	2.32
0.91	2.2159(3)	2.22
0.83	2.158(3)	2.15
0.77	2.1191(15)	2.11
0.71	2.0882(5)	2.09

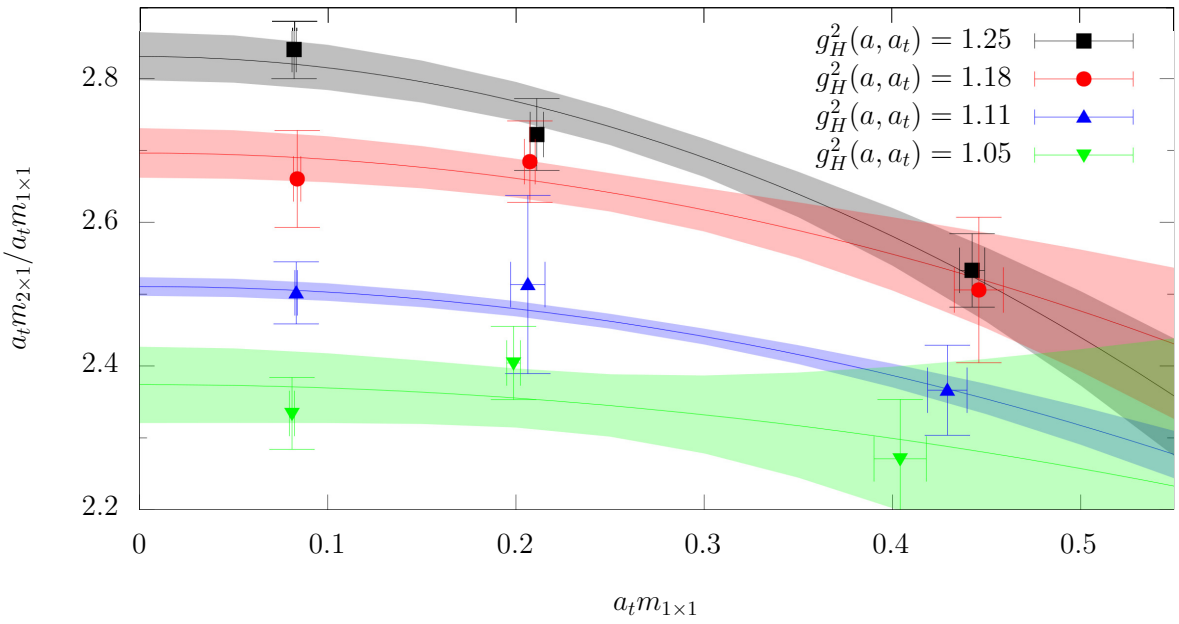

Figure 2.8: $a_t m_{2\times1}/a_t m_{1\times1}$ as a function of $a_t m_{1\times1}$ for a variety of $g_H^2(a, a_t)$. The data points are extracted from fixed δ_t results from a `qasm` calculation. For each g_H^2, we have $\delta_t = \{0.1, 0.25, 0.5\}$ from left to right. The solid lines reflect the best fit for a fixed $g_H^2(a, a_t)$. The colored bands are the 1σ uncertainties on the fits.

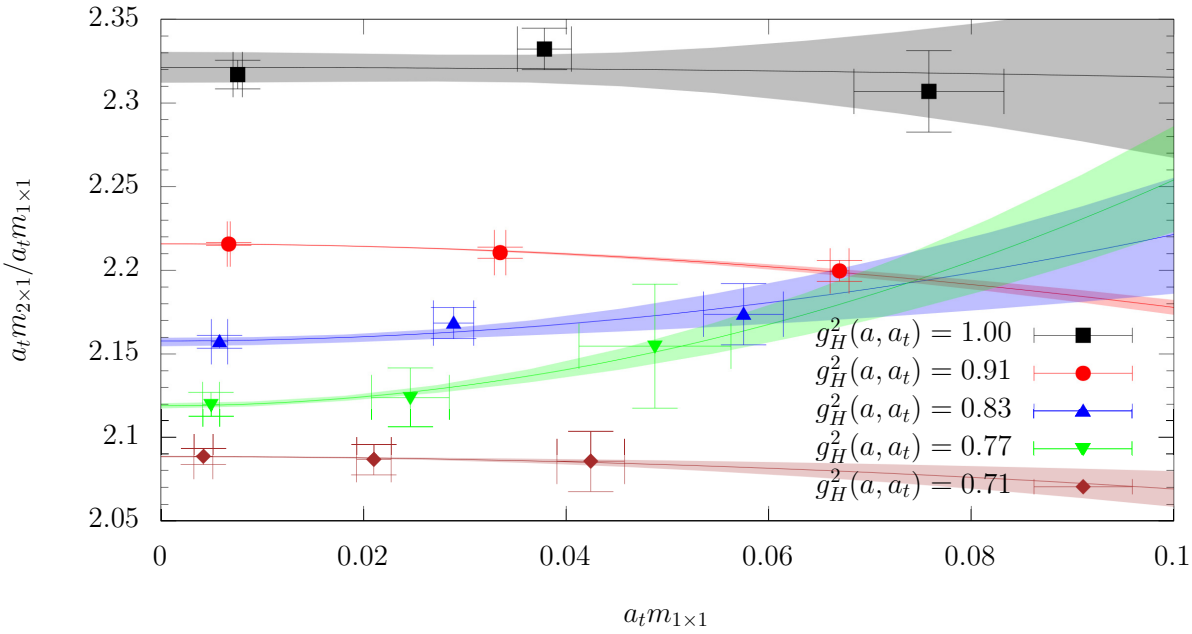

Figure 2.9: $a_t m_{2\times1}/a_t m_{1\times1}$ as a function of $a_t m_{1\times1}$ for a variety of $g_H^2(a,a_t)$. The data points are extracted from fixed δ_t results from a `state_vector` calculation. For each g_H^2, we have $\delta_t = \{0.01, 0.05, 0.1\}$ from left to right. The solid lines reflect the best fit for a fixed $g_H^2(a,a_t)$. The colored bands are the 1σ uncertainties on the fits.

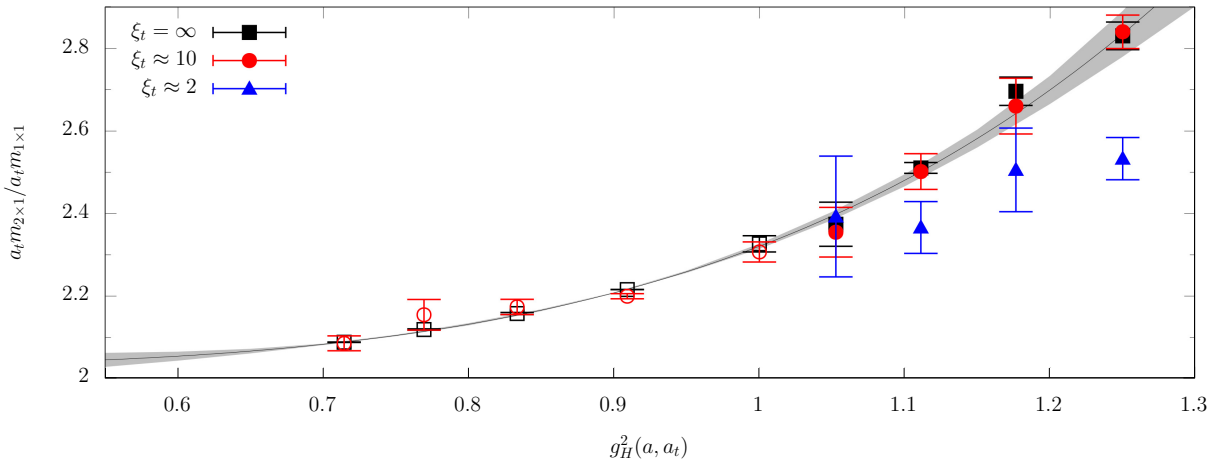

Figure 2.10: $am_{2\times1}/am_{1\times1}$ vs $g_H^2(a,a_t)$ for three continuum trajectories where ξ_t is approximately fixed. Closed and open symbols indicate `qasm` and `state_vector` results respectively. The black line is a best fit to the $\xi = \infty$ points with a 1σ uncertainty band.

CHAPTER 3

QUANTUM SIMULATIONS OF IMPROVED HAMILTONIANS

The historical success of Symanzik-improved lattice actions in classical simulations strongly suggest that improved Hamiltonians can dramatically reduce qubit and gate costs for the same physical limit results. This chapter presents a new direction for reducing quantum resources by using Hamiltonians with smaller discretization errors from finite differences. Quantum simulations can then be done at larger a, reducing the $\mathcal{O}((L/a)^d)$ qubits needed. We start with illustrating how to improve the commonly-used Kogut-Susskind Hamiltonian H_{KS} [68] in the Symanzik improvement program [183–185], then derive time-evolution operators for the improved terms and construct the corresponding quantum circuits, followed by an explicit demonstration for $\mathbb{Z}_2$.

For pure gauge theories, the classical Yang-Mills Hamiltonian can be written:

$$H_{\mathrm{YM}} = \frac{1}{2}\int \mathrm{d}^d x \,\mathrm{tr}\left[\mathbf{E}^2(\mathbf{x}) + \mathbf{B}^2(\mathbf{x})\right] \tag{3.1}$$

where $\mathbf{E}(\mathbf{x})$ and $\mathbf{B}(\mathbf{x})$ are the electric and magnetic field strengths with spatial components $E_i(\mathbf{x})$ and $B_i(\mathbf{x})$. Alternatively, the magnetic energy density can be written in terms of $F_{ij}(\mathbf{x})$, the spatial-spatial field strength tensor, as: $\frac{1}{2}\mathbf{B}^2(\mathbf{x}) = \frac{1}{2}\sum_{i<j} F_{ij}^2(\mathbf{x})$ with Latin indices indicating spatial directions as shown in Fig. 3.1. In terms of color components, $E_i(\mathbf{x}) = E_i^b(\mathbf{x})\lambda_b$, $B_i(\mathbf{x}) = B_i^b(\mathbf{x})\lambda_b$, with λ_b being generators of the gauge group. To ensure gauge invariance, lattice Hamiltonians are built from gauge links $U_i(\mathbf{x}) = e^{igaA_i(\mathbf{x})}$ connecting lattice site $\mathbf{x}$ to its neighbor in the i spatial direction, with g being the gauge coupling and $A_i(\mathbf{x})$ the lattice gauge field [186]. By replacing the magnetic field $B_i(\mathbf{x})$ term with the plaquettes $P_{ij}(\mathbf{x})$ (see Fig. 3.1 for $i = x$ and $j = y$) built from $U_i(\mathbf{x})$, and the

electric field $E_i(\mathbf{x})$ with the lattice electric field $L_i(\mathbf{x})$, one arrives at $H_{\rm KS}$ [68]:

$$H_{\rm KS} = K_{\rm KS} + V_{\rm KS}, \tag{3.2}$$
$$K_{\rm KS} = \sum_{\mathbf{x},i} \frac{g_t^2}{a} \,\mathrm{tr}\, L_i^2(\mathbf{x}),\; V_{\rm KS} = -\sum_{\mathbf{x},i<j} \frac{2}{g_s^2 a} \,\mathrm{Re}\,\mathrm{tr}\, P_{ij}(\mathbf{x}).$$

As temporal and spatial directions are treated differently, coupling g_t and g_s are introduced for the kinetic term $K_{\rm KS}$ and potential term $V_{\rm KS}$, respectively. The discrepancy between $H_{\rm KS}$ and $H_{\rm co}$ is of $\mathcal{O}(a^2)$, as seen by series-expanding P_{ij} with D_i denoting the covariant derivative:

$$P_{ij} = \mathbb{I} - \frac{g_s^2 a^4}{2}\left[F_{ij}^2 + \frac{a^2}{12} F_{ij}(D_i^2 + D_j^2)F_{ij} + \mathcal{O}(a^4)\right]. \tag{3.3}$$

For Symanzik improvement, one adds terms to $H_{\rm KS}$, and adjusts couplings to cancel the discretization errors [83, 84]. The above classical $\mathcal{O}(a^2)$ error from $F_{ij}(D_i^2 + D_j^2)F_{ij}$ can be cancelled by including the rectangle term $R_{ij}(\mathbf{x})$:

$R_{ij}(\mathbf{x}) =$ 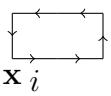 $= U^{-1}_{\mathbf{x},j} U^{-1}_{\mathbf{x}+\mathbf{j},i} U^{-1}_{\mathbf{x}+\mathbf{i}+\mathbf{j},i} U_{\mathbf{x}+\mathbf{2i},j} U_{\mathbf{x}+\mathbf{i},i} U_{\mathbf{x},i}.$ (3.4)

At the quantum level $\mathcal{O}(g_s^2 a^2)$ errors arise, requiring more terms like the six-link bent loop terms $C_{ijk}(\mathbf{x})$ (see Fig. 3.1).

The improved Hamiltonian can be written as $H_I = K_I + V_I$ with the improved potential term $V_I = \beta_{V0} V_{\rm KS} + \beta_{V1} V_{\rm rect} + \beta_{V2} V_{\rm bent}$ and the improved kinetic term $K_I = \beta_{K0} K_{\rm KS} + \beta_{K1} K_{2L}$ [84]. $V_{\rm rect}$ is defined as

$$V_{\rm rect} = \frac{2}{a g_s^2} \sum_{\mathbf{x},i<j} \mathrm{Re}\,\mathrm{tr}\left[R_{ij}(\mathbf{x}) + R_{ji}(\mathbf{x})\right], \tag{3.5}$$

and $V_{\rm bent}$ has analogous expressions to $V_{\rm rect}$. To cancel the $\mathcal{O}(a^2)$ errors in $K_{\rm KS}$, one adds

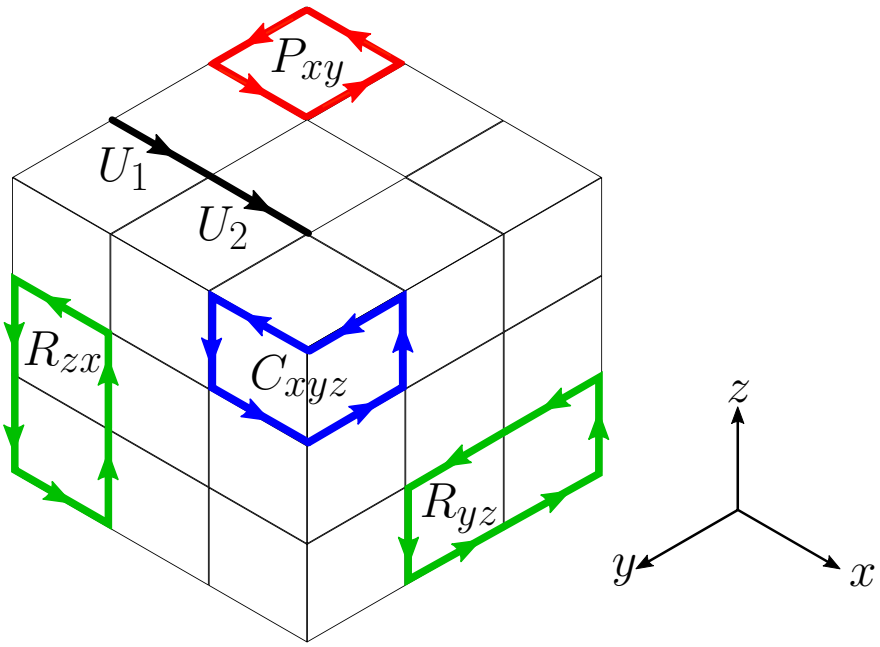

Figure 3.1: 3d lattice with example contributions to H_I: the plaquette P_{xy}, rectangles R_{yz} and R_{zx}, and the bent loop C_{xyz}, and the two links U_1 and U_2 used for K_{2L}.

the two-link term K_{2L}:

$$K_{2L} = \frac{g_t^2}{a} \sum_{\mathbf{x},i} \mathrm{tr}\left[L_i(\mathbf{x}) U_i(\mathbf{x}) L_i(\mathbf{x} + a\mathbf{i}) U_i^\dagger(\mathbf{x})\right]. \tag{3.6}$$

For classical improvement, the couplings should be [83, 84]: $\beta_{V0} = \frac{5}{3}$, $\beta_{V1} = -\frac{1}{12}$, $\beta_{V2} = 0$, $\beta_{K0} = \frac{5}{6}$ and $\beta_{K1} = \frac{1}{6}$. Perturbative improvements at the quantum level generate corrections of $\mathcal{O}(g^2a^2)$ [185, 187]. One can further nonperturbatively tune these couplings numerically. For quantum simulations, these couplings could be extracted via analytic continuation of Euclidean calculations [50]. The resulting H_I then has leading errors of $\mathcal{O}(a^4)$ to H_{co}.

Both H_{KS} and H_I can be derived from Euclidean actions via the transfer matrix in the continuous-time limit. The Lüscher-Weisz action [184] was used to derive H_I [83, 84] and has improved errors of $\mathcal{O}(a^4)$ compared to the $\mathcal{O}(a^2)$ Wilson action used to derive H_{KS} [188]. For the Lüscher-Weisz action, $a = 0.4$ fm lattices were found to have similar discretization errors to $a = 0.17$ fm lattices with the Wilson action [189]. Similarly, limited direct studies

of H_I and $H_{\rm KS}$ [190] suggest that H_I produces discretization errors comparable to $H_{\rm KS}$ at half the lattice spacing of H_I. As the number of qubits required is $\mathcal{O}((L/a)^d)$, using H_I may require $\gtrsim 2^d$ fewer qubits in realistic quantum simulations for a fixed discretization error compared to $H_{\rm KS}$. While this chapter focuses on pure gauge theories, improved Hamiltonian for fermions exist and the quantum implementation is discussed in [191]

3.1 Derivation for the improved potential term

The classical errors of $V_{\rm KS}$ can be analyzed via the series expansion of the one-plaquette Wilson loop

$$\mathrm{Re\,Tr}\, P_{ij}(x) = \mathrm{Re\,Tr}\, \mathbf{P}\{e^{ig_s \oint_{1\times 1} A\cdot dx}\}, \tag{3.7}$$

where $\mathbf{P}$ stands for the path-ordering. To do this, we transform the line integral of A into the surface integral ds_{ij} with Stokes theorem, and then Taylor expand it around the center of the plaquette $\mathbf{x}_c$ to the next leading order:

$$\begin{aligned}\oint_{1\times 1} dx\cdot A &= \int_{-a/2}^{a/2}\int_{-a/2}^{a/2} ds_{ij} F_{ij}(\mathbf{x}_c+\mathbf{x}') \\ &= a^2 F_{ij}(\mathbf{x}_c) + \frac{a^4}{24}(D_i^2+D_j^2)F_{ij}(\mathbf{x}_c) + O(a^6).\end{aligned} \tag{3.8}$$

We then obtain

$$\mathrm{Re\,Tr}\, P_{ij}(\mathbf{x}) = \mathbb{I} - g_s^2 a^4\, \mathrm{tr}\left[\frac{1}{2}F_{ij}^2(\mathbf{x}_c) + \frac{a^2}{24}F_{ij}(\mathbf{x}_c)(D_i^2+D_j^2)F_{ij}(\mathbf{x}_c) + \mathcal{O}(a^4)\right] + \mathcal{O}(g_s^4). \tag{3.9}$$

The $\mathcal{O}(a^2)$ errors can be canceled by including gauge invariant two-plaquette Wilson loops in the potential:

$$\mathrm{Re\,Tr}\, R_{ij}(\mathbf{x}) = \mathrm{Re\,Tr}\left\{ \begin{array}{l} \\ \\ \mathbf{x}\ i \end{array} \right. \!\!\!\

We implement the quantum circuits for $\hat{H}_I$ term by term with the primitive gates in Tab. 1.2. Optimal quantum circuits depend on the underlying architecture – in particular connectivity. We assume register connectivity between a pair of links sharing a common site (linear register connectivity).

$\hat{V}_I$ includes $\hat{P}_{ij}(\mathbf{x})$ for every individual plaquette and the rectangles $\hat{R}_{ij}(\mathbf{x})$ for every neighboring two plaquettes. We denote the circuits for $\hat{V}_{\mathrm{KS}}$ as $\mathcal{U}_{V_{\mathrm{KS}}} = e^{i\theta \,\mathrm{Re}\,\mathrm{tr}\,\hat{P}_{ij}(\mathbf{x})}$ (Fig. 1.2a) and for the rectangles $\mathcal{U}_{V_{\mathrm{rect}}} = e^{i\theta \,\mathrm{Re}\,\mathrm{tr}\,\hat{R}_{ij}(\mathbf{x})}$ (Fig. 3.2a), with the coupling and trotter step encoded in θ. The circuit of Fig. 3.2a with registers appropriately changed implements $\mathcal{U}_{V_{\mathrm{bent}}}$.

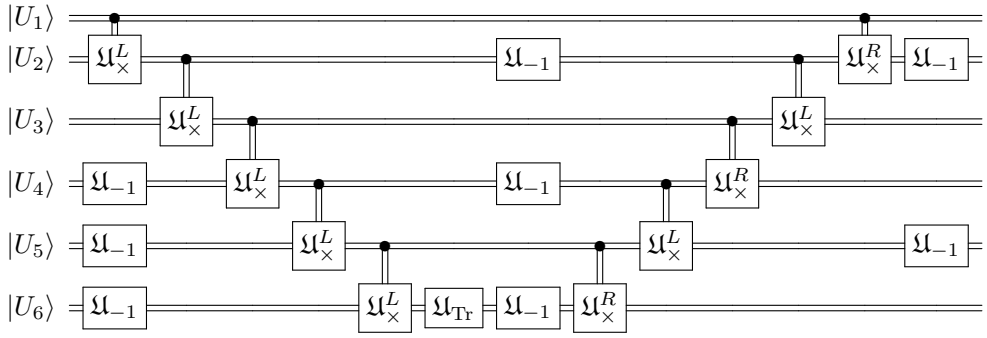

(a) $\mathcal{U}_{V_{\mathrm{rect}}}$ assuming linear register connectivity.

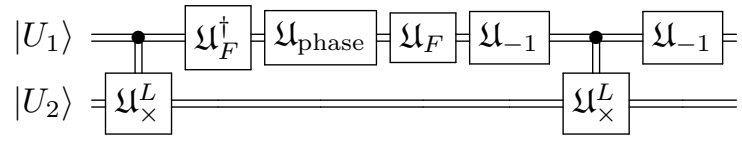

(b) $\mathcal{U}_{K_{2L}}$.

Figure 3.2: Quantum circuits for the time evolution of $\hat{H}_I$.

The circuits $\mathcal{U}_{K_{\mathrm{KS}}} = e^{i\theta \,\mathrm{tr}\,\hat{L}_1^2}$ for $\hat{K}_{\mathrm{KS}}$ can be implemented by the L-phase gate $\mathfrak{U}_{\mathrm{phase}}$ in the electric field basis [82], as shown in Fig. 1.2b. To avoid dealing with $\hat{L}$ and $\hat{U}$ operators

simultaneously, we rewrite $\hat{K}_{2L}$ as

$$\hat{K}_{2L} = \frac{g_t^2}{a} \sum_{x,i} \mathrm{tr}\Big[\hat{R}_i(\mathbf{x})\hat{L}_i(\mathbf{x}+a\mathbf{i})\Big], \tag{3.14}$$

using the right electric field operator [192]:

$$\hat{R}_i(\mathbf{x}) \equiv \hat{U}_i^\dagger(\mathbf{x})\hat{L}_i(\mathbf{x})\hat{U}_i(\mathbf{x}) = \hat{R}_i^b(\mathbf{x})\lambda_b, \tag{3.15}$$

For simplicity, we denote the two succeeding links in one direction as U_1 and U_2 following Fig. 3.1, and thus $\mathrm{tr}\Big[\hat{R}_i(\mathbf{x})\hat{L}_i(\mathbf{x}+a\mathbf{i})\Big]$ becomes $\mathrm{tr}\Big[\hat{R}_1\hat{L}_2\Big]$. For non-Abelian gauge theories, this sum of non-commuting terms ($\hat{R}_1^b\hat{L}_2^b$ with color index b) is difficult to implement. We bypass this obstacle by decomposing $\hat{R}_1\hat{L}_2$ as

$$\mathrm{tr}\Big(\hat{R}_1\hat{L}_2\Big) = \mathrm{tr}\Big[\hat{L}_2^2 + \hat{R}_1^2 - (\hat{L}_2 - \hat{R}_1)^2\Big]/2. \tag{3.16}$$

With $\hat{R}^2 = \hat{L}^2$, the first two terms can be absorbed into $\hat{K}_{\mathrm{KS}}$. Thus, for $\hat{K}_I$ the only new term is $\mathrm{tr}\Big[(\hat{L}_2 - \hat{R}_1)^2\Big]$. Defining the evolution operator $\mathcal{U}_{K_{2L}} \equiv e^{i\theta\,\mathrm{tr}\left(\hat{L}_2-\hat{R}_1\right)^2}$, and using $[\mathcal{U}_{K_{2L}}, \hat{U}_1\hat{U}_2] = 0$, the matrix elements of $\mathcal{U}_{K_{2L}}$ are found to be (see 3.3):

$$\left\langle U_1', U_2'\right| \mathcal{U}_{K_{2L}} \left|U_1, U_2\right\rangle = \delta_{U_1'U_2', U_1U_2} \left\langle U_1'\right| e^{i\theta\,\mathrm{tr}\,\hat{L}_1^2} \left|U_1\right\rangle, \tag{3.17}$$

The circuit in Fig. 3.2b implements Eq. (3.17) by first storing the conserved quantity U_1U_2 in the second register $|U_2\rangle$ via $\mathcal{U}_\times^L$, then performing $e^{i\theta\,\mathrm{tr}\,\hat{L}_1^2}$ on $|U_1\rangle$ with the sequence $\mathcal{U}_F^\dagger\mathcal{U}_{\mathrm{phase}}\mathcal{U}_F$. Finally, we ensure the conserved product of U_1U_2 imposed by $\delta(U_1'U_2' - U_1U_2)$ using the information stored in the second register via $\mathcal{U}_{-1}\mathcal{U}_\times\mathcal{U}_{-1}$.

While using $\hat{H}_I$ should require $\gtrsim 2^d$ times fewer qubits, it requires additional gates to implement evolutions with the improved terms. Since the dominant quantum errors today are from decoherence and the entangling gates with error rates of $\mathcal{O}(10^{-2})$ [193–195], this

increased cost may diminish the gain from using $\hat{H}_I$. We list the gate costs in terms of primitive gates in Tab. 3.1 for one trotter step using either $\hat{H}_{\rm KS}$ or $\hat{H}_I$. Depending on which primitive gates dominate the circuits, the gate cost for $\hat{H}_I$ is 2 to 4 times that of $\hat{H}_{\rm KS}$ per link register. For the group $\mathbb{Z}_N$ and D_N [196], different primitive gates take approximately the same order of entangling native gates. Since $\hat{H}_I$ should require $\gtrsim 2^d$ fewer link registers, for the cases of $d = 2, 3$ we anticipate the same or fewer total primitive gate cost.

Gate	$N[\hat{K}_{\rm KS} + \hat{V}_{\rm KS}]$	$N[\hat{K}_{\rm 2L} + \hat{V}_{\rm rect}]$	$\mathbb{Z}_2$ Impl.
$\mathfrak{U}_F$	2	2	H
$\mathfrak{U}_{\rm phase}$	1	1	$R_z(\theta)$
$\mathfrak{U}_{\rm Tr}$	$\frac{d-1}{2}$	$d-1$	$R_z(\theta)$
$\mathfrak{U}_{-1}$	$3(d-1)$	$2+8(d-1)$	$\mathbb{I}$
$\mathfrak{U}_{\times}$	$6(d-1)$	$4+20(d-1)$	CNOT

Table 3.1: Number of primitive gates per link register per trotter step neglecting boundary effects (columns 2-3), implementation for $\mathbb{Z}_2$ (last column).

3.3 Kinetic Term Circuit Derivation

To derive the quantum circuit for the term $\hat{K}_{2L}$, it is useful to review the properties of left and right electric field operators based on the discussion in [192]. $\hat{L}_i(\mathbf{x}) = \hat{L}_i^a(\mathbf{x})\lambda_a$ is the left electric field operator satisfying the following commutation relations [192, 197][1]:

$$[\hat{L}_i^a(\mathbf{x}), \hat{U}_i(\mathbf{x})] = \lambda_a \hat{U}_i(\mathbf{x}), \tag{3.18}$$

$$[\hat{L}_i^a(\mathbf{x}), \hat{L}_i^b(\mathbf{x})] = -if_{abc}\hat{L}_i^c(\mathbf{x}), \tag{3.19}$$

where $\{\lambda_a\}$ are the group's generators and f_{abc} are the structure constants.

The $\hat{R}_i(\mathbf{x})$ operator defined in Eq. (3.15) corresponds to the right electric field operator

1. Our definition of $\hat{L}$ differs from [197] by a minus sign.

obeying the following commutation relations: [192]

$$[\hat{R}_i^a(\mathbf{x}), \hat{U}_i(\mathbf{x})] = \hat{U}_i(\mathbf{x})\lambda_a, \tag{3.20}$$

$$[\hat{R}_i^a(\mathbf{x}), \hat{R}_i^b(\mathbf{x})] = if_{abc}\hat{R}_i^c(\mathbf{x}), \tag{3.21}$$

$$[\hat{L}_i^a(\mathbf{x}), \hat{R}_i^b(\mathbf{x})] = 0. \tag{3.22}$$

For the following discussions, we will neglect the position dependence on $\mathbf{x}$ and the subscript i of operators for simplicity. $\hat{L}(\hat{R})$ transforms $\hat{U}$ operators as follows [197]:

$$e^{i\alpha_a\hat{L}^a}\hat{U}_{mn}e^{-i\alpha_a\hat{L}^a} = U_{mk}(\alpha)\hat{U}_{kn}, \tag{3.23}$$

$$e^{i\alpha_a\hat{R}^a}\hat{U}_{mn}e^{-i\alpha_a\hat{R}^a} = \hat{U}_{mk}U_{kn}(\alpha), \tag{3.24}$$

with matrix-valued $U(\alpha) = e^{i\alpha^b\lambda_b}$. And $|U\rangle$ transforms under $e^{-i\alpha_a\hat{L}^a}$ and $e^{-i\alpha_a\hat{R}^a}$ as

$$\begin{aligned} e^{-i\alpha_a\hat{L}^a}|U\rangle &= |U(\alpha)\cdot U\rangle\,, \\ e^{-i\alpha_a\hat{R}^a}|U\rangle &= |U\cdot U(\alpha)\rangle\,. \end{aligned} \tag{3.25}$$

With the above properties, we can simplify the implementation of $\mathcal{U}_{K_{2L}} \equiv e^{i\theta\,\mathrm{tr}\left(\hat{L}_2-\hat{R}_1\right)^2}$. First, we shoe that it commutes with $\hat{U}_1\hat{U}_2$, as

$$\begin{aligned} &[(\hat{L}_2^a - \hat{R}_1^a), (\hat{U}_1\hat{U}_2)_{ij}] \\ =&(\hat{U}_1)_{ik}[\hat{L}_2^a, (\hat{U}_2)_{kj}] - [\hat{R}_1^a, (\hat{U}_1)_{ik}](\hat{U}_2)_{kj} \\ =&(\hat{U}_1)_{ik}(\lambda^a)_{kl}(\hat{U}_2)_{lj} - (\hat{U}_1)_{il}(\lambda^a)_{lk}(\hat{U}_2)_{kj} \\ =&\,0. \end{aligned} \tag{3.26}$$

This subsequently leads to $[\mathcal{U}_{K_{2L}}, (\hat{U}_1\hat{U}_2)] = 0$. The time evolution circuit for the two-link

term $\mathcal{U}_{K_{2L}}$ thus preserves the product of U_1U_2 and can be written as:

$$\left\langle U_1', U_2' \right| \mathcal{U}_{K_{2L}} \left| U_1, U_2 \right\rangle = \delta_{U_1'U_2', U_1U_2} \mathcal{A}(U_1, U_2, U_1'). \tag{3.27}$$

We obtain $\mathcal{A}(U_1, U_2, U_1')$ by integrating over U_2' on both sides of Eq. (3.27), canceling $\delta_{U_1'U_2', U_1U_2}$:

$$\mathcal{A}(U_1, U_2, U_1') = \int dU_2' \left\langle U_1', U_2' \right| \mathcal{U}_{K_{2L}} \left| U_1, U_2 \right\rangle. \tag{3.28}$$

Define the change from U_2 to U_2' as $V \equiv U_2' U_2^{-1}$, which is evidently a group element and can be parameterized as $V = e^{i\alpha^b \lambda_b}$. Thereby the operator $e^{i\alpha_a \hat{L}_2^a}$ generates the transformation from $\langle U_2|$ to $\langle VU_2| = \left\langle U_2' \right|$. Thus, the final state can be written as

$$\left\langle U_1', U_2' \right| = \left\langle U_1', VU_2 \right| = \left\langle U_1', U_2 \right| e^{i\alpha_c \hat{L}_2^c}. \tag{3.29}$$

As the Haar measure is invariant under product with any group element, we have

$$dU_2' = d(VU_2) = dV. \tag{3.30}$$

Replacing $\left\langle U_1', U_2 \right|$ and dU_2' in the RHS of Eq. (3.28) with Eq. (3.29) and Eq. (3.30), we get:

$$\mathcal{A}(U_1, U_2, U_1') = \int dV \left\langle U_1', U_2 \right| e^{i\alpha_c \hat{L}_2^c} \mathcal{U}_{K_{2L}} \left| U_1, U_2 \right\rangle. \tag{3.31}$$

The integral over all group transformations $\int dV e^{i\alpha_c \hat{L}_2^c}$ is equivalent to projecting the $|U_2\rangle$ register to the ground state of $\hat{L}_2^2$ ($|J_2 = 0\rangle$) up to a normalization factor fixed to be consistent with $\int dV = |G|$ [198]. This can be easily understood as follows. Any generator $\hat{L}^b$ annihilates the state $\int dV e^{i\alpha_a \hat{L}^a} |U\rangle$ for arbitrary $|U\rangle$, as a result of Stokes' theorem on a

compact manifold:

$$\hat{L}^b \int dV e^{i\alpha_a \hat{L}^a} |U\rangle = -i \int dV \frac{\partial}{\partial \alpha_b} e^{i\alpha_a \hat{L}^a} |U\rangle = 0. \tag{3.32}$$

Therefore, $\int dV e^{i\alpha_a \hat{L}_2^a} |U\rangle \propto |J_2 = 0\rangle$ and we get the following:

$$\int dV e^{i\alpha_a \hat{L}_2^a} = |G| \, |J_2 = 0\rangle \langle J_2 = 0| = |G| \hat{P}_{J_2=0}. \tag{3.33}$$

Substitute Eq. (3.33) into Eq. (3.31) and notice that, as $\mathcal{U}_{K_{2L}}$ commutes with $\hat{R}_2^2$, it conserves the quantum number J_2, and therefore, $\hat{P}_{J_2=0} \, \mathcal{U}_{K_{2L}} = \hat{P}_{J_2=0} \, \mathcal{U}_{K_{2L}} \, \hat{P}_{J_2=0}$. Insert another $\hat{P}_{J_2=0}$ after $\mathcal{U}_{K_{2L}}$ in Eq. (3.31) and we find $\mathcal{A}$ is:

$$\begin{aligned} \mathcal{A}(U_1, U_2, U_1') &= \langle U_1', J_2 = 0 | \, \mathcal{U}_{K_{2L}} \, |U_1, J_2 = 0\rangle \\ &= \langle U_1' | \, e^{i\theta \operatorname{tr} \hat{R}_1^2} \, |U_1\rangle \,, \end{aligned} \tag{3.34}$$

which gives

$$\langle U_1', U_2' | \, \mathcal{U}_{K_{2L}} \, |U_1, U_2\rangle = \delta_{U_1' U_2', U_1 U_2} \langle U_1' | \, e^{i\theta \operatorname{tr} \hat{L}_1^2} \, |U_1\rangle \,. \tag{3.35}$$

3.4 Demonstration a real quantum computer

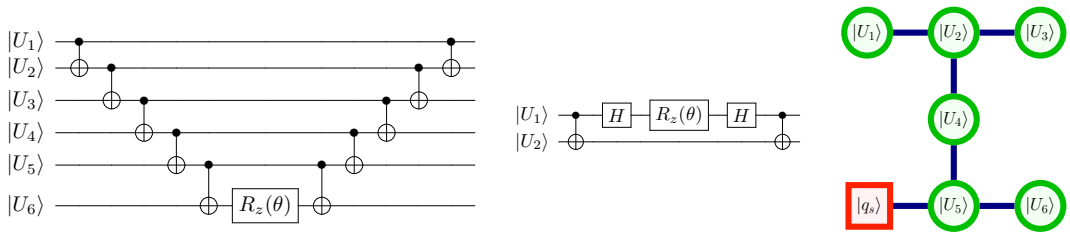

(a) (b) (c)

Figure 3.3: $\mathcal{U}_{V_{\text{rect}}}$ (a) and $\mathcal{U}_{K_{2L}}$ (b) for $\mathbb{Z}_2$ gauge theory. (c) Link-to-qubit map on `ibm_perth`.

For $\mathbb{Z}_2$ gauge theory, $\hat{H}_I$ can be mapped to Pauli matrices. Choosing the magnetic field

basis, the qubit state $|0\rangle$ ($|1\rangle$) represents the element 1 (-1) of $\mathbb{Z}_2$. Implementations of the primitive gates are listed in the last column of Tab. 3.1. We consider the most expensive $\mathbb{Z}_2$ gate, $\mathcal{U}_{V_{\text{rect}}}$ on the 7-qubit `ibm_perth` device (Fig. 3.3c). The connectivity of `ibm_perth` prevents implementing $\mathcal{U}_{V_{\text{rect}}}$ as shown in Fig. 3.3a. With the mapping from links to qubits shown in Fig. 3.3c, a transpiled version of the circuit with 12 CNOTs and 20 additional one-qubit gates are used. We use the benchmark value $\theta = \delta t/(g_s g_t) = 0.811411$, precluding circuit optimization when using θ values such as $\pi/2$.

To quantify quantum errors, we evolve states with $\mathcal{U}_{V_{\text{rect}}}$ and its inverse, and compare the measurement with noiseless expectations, implemented as the circuit $\mathcal{U}_{\text{circ}}^{|n\rangle}$ in Fig. 3.4. Without noise, the state preparation $\hat{\Psi}_n$ and $\mathcal{U}_{V_{\text{rect}}}$ are exactly cancelled by their complex conjugations, thus all measurements return $|0\rangle^{\otimes 6}$, and the distribution $P(w_H)$ of the Hamming weight w_H – the number of qubits measured in the $|1\rangle$ state – returns $P(w_H) = \delta_{w_H,0}$. In the noise-dominated limit where all states are equally populated, $P(w_H)$ follows the binomial distribution with 6 trials. We take $\mathcal{F}_{\text{rect}}^{|n\rangle} \equiv \sqrt{P(w_H = 0)}$ as a definition of the quantum

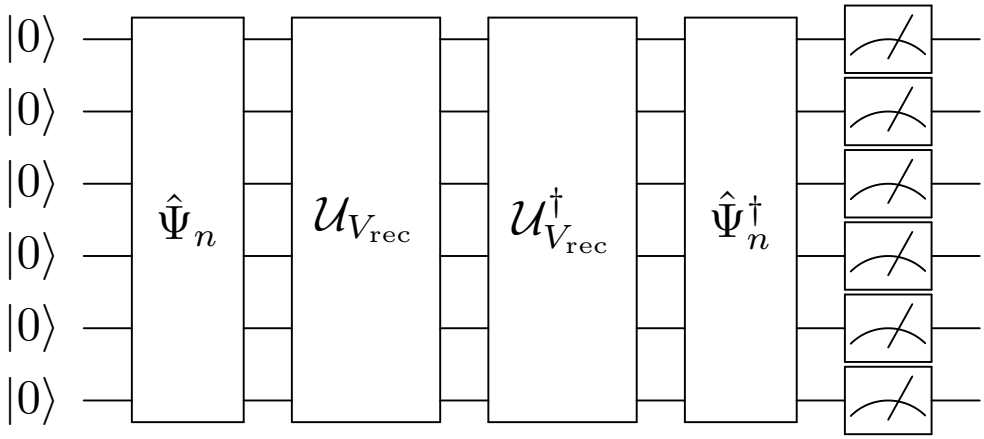

Figure 3.4: $\mathcal{U}_{\text{circ}}^{|n\rangle}$ for studying the errors of $\mathcal{U}_{V_{\text{rect}}}$.

fidelity of $\mathcal{U}_{V_{\text{rect}}}$ for the state $|\Psi_n\rangle = \hat{\Psi}_n |0\rangle^{\otimes 6}$. Determining the fidelity requires testing all

the possible states $|\Psi_n\rangle$, a prohibitively expensive task [199]. Therefore we consider a restricted set consisting of $\hat{\Psi}_n = \prod_{m\leq n} H_m^{\otimes}$ for $n \in [0, 6]$ with m indicating the qubit to which H is applied.

To mitigate the coherent noise dominating the CNOT errors, we implement Pauli twirling [200–204] which converts coherent errors into random errors in Pauli channels and has found success in low-dimensional lattice field theories [205]. The circuits are modified by wrapping each CNOT with a set of Pauli gates $\{\mathbb{I}, X, Y, Z\}$ randomly sampled from sets satisfying

$$\left(\prod_i (\sigma_i^{b_i})^{\otimes}\right) \text{CNOT} \otimes \mathbb{I}_4 \left(\prod_i (\sigma_i^{a_i})^{\otimes}\right) = \text{CNOT} \otimes \mathbb{I}_4, \tag{3.36}$$

where the i-th qubit (including spectators) was rotated by $\sigma_i^{a_i}$ before the CNOT and by $\sigma_i^{b_i}$ after. Despite the enormous number of possible circuits, prior work has found $\mathcal{O}(10)$ circuits to be sufficient for error mitigation [200]. Therefore we implemented 15 unique circuits and run each circuit 2^{13} times. We also compute $\mathcal{F}_{\text{rect}}^{|6\rangle}$ without Pauli twirling to gauge its effect.

With the above setup, we obtain the distribution $P(w_H)$ in Fig. 3.5 for selected $|\Psi_n\rangle$ and the state-dependent fidelities $\mathcal{F}_{\text{rect}}^{|n\rangle}$ (Table 3.2), yielding an average $\mathcal{F}_{\text{rect}} = 0.550$. Without Pauli twirling for $n = 6$, $P(w_H)$ is indistinguishable from the noise-dominated limit while all the Pauli-twirled results are skewed toward the noiseless result, with states of lower n (and consequently less average entanglement) being closer to the desired value. Comparing the results for $|\Psi_6\rangle$ with and without Pauli twirling we observe a fourfold improvement in fidelity – clearly demonstrating the advantage from this error mitigation.

$\|\Psi_n\rangle$	$\|\Psi_0\rangle$	$\|\Psi_1\rangle$	$\|\Psi_2\rangle$	$\|\Psi_3\rangle$	$\|\Psi_4\rangle$	$\|\Psi_5\rangle$	$\|\Psi_6\rangle$	$\|\Psi_6\rangle_{\text{no PT}}$
$\mathcal{F}_{\text{rect}}^{\|n\rangle}$	0.650	0.575	0.605	0.599	0.579	0.442	0.425	0.1194

Table 3.2: Measured state-dependent quantum fidelities with Pauli twirling and without it for $|\Psi_6\rangle_{\text{no PT}}$.

For a single trotter step, the time evolution of $\hat{H}_I$ for a two-plaquette lattice with open

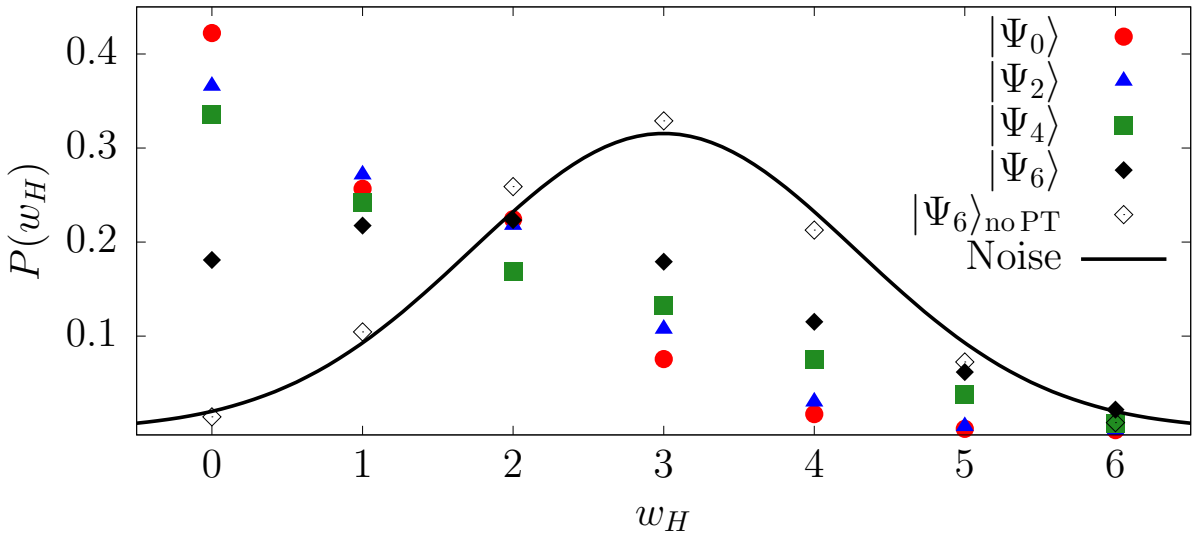

Figure 3.5: Probability of measuring Hamming weights for selected $|\Psi_n\rangle$ compared to the noise-dominated results. In the noiseless limit, $P(w_H) = \delta_{w_H,0}$ for all $|\Psi_n\rangle$.

boundary conditions requires at least 28 CNOTs (40 one-qubit gates): 12 CNOTs (20 one-qubit gates) for $\mathcal{U}_{V_{\text{rect}}}$, at least 12 CNOTs (2 one-qubit gates) for the two $\mathcal{U}_{V_{\text{KS}}}$ and 4 CNOTs (6 one-qubit gates) for the two $\mathcal{U}_{K_{2L}}$, alongwith 12 one-qubit gates for $\mathcal{U}_{K_{\text{KS}}}$. Assuming that the average fidelity depends on the total number of CNOT gates, we can estimate the single-trotter-step fidelity for $\hat{H}_I$: $\mathcal{F}_\delta \lesssim (\mathcal{F}_{\text{rect}})^{28/12} \approx 0.25$. Thus current devices are inadequate for real-time computations. However given the expected hardware improvements in the coming years [46, 48, 206], $\mathcal{F}_\delta$ will be improved, allowing simulations of a two-plaquette lattice for $\mathbb{Z}_2$ gauge theory and direct comparisons between Hamiltonians. Alternatively, classical simulators could explore lattices up to 7^2 [207] to test improved Hamiltonians.

3.5 Conclusions

In this chapter, we designed the quantum circuits for simulating the improved Hamiltonian $\hat{H}_I$. These circuits introduce counter-terms, which are the two-plaquette magnetic energy and the two-link electric energy terms with matching coefficients, to cancel the leading-order discretization errors of the commonly used $\hat{H}_{\text{KS}}$. Based on previous empirical evidence with

Euclidean LGTs, such improvements should allow quantum simulations with a factor of $\gtrsim 2^d$ fewer qubits. With this reduction, we expect the gate count to be comparable or less than that of $\hat{H}_{\mathrm{KS}}$ for theories with $d \geq 2$ despite increases of gate costs per link.

For near-term numerical demonstrations, we constructed the circuits for $\hat{H}_I$ of the $\mathbb{Z}_2$ gauge theory and found that for `ibm_perth` the fidelity of the 12 CNOT improved potential term is $\lesssim 0.550$. Our results suggest that alongside hardware developments, improved Hamiltonians can accelerate quantum simulations by years by reducing the number of qubits required, with optimistic prospects for $2+1d$ $\mathbb{Z}_2$ simulations in the near future.

CHAPTER 4

GAUGE SYMMETRY AS QUANTUM ERROR CORRECTION CODES

In order to use quantum computers for simulations, the infinite-dimensional Hilbert space of the gauge theory must be addressed. To allow a mapping to a finite quantum memory, many digitization proposals to truncate this space have been studied (see Sec VI.b of [22]). All truncations break the continuous symmetries to some degree and produce theories with smaller symmetries. Understanding the theoretical errors introduced by this is an area of active research [54–61]. Broadly speaking, methods to encode these regularized theories in quantum computers fall into two classes. The first class digitizes all the states connected through gauge transformations as *redundancy* and uses Gauss's law to project the gauge-invariant subspace, where the physical theory should be simulated. This can be done in group element basis [56, 74, 154, 197, 208–213], the group representation basis [192, 197, 214–218], the mixed basis [219], as a fuzzy gauge theory [220, 221], as a quantum link model [222–226], and more. The second class digitizes only gauge-invariant states. We refer to this as *fixing the gauge* in the sense that it eliminates the redundant degrees of freedom. One can digitize the independent Wilson loops in the lattice, which can be identified as the plaquettes in $(2+1)$ dimensions [227–235], and as the states outside the maximal tree in higher dimensions [58]. Other digitizations to eliminate redundancy include the Fock basis in the light-front Hamiltonian [7, 236], the local multiplet basis [31, 237], and spin networks [238, 239]. Besides reducing the qubit cost, gauge fixing also simplifies the quantum state preparation, but can complicate the Hamiltonian [31, 58, 227, 237–245]. At present, it is an open question whether gauge fixing is ultimately advantageous for quantum simulation.

The effect of noisy hardware has been generally neglected in the above discussion. Naively, gauge-redundant digitizations suffer more severely from quantum noise because more qubits introduce more errors. However, not all the errors are equally harmful. Noise which breaks

symmetries can change the universality class simulated [216, 217, 220, 246–248] and thus sufficient symmetry preservation is crucial [111, 113, 243, 249–251]. In the gauge-redundant digitization, quantum errors can be classified as gauge-preserving or gauge-violating operators [119, 251–255]. The gauge-violating errors can be mitigated by introducing energy penalties [110, 114, 115, 118, 121, 256] or random gauge transformations [113] in the Hamiltonian evolution. They can also be corrected by measuring and restoring Gauss's law [111, 257]. The gauge-fixed digitization – while precluded from noise-based gauge violations– does not have such natural error mitigation or correction methods, and thus relies on generic methods for the residual errors. Notably, redundancy and symmetry play a central role in both quantum error correction (QEC) and mitigation (QEM). QEC deliberately designs a redundant full Hilbert space $\mathcal{H}_{\text{full}}$ on the physical qudits and encodes quantum information in a much smaller code subspace $\mathcal{H}_{\text{code}}$ on logical qudits with certain symmetries, thus allowing for correction without disrupting the coherent quantum information in $\mathcal{H}_{\text{code}}$ [44, 45]. As an active field of research, estimates for the overhead – the physical to logical qubit ratio – vary from $\mathcal{O}(10)$ to $\mathcal{O}(10^5)$ [46–48]. QEM uses the existing symmetries without introducing redundancy to mitigate errors [49]. Indeed, it is this structural similarity between QEC, QEM and LGT that inspires the above mentioned works [110, 111, 113, 114, 249–255, 257] to use gauge redundancy as a resource for error correction and mitigation. Given the huge variance of the overhead in QEC, and that gauge fixing saves logical qubits only by a factor of approximately $(1 - 1/d)$ in d spatial dimensions, keeping the gauge redundancy for QEC or QEM may be more resource efficient for achieving a desired accuracy. This idea has only just begun to be explored for field theories [255, 258–260] including fermionic systems [261, 262].

The answer to *when* this is true can be phrased as a *threshold theorem* of QEC [263–265], which states that there is a threshold for the error rate of physical qubits, below which more redundancy makes the code more error-proof. In this chapter, we compute the threshold

below which gauge redundancy makes the digitization more robust. After reviewing the connection between gauge symmetry and QEC in Sec. 4.1 and Sec. 4.2, we present the circuits to encode and decode via Gauss's law. This paves the way for calculations in Sec. 4.4 of the thresholds, below which the gauge-redundant digitization combined with QEC has a better fidelity than the gauge-fixed one.

4.1 Gauge symmetry and fixing

We will briefly review gauge symmetry on lattice in both the group element (magnetic) and the group representation (electric) basis, as the former is closer to the path-integral quantization and the latter to Gauss's law in classical fields. These bases are related by the group Fourier transform. In the group element basis, one assigns an element of the group G (link variable) to each link on the lattice, representing the Wilson line [68]. For continuous gauge groups, the link variables are related to the vector potentials of the continuum theory via:

$$U_{\mathbf{x},i} = P \exp\left(-i \int_{\mathbf{x}}^{\mathbf{x}+\mathbf{i}} d\mathbf{l} \cdot \mathbf{A}\right) \approx e^{-iaA_i(\mathbf{x})}, \tag{4.1}$$

where P denotes path ordering, a is the lattice spacing, and i the spacial direction of the link. The gauge-redundant Hilbert space $\mathcal{H}_{\text{gauge}}$ is the tensor product of N_L local spaces, each spanned by the group elements:

$$\mathcal{H}_{\text{gauge}} = \text{span}(\{|U\rangle, U \in G\})^{\otimes N_L} \tag{4.2}$$

where N_L is the total number of links and $\langle U|U'\rangle = \delta_{U',U}$.

For a continuous gauge group, $\dim(\mathcal{H}_{\text{gauge}}) = \infty$, and digitization is required to render it finite. Here we will focus on the discrete subgroup digitization. Some discussion of the continuous theory can be found in [266] and other digitization schemes remain for future works. For a discrete gauge group G, the dimension of the one-link Hilbert space is $|G|$. The

dimension of $\mathcal{H}_{\text{gauge}}$ is given by:

$$\dim \mathcal{H}_{\text{gauge}} = |G|^{N_L}. \tag{4.3}$$

A gauge transformation $\hat{T}_{g_{\mathbf{x}}}$ is a unitary operator that transforms all out-going (incoming) links connected to a site $\mathbf{x}$ by a left (right) product with $g \in G$ ($g^{-1} \in G$):

$$\hat{T}_{g_{\mathbf{x}}} = \prod_{i=1}^{d} [\hat{L}_g(\mathbf{x}, i)\hat{R}_{g^{-1}}(\mathbf{x} - \mathbf{i}, i)], \tag{4.4}$$

where $\hat{L}_g, \hat{R}_g$ are left and right multiplication operators,

$$\hat{L}_g = \sum_{U \in G} |gU\rangle \langle U| \,,\ \hat{R}_{g^{-1}} = \sum_{U \in G} \left|Ug^{-1}\right\rangle \langle U| \,. \tag{4.5}$$

Typical lattice gauge Hamiltonians preserves gauge symmetry as they commutes with the gauge transformation operator $\hat{T}_{g_{\mathbf{x}}}$. This includes the Kogut-Susskind [68], the Symanzik-improved [83, 84, 267, 268] and the Similarity-Renormalization-Group-improved ones [59].

Gauge-invariant states satisfy a lattice version of Gauss's law:

$$\hat{T}_{g_{\mathbf{x}}} |\Psi_{\text{inv}}\rangle = |\Psi_{\text{inv}}\rangle \,, \forall\, g_{\mathbf{x}} \in G. \tag{4.6}$$

In the $|U\rangle$ basis, Gauss's law requires the wave functions on gauge-equivalent configurations to be the same, as taking an inner product of Eq. (4.6) with $\langle U|$ gives

$$\left\langle U|\hat{T}_{g_{\mathbf{x}}}|\Psi_{\text{inv}}\right\rangle = \langle U|\Psi_{\text{inv}}\rangle \tag{4.7}$$

Such states are in the gauge-invariant subspace $\mathcal{H}_{\text{inv}}$, which can be projected from $\mathcal{H}_{\text{gauge}}$

with the operator $\hat{P}_{\text{inv}} \equiv \prod_{\mathbf{x}} \hat{P}_0(\mathbf{x})$, where the local Gauss's law projector is

$$\hat{P}_0(\mathbf{x}) = \frac{1}{|G|} \sum_{g_{\mathbf{x}} \in G} \hat{T}_{g_{\mathbf{x}}}. \tag{4.8}$$

To get a clearer physical picture, it is useful to introduce the electric basis $|\sigma_{mn}\rangle$, which is the group Fourier transform of the group element basis:

$$\langle \sigma_{mn} | U \rangle = \sqrt{d_\sigma / |G|} \Gamma^{(\sigma)}_{mn}(U), \tag{4.9}$$

where $\Gamma^{(\sigma)}_{mn}(U)$ is the m, n matrix element of the unitary irreducible representation (irrep) σ for U, d_σ is the dimension of σ. The dimension of the one-link Hilbert space $|G|$ also equals $\sum_\sigma d_\sigma^2$. For the Abelian groups, all irreps are 1d and m, n can therefore be suppressed with σ being the Abelian electric flux. For non-Abelian groups, $|\sigma_{mn}\rangle$ is a tensor representation comprised of the left vector representation $|\sigma_m\rangle$ and the right vector representation $|\bar{\sigma}_n\rangle$:

$$|\sigma_{mn}\rangle = |\sigma_m\rangle \otimes |\bar{\sigma}_n\rangle \,, \tag{4.10}$$

where $\bar{\sigma}$ is the complex conjugate dual of representation σ, i.e. $\Gamma^{(\bar{\sigma})}_{nq}(g) = \Gamma^{(\sigma)}_{qn}(g^{-1})$. This is because gauge transformations act on the links going out from the vertex via

$$\hat{L}_g = \sum_{\sigma,m,q} \Gamma^{(\sigma)}_{mq}(g) \, |\sigma_m\rangle \left\langle \sigma_q \right| \otimes \sum_n |\bar{\sigma}_n\rangle \langle \bar{\sigma}_n| \,, \tag{4.11}$$

thus transforming only the left vector. Similarly, the in-coming links transform in the dual representation, and only the right vectors are transformed:

$$\hat{R}_{g^{-1}} = \sum_{\sigma,m} |\sigma_m\rangle \langle \sigma_m| \otimes \sum_{n,q} \Gamma^{(\bar{\sigma})}_{nq}(g) \, |\bar{\sigma}_n\rangle \left\langle \bar{\sigma}_q \right| . \tag{4.12}$$

Thus, one can define the local charge at vertex $\mathbf{x}$ as the tensor product representation:

$$|Q(\mathbf{x})\rangle = \prod_{i=1}^{d} \otimes |\sigma_m(\mathbf{x}, i)\rangle \otimes |\bar{\sigma}_n(\mathbf{x} - \mathbf{i}, i)\rangle \tag{4.13}$$

$\hat{P}_0(\mathbf{x})$ projects the tensor product to the trivial representation according to the Clebsch-Gordan coefficients of the group. Physically, one can interpret $Q(\mathbf{x})$ as the net flux, and $\hat{P}_0(\mathbf{x})$ selects states with neutral net flux. As the result of the constraints, one lacks the freedom to independently assign all the links variables. Naively, applying $\hat{P}_0(\mathbf{x})$ to all the N_V vertices in the lattice implies N_V different constraints. However, the global charge, defined as the tensor product of all the local charges,

$$\left|Q_{\mathrm{gl}}\right\rangle = \prod_{\mathbf{x}} \otimes |Q(\mathbf{x})\rangle = \prod_{\mathbf{x},i} \otimes |\sigma_m(\mathbf{x}, i)\rangle \otimes |\bar{\sigma}_n(\mathbf{x}, i)\rangle \tag{4.14}$$

is not a gauge constraint but rather the physically-conserved charge of the state under the global transformation with $h \in G$:

$$\hat{T}_h^{\mathrm{Gl}} \prod_{\mathbf{x},i} \left|U_{\mathbf{x},i}\right\rangle = \prod_{\mathbf{x},i} \left|hU_{\mathbf{x},i}h^{-1}\right\rangle . \tag{4.15}$$

In the case of an Abelian group like $U(1)$ or $\mathbb{Z}_N$, the links cannot carry charge as the charges of the left and right vector always cancel, making the global charge automatically neutral. This can also be easily seen in the group element basis as all states are invariant under Eq. (4.15). In contrast, non-Abelian gauge fields can carry charge, as indicated by the difference between the left and right vectors, and the non-trivial global transformations. If one allows for all the possible global charges, the number of independent constraints is thus $N_V - 1$. This makes $N_L - N_V + 1$ links dynamical with the rest $N_V - 1$ links dependent on the dynamical ones. Thus,

$$\dim\mathcal{H}_{\mathrm{inv}} = |G|^{N_L - N_V + 1}. \tag{4.16}$$

If one fixes the global transformations as well, thereby selecting the subspace with neutral global charge, the dimension of $\mathcal{H}_{\text{inv}}$ might be reduced by a factor greater or equal to $|H|/|G|$ where H is the Abelian center of the group, as derived in Appendix 4.1.1.

Choosing which degrees of freedom are independent and eliminating others is equivalent to gauge fixing. On the lattice, the maximal tree method fixes the gauge up to the global transformations Eq. (4.15), by explicitly solving the local Gauss's law constraints which forces some links to be functions of the remaining ones (See [269] for a good discussion). For example, consider the links connected to the vertex $\mathbf{x}$ shown in the left of Fig. 4.1, the state are given by [1]

$$\left|\Psi_{\text{gauge}}\right\rangle = \sum_{\sigma,\rho,\tau} a(\sigma,\rho,\tau)\left|\sigma,\rho,\tau\right\rangle . \tag{4.17}$$

Constraining $|Q(\mathbf{x})\rangle$ to be in the trivial representation, the variable ρ in the maximal tree can be determined as $\rho = \sigma \otimes \bar{\tau}$, which produces the gauge-invariant state:

$$\left|\Psi_{\text{inv}}\right\rangle \;\; = \;\; \sum_{\sigma,\tau} a(\sigma,\tau)\left|\sigma,\tau\right\rangle \otimes \left|\rho = \sigma \otimes \bar{\tau}\right\rangle . \tag{4.18}$$

The same procedure can be repeated till the dependent links form a maximal tree in the lattice, i.e. a set of links which contains one and only one path between any pair of vertices, the size of which is $N_T = N_V - 1$. We will define the Hilbert space spanned by the variables completely determined by Gauss law (in the maximal tree in the above example) as $\mathcal{H}_{\text{red}}$, and the rest as $\mathcal{H}_{\text{fixed}}$. Clearly,

$$\mathcal{H}_{\text{inv}} \cong \mathcal{H}_{\text{fixed}} = \text{span}(\{\left|U\right\rangle, U \in G\})^{\otimes N_L - N_V + 1}. \tag{4.19}$$

Similar to choice of gauge fixing in the continuum, for a given lattice there is no unique maximal tree. One popular method [58, 270–272] is to pick a site $\mathbf{x}_0$, and the set of links

1. We have suppressed the vector indices of representations here for simplicity.

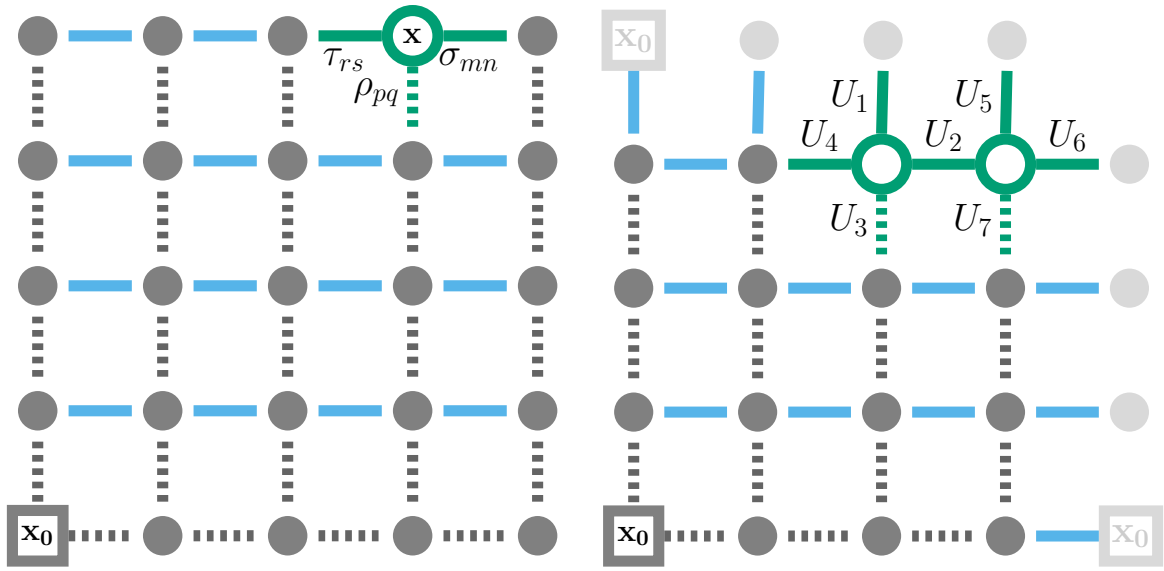

Figure 4.1: Maximal trees (dashed lattice links) of lattices with (left) OBC and (right) PBC. The site at the lower left corner is chosen as the root of the maximal tree.

which uniquely connects $\mathbf{x}_0$ via a comb-like path to any other site form a tree of size $N_T = N_V - 1$. This maximal tree is shown in Fig. 4.1 for 2d with open (OBC) and periodic (PBC) boundary conditions. Notably, the charge at $\mathbf{x}_0$ is not fixed by the maximal tree, but left to carry the charge under global transformations in Eq. (4.15) [58, 272].

In the *gauge-redundant* quantum simulations digitized with Hilbert space $\mathcal{H}_{\text{gauge}}$ and a quantum computer made of qudits of dimension N, the number of qudits required is $\log_N(\dim \mathcal{H}_{\text{gauge}}) = N_L \log_N |G|$. *Gauge fixing* eliminates the redundancy by digitizing the subspace $\mathcal{H}_{\text{inv}}$ instead, thus reducing the number of qudits to $\log_N(\dim \mathcal{H}_{\text{inv}})$. For the rest of the work, we take $\log_N(\dim \mathcal{H}_{\text{inv}}) \approx (N_L - N_T) \log_N |G|$, which is accurate for fixing the maximal tree in both the Abelian and non-Abelian cases, and an upper bound for non-Abelian G if the global symmetry is also fixed. The numbers of sites, links, links in a maximal tree are listed in Tab. 4.1 for different boundary conditions.

Gauge fixing reduces the number of qubits, but often at the price of complicating the lattice gauge Hamiltonian $\hat{H}_{\text{LGT}}$. Written with the gauge-redundant degrees of freedom, $\hat{H}_{\text{LGT}}$ only consists of local electric and magnetic energy operators. In the gauge-fixed

Table 4.1: The number of degrees of freedom in a lattice with L links per side in d dimensions. $b = 0, 1$ for PBC and OBC respectively.

Sites N_V	$(L+b)^d$
Links N_L	$dL(L+b)^{d-1}$
Maximal Tree Links N_T	$(L+b)^d - 1$

formalism with Hamiltonian $\hat{H}_{\text{fixed}}$, the electric operators of the redundant links in the maximal tree cannot be discarded, but are non-local combinations of operators outside the tree [58, 272]. Thus $\hat{H}_{\text{fixed}}$ is generically denser and non-local. It is easier to fix the gauge while keeping the Hamiltonian simple in 1d or 2d. In 2d, $\log_{|G|} \dim \mathcal{H}_{\text{inv}}$ is

$$N_L - N_T = N_L - N_V + 1 = N_P - \chi + 1, \tag{4.20}$$

where N_P is the number of plaquettes, and χ is the Euler characteristic. This also follows from counting the number of plaquettes with independent magnetic fluxes (Wilson loops), plus the topological degrees of freedom. For an OBC lattice ($\chi = 1$), all N_P plaquettes are independent and there are no topological degrees of freedom. This plaquette magnetic flux basis keeps the Hamiltonian local and sparse for Abelian gauge groups [219, 227–234]. For a PBC lattice ($\chi = 0$), the total magnetic flux is zero, thus there are $(N_P - 1)$ plaquettes with independent magnetic fluxes. Additionally, considering the two independent Wilson loops with winding number one, this yields $\dim \mathcal{H}_{\text{inv}} = |G|^{N_P+1}$.

4.1.1 Counting gauge orbits

Let $\mathcal{U}$ be the set of configurations and $\mathcal{G}$ the group of gauge transformations on the entire lattice, with $|\mathcal{U}| = |G|^{N_L}$ and $|\mathcal{G}| = |G|^{N_V}$. In the magnetic basis, $\hat{P}_{\text{inv}} |U\rangle$ is the uniform superposition of all gauge transformations of $|U\rangle$. Thus the number of states in the basis $\hat{P}_{\text{inv}}\mathcal{U}$

is the number of configurations in $\mathcal{U}$ that are not equivalent under gauge transformations:

$$\dim\mathcal{H}_{\text{inv}} = |\mathcal{U}/\mathcal{G}| \tag{4.21}$$

where $|\mathcal{U}/\mathcal{G}|$ is the number of orbits in $\mathcal{U}$ under $\mathcal{G}$. According to Burnside's counting theorem,

$$|\mathcal{U}/\mathcal{G}| = \frac{1}{|\mathcal{G}|}\sum_{T\in\mathcal{G}}|\mathcal{U}^T| = \frac{1}{|\mathcal{G}|}\sum_{|U\rangle\in\mathcal{U}}|\mathcal{G}_{|U\rangle}|, \tag{4.22}$$

where $\mathcal{U}^T$ is the subset of elements invariant under $T\in\mathcal{G}$,

$$\mathcal{U}^T = \{|U\rangle\in\mathcal{U} : T\,|U\rangle = |U\rangle\}, \tag{4.23}$$

and $\mathcal{G}_{|U\rangle}$ is the stabilizer group for the element $|U\rangle$,

$$\mathcal{G}_{|U\rangle} = \{T\in\mathcal{G} : T\,|U\rangle = |U\rangle\}. \tag{4.24}$$

If $T = \prod_{\mathbf{x}}\hat{T}_{h_{\mathbf{x}}}$ then with $|U\rangle = \prod_{\mathbf{x},i}\left|g_{\mathbf{x},i}\right\rangle$, there must be

$$h_{\mathbf{x}+\mathbf{i}} = g_{\mathbf{x},i}^{-1}h_{\mathbf{x}}g_{\mathbf{x},i}, \tag{4.25}$$

which means once $h_{\mathbf{x}_0}$ at a certain site $\mathbf{x}_0$ is fixed, there is at most one $T\in\mathcal{G}$ to keep $|U\rangle$ invariant. For $h_{\mathbf{x}_0}\in H$ the Abelian center of G, this is the global transformation with $h_{\mathbf{x}_0}$. Therefore $|H|\le|\mathcal{G}_{|U\rangle}|\le|G|$ and

$$|\mathcal{U}||H| \le \sum_{|U\rangle\in\mathcal{U}}|\mathcal{G}_{|U\rangle}| \le |\mathcal{U}||G|. \tag{4.26}$$

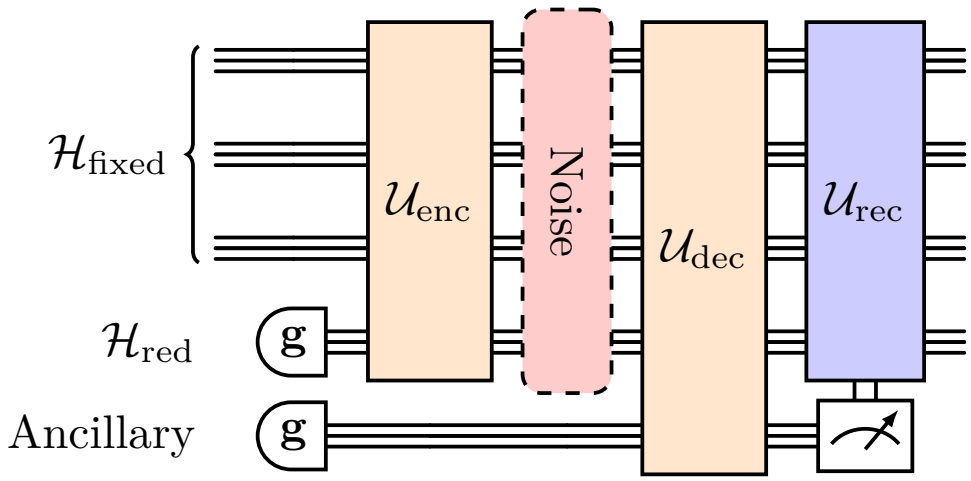

Figure 4.2: Schematic circuit of LGT as QEC. **g** represents a color-neutral state.

given that $|\mathcal{U}| = |G|^{N_L}, |\mathcal{G}| = |G|^{N_V}$, we find

$$|H||G|^{N_L-N_V} \leq |\mathcal{U}/\mathcal{G}| \leq |G|^{N_L-N_V+1}. \tag{4.27}$$

For Abelian groups, $H = G$ and $|\mathcal{U}/\mathcal{G}| = |G|^{N_L-N_V+1} = |G|^{N_L-N_T}$. For non-Abelian G, the "$\leq$" are both "$<$".

4.2 Lattice gauge symmetries as stabilizer codes

In this section, we construct quantum circuits to use gauge redundancy as partial error correction codes for generic finite groups. The method is based on the similarity between stabilizer codes and lattice gauge theories, which we review in 4.2.1. Without redundancy, any error in $\mathcal{H}_{\text{fixed}}$ causes irrecoverable information loss. In the gauge-redundant formalism, as a result of gauge symmetry Eq. (4.7), all the states equivalent under gauge transformation carry copies of the same wave function. This allows one to detect and correct some gauge-symmetry violating errors, as is analyzed in 4.2.2. Fig. 4.2 outlines the circuit to realize such error corrections. The preparation of gauge invariant states is a process to encode

the quantum information with the maximal-tree redundancy. To decode, we introduce an ancillary register at each site to compute and measure the net flux. Nonzero fluxes indicates occurrence of quantum errors which can be mitigated via post-selection, with the associated sampling overhead exhibiting exponential growth in the system size [273]. One can also correct these errors by applying the optimal recoveries after deducing the most likely errors. The details of the construction are in 4.2.4.

4.2.1 Stabilizer codes

Stabilizer codes perform error correction by using a redundant *full Hilbert space* $\mathcal{H}_{\text{full}}$ of physical qubits (qudits), but encoding quantum information only in states with certain symmetries. The symmetry group that defines the code states is called the stabilizer group $\mathcal{S}$, usually a subgroup of the (generalized) Pauli group on the physical qubits (qudits). A code state satisfies

$$\hat{s}\,|\psi\rangle_{\text{code}} = |\psi\rangle_{\text{code}}\,, \forall\, \hat{s} \in \mathcal{S}. \tag{4.28}$$

All code states are in the *code space*, $\mathcal{H}_{\text{code}}$. The sum of all $\hat{s}$ is proportional to the projector from $\mathcal{H}_{\text{full}}$ to $\mathcal{H}_{\text{code}}$:

$$\hat{P}_{\text{code}} = \frac{1}{|\mathcal{S}|} \sum_{\hat{s}\in\mathcal{S}} \hat{s}. \tag{4.29}$$

Note that Eq. (4.28) is similar to Eq. (4.6), and Eq. (4.29) to Eq. (4.8). Applying the above concepts to LGT, the group of gauge transformations $\mathcal{G}$ is a stabilizer group, and $\mathcal{H}_{\text{inv}}$ corresponds to the code space. The projection operator $\hat{P}_{\text{inv}}$ from $\mathcal{H}_{\text{gauge}}$ to $\mathcal{H}_{\text{inv}}$ is the (normalized) sum of all stabilizers. [2] Measuring whether and how gauge symmetry is violated allows one to detect and correct gauge-violating errors.

In active QEC, one measures a minimum generating set of $\mathcal{S}$, and the results are *syn-*

2. We will reserve the terms "physical states (space)" for the gauge-symmetric ones in the LGT which is unfortunately different from the convention of the QEC literature. Terms "physical qubits (qudits, noise)" still refer to any qubits (qudits, noise) in $\mathcal{H}_{\text{full}}$, consistent with QEC literature.

dromes. To avoid collapsing the quantum information in the measurement of syndromes, ancillae are needed to compute the syndromes coherently:

$$[\sum_X \psi(X)\,|X\rangle\,] \otimes |0\rangle_{\text{anc}} \rightarrow \sum_X \psi(X)\,|X\rangle \otimes |s(X)\rangle_{\text{anc}}\,, \tag{4.30}$$

where $|X\rangle$ are base vectors of the physical qubits. In the case of Pauli stabilizers with eigenvalue ± 1, measuring the ancillary qubits collapses the state to $\mathcal{H}_{\text{code}}$ when all syndromes return $+1$, or one of the subspaces orthogonal to $\mathcal{H}_{\text{code}}$ if some syndromes return -1 indicate the errors. One then applies an optimal recovery operation to the quantum state depending on the syndromes. Clearly, errors that transform one state to another within $\mathcal{H}_{\text{code}}$ are not detectable, and those are *logical errors*.

The *code distance* is the minimum number of single physical qubit (qudit) errors that are part of a logical error. For scalable quantum error correction codes, which imply that the code distance can be arbitrarily large, there exists an *error threshold* for the error rate per physical qudit. If the physical error rate is below such threshold, we can decrease the logical error rate by increasing the code distance, despite the increased total errors due to more physical qudits [263–265].

4.2.2 The set of correctable errors

For a quantum system represented as a density operator ρ, the general noisy evolution can be written as a completely positive, trace-preserving map $\mathcal{N}(\rho)$:

$$\mathcal{N}(\rho) = \sum_j \hat{N}_j \rho \hat{N}_j^\dagger \tag{4.31}$$

where $\hat{N}_j$ are error operators, usually including the identity operator. The necessary and sufficient condition for correctable errors is the Knill-Laflamme (KL) condition [274]:

$$\hat{P}_{\text{code}}\hat{N}_i^\dagger \hat{N}_j \hat{P}_{\text{code}} = \lambda_{ij}\hat{P}_{\text{code}}, \quad \lambda_{ij}^* = \lambda_{ji}. \tag{4.32}$$

For errors as operators on a G-register, a linearly independent complete basis can be constructed as $\{\hat{L}_g\hat{\Gamma}_\sigma\}$, where $\hat{L}_g$ is the group left multiplication operator defined in Eq. (4.5), and $\hat{\Gamma}_\sigma$ is the matrix element operator: [3]

$$\hat{\Gamma}_{\sigma,m,n} = \sum_{h\in G} \sqrt{d_\sigma}\Gamma^{(\sigma)}_{mn}(h)^* \left|h\right\rangle \left\langle h\right| \tag{4.33}$$

One can check that the above set of operators are linearly independent by satisfying:

$$\text{tr}\left[(\hat{L}_g\hat{\Gamma}_\sigma)^\dagger(\hat{L}_{g'}\hat{\Gamma}_{\sigma'})\right] = |G|\delta_{g,g'}\delta_{\sigma,\sigma'}. \tag{4.34}$$

The basis is complete as there are only $|G|^2$ independent operators in a Hilbert space of dimension $|G|$.

The gauge-violating effect of $\hat{\Gamma}_\sigma$ is clearer in the electric basis. Using Eq. (4.63) between Clebsch-Gordan coefficients and the matrix elements of irreps in [275], one can derive:

$$\begin{aligned}&\left\langle \sigma''_{lr}\right| \hat{\Gamma}_{\sigma,m,n} \left|\sigma'_{kq}\right\rangle = \\ &\sqrt{\frac{d_\sigma d_{\sigma'}}{d_{\sigma''}}} \sum_\alpha \left\langle \sigma''_l, \alpha|\sigma'_k, \sigma_m\right\rangle \left\langle \bar{\sigma}''_r, \alpha|\bar{\sigma}'_q, \bar{\sigma}_n\right\rangle,\end{aligned} \tag{4.35}$$

where $\left\langle \sigma''_l, \alpha|\sigma'_k, \sigma_m\right\rangle$ is the Clebsch-Gordan coefficient, and the sum of α is from 1 to the multiplicity $M(\sigma'';\sigma',\sigma)$, i.e. the number of times that σ'' appears in the direct sum decomposition of the tensor product of σ and σ'. This can be interpreted as $\hat{\Gamma}_{\sigma,m,n}$ adding σ_m

3. Γ_σ is short for $\Gamma_{\sigma,m,n}$, where σ is the irrep, and m, n indicated the matrix element in the representation. The number of different $\Gamma_{\sigma,m,n}$ is therefore $\sum_\sigma {d_\sigma}^2 = |G|$.

to the left vector and $\bar{\sigma}_n$ to the right vector. Thus, $\hat{\Gamma}_{\sigma,m,n}(\mathbf{x}, i)$ on a gauge-invariant state creates net flux σ_m at site $\mathbf{x}$ and $\bar{\sigma}_n$ at the site $(\mathbf{x}+\mathbf{i})$. Applying $\hat{\Gamma}^{\dagger}_{\sigma,m,n}$ to the same link annihilates the flux and restores gauge symmetry. Indeed, we can check in Appendix 4.2.3 that $\hat{\Gamma}_{\sigma}, \hat{\Gamma}_{\sigma'}$ on the same link satisfies the KL condition,

$$\hat{P}_{\text{inv}}\hat{\Gamma}^{\dagger}_{\sigma}\hat{\Gamma}_{\sigma'}\hat{P}_{\text{inv}} = \delta_{\sigma,\sigma'}\hat{P}_{\text{inv}}, \tag{4.36}$$

Thus $\hat{\Gamma}_{\sigma}$-type errors are correctable. Another way to obtain the conclusion is through the code distance d_{code}: for a QEC with code distance d_{code}, errors involving up to $[(d_{\text{code}}-1)/2]$ qudits are guaranteed to be correctable [39]. In our case, to make a logical error with $\hat{\Gamma}_{\sigma}$-type operators, one needs at least four links of a plaquette to form a Wilson loop, thus the code distance is 4. This makes any $[(4-1)/2] = 1$ $\hat{\Gamma}_{\sigma}$-type error correctable.

The errors induced by the $\hat{L}_g(\mathbf{x}, i)$ operator are not detectable if g is the Abelian center of the group as it commutes with the $\hat{P}_{\text{inv}}$. For g not in the Abelian center, if $\hat{L}_g(\mathbf{x}, i)$ drifts a state to another gauge invariant state, we can not detect such errors. On the other hand when the error $\hat{L}_g(\mathbf{x}, i)$ drifts a state out of the invariant Hilbert space by generating a local charge at site $\mathbf{x}$, we can measure the local charge at $\mathbf{x}$ and detect such errors. However, as $\hat{L}_g(\mathbf{x}, i)$ does not affect local charges at other sites, it is not possible to diagnose the link that $\hat{L}_g(\mathbf{x}, i)$ affects, and thus the errors are not correctable. The fact that $\hat{L}_g(\mathbf{x}, i)$ are not correctable can also be seen by checking the KL condition:

$$\hat{P}_{\text{inv}}\hat{L}^{\dagger}_{g'}\hat{L}_g\hat{P}_{\text{inv}} = \frac{1}{|G|}\sum_{h\in G}\hat{L}_{h^{-1}g'^{-1}gh}\hat{P}_{\text{inv}}. \tag{4.37}$$

The right hand side of Eq. (4.37) differs from Eq. (4.32) by an operator $\frac{1}{|G|}\sum_{h\in G}\hat{L}_{h^{-1}g'^{-1}gh}$, thus breaking the KL condition. In the Z_2 gauge theory, a Z_2-register is a qubit, and the complete basis reduces to the familiar Pauli operators $\{I, \hat{X}, \hat{Z}, \hat{X}\hat{Z}\}$, of which $\hat{\Gamma}_{\sigma} \in \{I, \hat{Z}\}$

are correctable.

The correctable error set can contain multiple-link $\hat{\Gamma}_\sigma$ errors, as long as the erroneous links are separated enough such that there is no ambiguity about which link causes the gauge violation. The easiest errors to decode are those that show up as pairs of charges in dual representations $\sigma, \bar{\sigma}$ at the two ends of a link, surrounded by neighboring sites all with zero charge. This requires the $\hat{\Gamma}_\sigma$ errors to be separated by at least two error-less links (Fig. 4.3), which we call the *minimal effort decoding condition (MED)*. The condition can be relaxed if more complicated classical processing is available. The KL condition requires any product of two error operators $\hat{N}_i$ and $\hat{N}_j$ to contain no non-trivial gauge-invariant operators, i.e. Wilson loops. This condition is fulfilled when the number of links affected by Γ_σ errors along any closed loop of perimeter C is at most $[\frac{C-1}{2}]$, thus eliminating the possibility of error links in $\hat{N}_i$ and $\hat{N}_j$ forming loops. Considering only the smallest loops, i.e. plaquettes, the local KL condition allows at most one $\hat{\Gamma}_\sigma$ error per plaquette.

4.2.3 Correctability of $\hat{\Gamma}_\sigma$

In this subsection, g, h are group elements, σ, τ are irreducible representations (irreps), and $k, l, m, n, q, r, s, t, u$ are the matrix elements of representations. To check Eq. (4.36), we will compute in the magnetic basis

$$\hat{P}_0(\mathbf{x})\hat{\Gamma}^\dagger_{\sigma',s,q}(\mathbf{x},i)\hat{\Gamma}_{\sigma,m,n}(\mathbf{x},i)\hat{P}_0(\mathbf{x}) = \frac{1}{|G|^2}\sum_{g,h\in G}\Bigg(\hat{R}_{g^{-1}}\hat{R}_{h^{-1}} \;\; \begin{array}{c} \hat{L}_g\hat{L}_h \\ \vdots \\ -\!\!\!

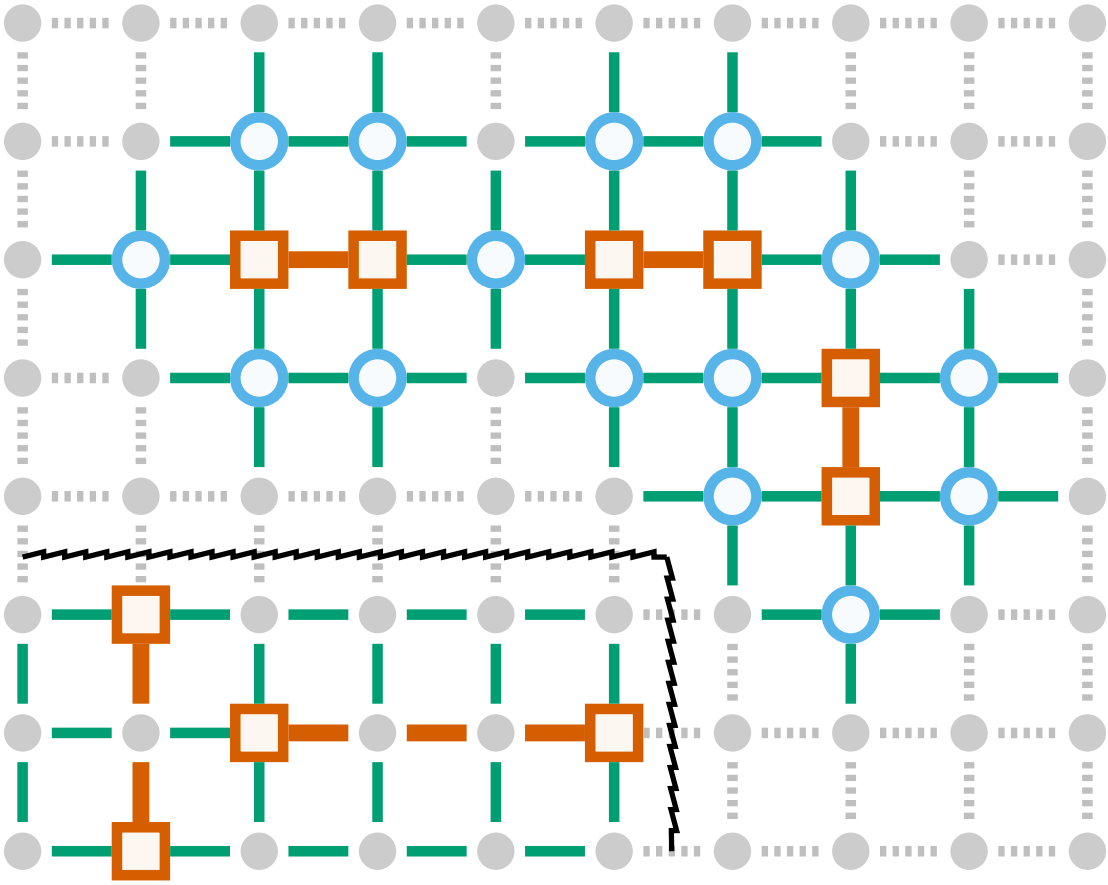

Figure 4.3: Examples of correctable error distributed on the lattice to satisfy the MED (upper-right) or the local KL condition (lower-left). The orange links are Γ-type errors, which must break gauge symmetry at the orange squares. The conditions require the green links to be error-less. For the MED condition, the adjacent sites (blue circles) must be charge-neutral. For the local KL condition, the error links are allowed to extend in a straight line, which is the shortest path to connect a pair of charges.

For the operators on the link $\mathbf{x}, i$,

$$\begin{aligned}\hat{L}_g\hat{\Gamma}^{\dagger}_{\sigma',s,q}\hat{\Gamma}_{\sigma,m,n}\hat{L}_h &= \sum_U |gU\rangle\langle U|\sqrt{d_\sigma d_{\sigma'}}\Gamma^{(\sigma')}_{sq}(U)\Gamma^{(\sigma)}_{mn}(U)^*\hat{L}_h \\ &= \sqrt{d_\sigma}\Big[\sum_{U,l}\Gamma^{(\sigma')}_{sl}(g^{-1})\Gamma^{(\sigma')}_{lq}(gU)\Big]\Big[\sum_k \Gamma^{(\sigma)}_{mk}(g^{-1})\Gamma^{(\sigma)}_{kn}(gU)\Big]^* |gU\rangle\langle U|\hat{L}_h \\ &= \sum_{k,l}\Gamma^{(\sigma')}_{sl}(g^{-1})\Gamma^{(\sigma)}_{mk}(g^{-1})^*\hat{\Gamma}^{\dagger}_{\sigma',l,q}\hat{\Gamma}_{\sigma,k,n}\hat{L}_g\hat{L}_h. \end{aligned} \tag{4.39}$$

Thus, let $h' = gh$,

$$\hat{P}_0(\mathbf{x})\hat{\Gamma}^{\dagger}_{\sigma',s,q}(\mathbf{x},i)\hat{\Gamma}_{\sigma,m,n}(\mathbf{x},i)\hat{P}_0(\mathbf{x}) \tag{4.40}$$

$$= \frac{1}{|G|^2}\sum_{h'\in G}\Bigg(\hat{R}_{h'^{-1}} \;\; \begin{array}{c}\hat{L}_{h'}\\ \text{—}\!\!\bigcirc\!\!\text{—}\\ \hat{R}_{h'^{-1}}\end{array} \;\; \mathbf{x} \;\; \sum_{k,l,g}\Gamma^{(\sigma')}_{sl}(g^{-1})\Gamma^{(\sigma)}_{mk}(g^{-1})^*\hat{\Gamma}^{\dagger}_{\sigma',l,q}\hat{\Gamma}_{\sigma,k,n}\hat{L}_{h'}\Bigg). \tag{4.41}$$

With the orthogonality of matrix elements

$$\sum_g \Gamma^{(\sigma')}_{sl}(g^{-1})\Gamma^{(\sigma)}_{mk}(g^{-1})^* = \delta_{\sigma\sigma'}\delta_{ms}\delta_{lk}|G|/d_\sigma, \tag{4.42}$$

and the unitarity of representations Eq. (4.50), we get

$$\hat{P}_0(\mathbf{x})\hat{\Gamma}^{\dagger}_{\sigma',s,q}(\mathbf{x},i)\hat{\Gamma}_{\sigma,m,n}(\mathbf{x},i)\hat{P}_0(\mathbf{x}) = \delta_{\sigma'\sigma}\delta_{sm}\delta_{qn}\hat{P}_0(\mathbf{x}) \tag{4.43}$$

4.2.4 The encoding and decoding circuits

Conceptually, the encoding and decoding of gauge symmetry is easier in the electric basis, where Gauss's law reads as "zero electric flux at each vertex". For non-Abelian groups, the computation of the net flux requires the group's Clebsch-Gordan coefficients which are

not diagonal in the electric basis. We bypass some of the difficulties by doing an "effective Clebsch-Gordan sum" in the group element basis. We derive in Appendix 4.3 that the Clebsch-Gordan sum is equivalent to group multiplications in the group element basis. With this, we can encode and decode Gauss's law using the following primitive gates [82] acting on group registers:

- Inverse gate: $\mathfrak{U}_{-1}|g\rangle = \left|g^{-1}\right\rangle$,
- Left and Right Multiplication gates: $\mathfrak{U}^L_\times|g\rangle|U\rangle = |g\rangle|gU\rangle$, $\mathfrak{U}^R_\times|g\rangle|U\rangle = |g\rangle|Ug\rangle$,
- Fourier transform gate:

$$\mathfrak{U}_F = \sum_{g,\sigma_{mn}} \sqrt{\frac{d_\sigma}{|G|}} \Gamma^{(\sigma)}_{mn}(g) \left|\sigma_{mn}\right\rangle \langle g| \tag{4.44}$$

  which rotates the magnetic basis to the electric one,

- Group rotation gates in irreps. This uses a group register $|U\rangle$ as the control to rotate between the vectors in the d_σ-dimensional space:

$$\begin{aligned} \mathfrak{U}_\sigma &= \sum_{U\in G} (|U\rangle\langle U|) \otimes \Big(\sum_{m,n=1}^{d_\sigma} \Gamma^{(\sigma)}_{mn}(U) |n\rangle\langle m| \Big) \\ &= d_\sigma^{-1/2} \sum_{m,n=1}^{d_\sigma} \hat{\Gamma}^\dagger_{\sigma,m,n} \otimes (|n\rangle\langle m|) \end{aligned} \tag{4.45}$$

  where the second equality follows from Eq. (4.33). For Abelian groups, $\mathfrak{U}_\sigma$ is a one-register phase gate on $|U\rangle$.

Fig. 4.4 shows an example of encoding and decoding for the patch of 7 gauge links connected to 2 sites in the right corner of Fig. 4.1. To encode, the links U_3, U_7 in the

maximal tree are initialized to the color neutral state $|\mathbf{g}\rangle \equiv |G|^{-\frac{1}{2}} \sum_{g\in G} |g\rangle$, and then,

$$|U_1\rangle\,|U_2\rangle\,|\mathbf{g}\rangle\,|U_4\rangle \xrightarrow{\mathfrak{U}_{\rm enc}} |G|^{-\frac{1}{2}} \sum_{g\in G} |gU_1\rangle\,|gU_2\rangle \left|g^{-1}\right\rangle \left|U_4 g^{-1}\right\rangle \tag{4.46}$$

One can easily check the gauge invariance Eq. (4.6) for the two sites after the circuit $\mathcal{U}_{\rm enc}$ in Fig. 4.4:

$$\begin{aligned} &\hat{T}_h\,|G|^{-\frac{1}{2}} \sum_{g\in G} |gU_1\rangle\,|gU_2\rangle \left|g^{-1}\right\rangle \left|U_4 g^{-1}\right\rangle \\ =&|G|^{-\frac{1}{2}} \sum_{g'=hg\in G} \left|g'U_1\right\rangle \left|g'U_2\right\rangle \left|g'^{-1}\right\rangle \left|U_4 g'^{-1}\right\rangle \end{aligned} \tag{4.47}$$

In the electric basis, the circuit computes the net flux of U_1, U_2, U_4 and stores it into the tree-link U_3, thus making the total net flux at the vertex to be zero. The same process is repeated for every vertex except $\mathbf{x_0}$. Sites in the same branch of the maximal tree should be processed in sequence, from the top of the branch to the root, and different branches can be encoded in parallel.

The above procedure initializes the state to the gauge invariant one $|\Psi_{\rm inv}\rangle$. During the noisy process in Fig. 4.2, suppose an error $\hat{\Gamma}_{\sigma,m,n}(\mathbf{x}, i)$ turns $|\Psi_{\rm inv}\rangle$ into $\hat{\Gamma}_{\sigma,m,n}(\mathbf{x}, i)\,|\Psi_{\rm inv}\rangle$, creating a net flux of σ_m at $\mathbf{x}$ and $\bar{\sigma}_n$ at $\mathbf{x}+\mathbf{i}$. We can decode this error pattern with the circuit $\mathcal{U}_{\rm dec}$, which adds the electric fluxes coherently to the ancillary registers originally initialized to color neutral states. Then in the decoding (derived 4.2.5),

$$\begin{aligned} &\hat{\Gamma}_{\sigma,m,n}\,|\Psi_{\rm inv}\rangle \otimes |\mathbf{g}\rangle \otimes |\mathbf{g}\rangle \xrightarrow{\mathcal{U}_{\rm dec}} \\ &\frac{1}{d_\sigma} \sum_{q,r}^{d_\sigma} \hat{\Gamma}_{\sigma,q,r}\,|\Psi_{\rm inv}\rangle \otimes \left|\sigma_{mq}(\mathbf{x})\right\rangle \otimes |\bar{\sigma}_{nr}(\mathbf{x}+\mathbf{i})\rangle\,. \end{aligned} \tag{4.48}$$

For non-Abelian groups, $\mathcal{U}_{\rm dec}$ preserves the quantum numbers $\sigma, \bar{\sigma}$, but m, n can change into

any integer in $[1, d_\sigma]$, and the corresponding new quantum numbers q, r are entangled with the ancillae.

To correct gauge-violating errors, the representation of the ancillary register at every site needs to be measured. This requires the quantum numbers σ, m, n in the Fourier basis to be stored in different qubits, and thus one can measure σ without collapsing m, n. Measuring $|\sigma\rangle$ in the trivial representation confirms the local gauge symmetry. Measuring any other $|\sigma\rangle$ indicates a gauge-violating error, and projects the gauge fields to a subspace orthogonal to $\mathcal{H}_{\text{inv}}$ in $\mathcal{H}_{\text{gauge}}$. In this example, a pair of non-trivial representations $|\sigma\rangle, |\bar{\sigma}\rangle$ on the two ends of a link are measured, which indicates a $\hat{\Gamma}_\sigma$ error on the link, and the quantum numbers $|m\rangle |q\rangle, |n\rangle |r\rangle$ of the ancillae are entangled with the gauge field state. The recovery can be performed with $\mathfrak{U}_\sigma$ in Eq. (4.45):

$$\begin{aligned}
&\frac{1}{d_\sigma} \sum_{q,r}^{d_\sigma} \hat{\Gamma}_{\sigma,q,r} |\Psi_{\text{inv}}\rangle \otimes (|m\rangle |q\rangle) \otimes (|n\rangle |r\rangle) \xrightarrow{\mathcal{U}_{\text{rec}}} \\
&\frac{1}{d_\sigma^{3/2}} \sum_{q,k,r}^{d_\sigma} \hat{\Gamma}^\dagger_{\sigma,q,k} \hat{\Gamma}_{\sigma,q,r} |\Psi_{\text{inv}}\rangle \otimes (|m\rangle |k\rangle) \otimes (|n\rangle |r\rangle) \\
&= |\Psi_{\text{inv}}\rangle \otimes \left[\frac{1}{d_\sigma^{1/2}} \sum_{r}^{d_\sigma} (|m\rangle |r\rangle) \otimes (|n\rangle |r\rangle) \right],
\end{aligned} \tag{4.49}$$

where we have used the unitarity of representations,

$$d_\sigma^{-1} \sum_{q=1}^{d_\sigma} \hat{\Gamma}^\dagger_{\sigma,q,k} \hat{\Gamma}_{\sigma,q,r} = \delta_{k,r}. \tag{4.50}$$

Thus $|\Psi_{\text{inv}}\rangle$ is recovered and unentangled with ancillae. At this point, since the quantum information in the ancillae is irrelevant to the gauge system, one can recycle the ancillae and re-initialize them to $|\mathbf{g}\rangle$ for the next round of error detection and correction.

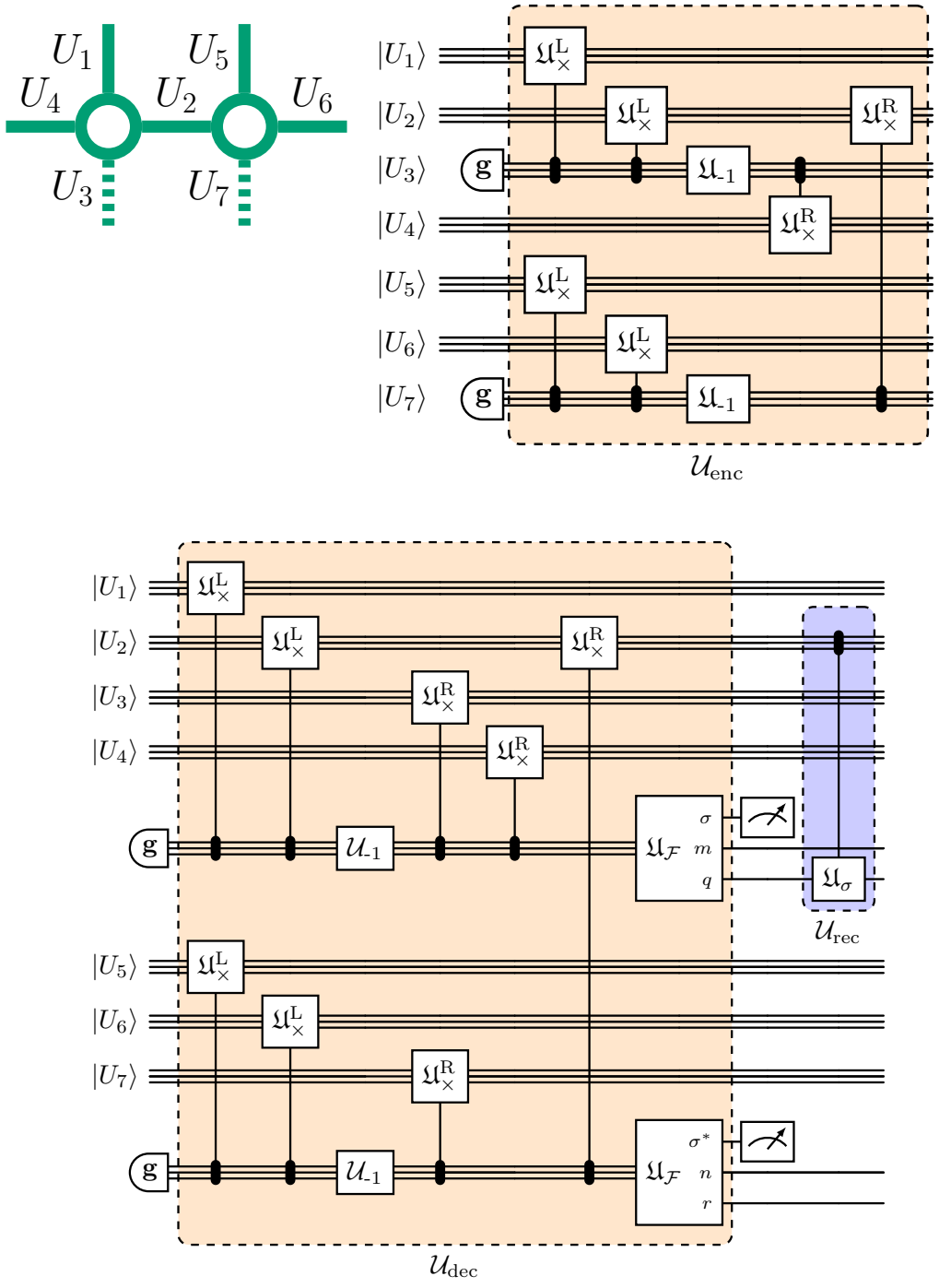

Figure 4.4: Encoding and decoding circuits for the patch in Fig. 4.1. (top) Circuit for preparing gauge-invariant states, and (bottom) Gauss's law measurement and recovery circuit, where measuring a pair of charges $\sigma, \bar{\sigma}$ on the two ancillae indicates a gauge-violating error on $|U_2\rangle$.

4.2.5 Derivation of Eq. (4.48) in the group element basis

$\mathcal{U}_{\text{dec}}$ performs the following for a gauge field state $|\Psi\rangle$:

$$|\Psi\rangle \otimes (|G|^{-\frac{1}{2}} \sum_{g\in G} |g\rangle) \xrightarrow{\mathfrak{U}_\times^L,\mathfrak{U}_\times^L,\mathfrak{U}_{-1},\mathfrak{U}_\times^R,\mathfrak{U}_\times^R} |G|^{-\frac{1}{2}} \sum_{g\in G} \hat{T}_g(\mathbf{x}) |\Psi\rangle \otimes \left|g^{-1}\right\rangle$$

$$\xrightarrow{QFT} \sum_{g\in G} \hat{T}_g(\mathbf{x}) |\Psi\rangle \otimes \Big(\sum_{\sigma,m,n} \frac{\sqrt{d_\sigma}}{|G|} \Gamma^{(\sigma)}_{mn}(g^{-1}) |\sigma\rangle \Big) \tag{4.51}$$

$$= \sum_{\sigma,m,n} \hat{P}_{\sigma_{mn}}(\mathbf{x}) |\Psi\rangle \otimes |\sigma_{mn}\rangle , \tag{4.52}$$

where

$$\hat{P}_{\sigma_{mn}}(\mathbf{x}) \equiv \frac{\sqrt{d_\sigma}}{|G|} \sum_{g\in G} \Gamma^{(\sigma)}_{mn}(g^{-1}) \hat{T}_g(\mathbf{x}) \tag{4.53}$$

For the trivial representation $\sigma = 0$, $\hat{P}_0(\mathbf{x})$ is the projection to the subspace invariant under local gauge transformations and $\hat{P}_0(\mathbf{x}) |\Psi\rangle_{\text{inv}} = |\Psi\rangle_{\text{inv}}$. When a correctable error $\hat{\Gamma}_\sigma$ occurs on one gauge register, consider

$$\hat{P}_{\sigma'_{sq}}(\mathbf{x}) \hat{\Gamma}_{\sigma,m,n}(\mathbf{x},i) \hat{P}_0(\mathbf{x}) = \frac{\sqrt{d_\sigma}}{|G|^2} \sum_{g,h\in G} \Gamma^{(\sigma')}_{sq}(g^{-1}) \Big(\hat{R}_{g^{-1}} \hat{R}_{h^{-1}} \; \overset{\hat{L}_g \hat{L}_h}{\underset{\hat{R}_{g^{-1}} \hat{R}_{h^{-1}}}{-\!\!\!\bigcirc\!\!\!-}} \; \mathbf{x} \; \hat{L}_g \hat{\Gamma}_{\sigma,m,n} \hat{L}_h \Big), \tag{4.54}$$

use the "commutation relation" to replace $\hat{L}_g \hat{\Gamma}_\sigma$ on the link $(\mathbf{x}, i)$ with

$$\hat{L}_g \hat{\Gamma}_{\sigma,m,n} = \sum_U |gU\rangle \langle U| \sqrt{d_\sigma} \Gamma^{(\sigma)}_{mn}(U)^* \tag{4.55}$$

$$= \sum_U |gU\rangle \langle U| \sqrt{d_\sigma} [\sum_k \Gamma^{(\sigma)}_{mk}(g^{-1}) \Gamma^{(\sigma)}_{kn}(gU)]^* = \sum_k \Gamma^{(\sigma)}_{mk}(g^{-1})^* \hat{\Gamma}_{\sigma,k,n} \hat{L}_g, \tag{4.56}$$

and let $h' = gh$, Eq. (4.54) can be simplified as

$$\hat{P}_{\sigma'_{sq}}(\mathbf{x})\hat{\Gamma}_{\sigma,m,n}(\mathbf{x},i)\hat{P}_0(\mathbf{x}) = \frac{\sqrt{d_\sigma}}{|G|^2}\sum_g \Gamma^{(\sigma')}_{sq}(g^{-1})\sum_k \Gamma^{(\sigma)}_{mk}(g^{-1})^*\sum_{h'}\Bigg(\; \hat{R}_{h'^{-1}} \; \overset{\hat{L}_{h'}}{\underset{\hat{R}_{h'^{-1}}}{\mathbf{x}}} \; \hat{\Gamma}_{\sigma,k,n}\hat{L}_{h'} \;\Bigg).$$

(4.57)

Using the orthogonality Eq. (4.42), we get

$$\hat{P}_{\sigma'_{sq}}(\mathbf{x})\hat{\Gamma}_{\sigma,m,n}(\mathbf{x},i)\hat{P}_0(\mathbf{x}) = \delta_{\sigma'\sigma}\delta_{sm}d_\sigma^{-1/2}\hat{\Gamma}_{\sigma,q,n}(\mathbf{x},i)\hat{P}_0(\mathbf{x}). \tag{4.58}$$

Similarly for $(\mathbf{x}+\mathbf{i})$ at the other end of the erroneous link,

$$\hat{R}_{g^{-1}}\hat{\Gamma}_{\sigma,m,n} = \sum_k \Gamma^{(\sigma)}_{kn}(g)^*\hat{\Gamma}_{\sigma,m,k}\hat{R}_{g^{-1}}, \tag{4.59}$$

and

$$\hat{P}_{\sigma''_{tr}}(\mathbf{x}+\mathbf{i})\hat{\Gamma}_{\sigma,q,n}(\mathbf{x},i)\hat{P}_0(\mathbf{x}+\mathbf{i}) = \delta_{\sigma''\bar{\sigma}}\delta_{tn}d_\sigma^{-1/2}\hat{\Gamma}_{\sigma,q,r}(\mathbf{x},i)\hat{P}_0(\mathbf{x}+\mathbf{i}). \tag{4.60}$$

Combining Eq. (4.58) and Eq. (4.60) gives

$$\hat{P}_{\sigma''_{tr}}(\mathbf{x}+\mathbf{i})\hat{P}_{\sigma'_{sq}}(\mathbf{x})\hat{\Gamma}_{\sigma,m,n}(\mathbf{x},i)\hat{P}_0(\mathbf{x})\hat{P}_0(\mathbf{x}+\mathbf{i}) = \delta_{\sigma.\sigma'}\delta_{\sigma''\bar{\sigma}}\delta_{sm}\delta_{tn}\frac{1}{d_\sigma}\hat{\Gamma}_{\sigma,q,r}(\mathbf{x},i)\hat{P}_0(\mathbf{x})\hat{P}_0(\mathbf{x}+\mathbf{i}). \tag{4.61}$$

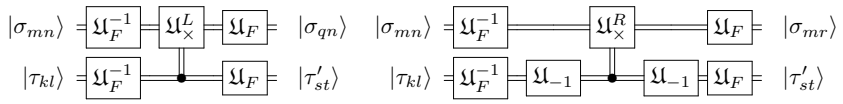

Figure 4.5: Quantum circuits implementing Clebsch-Gordan sums for generic finite groups. (left) $\mathfrak{U}_{CG}^L$ and (right) $\mathfrak{U}_{CG}^R$

Using the fact $\hat{P}_0(\mathbf{x})\hat{P}_0(\mathbf{x}+\mathbf{i})\left|\Psi\right\rangle_{\text{inv}} = \left|\Psi\right\rangle_{\text{inv}}$, the outcome of $\mathcal{U}_{\text{dec}}$ the gauge field state $\hat{\Gamma}_{\sigma,m,n}(\mathbf{x},i)\left|\Psi\right\rangle_{\text{inv}}$ is

$$\begin{aligned}
&\sum_{\sigma'_{sq},\sigma''_{tr}} \hat{P}_{\sigma''_{tr}}(\mathbf{x}+\mathbf{i})\hat{P}_{\sigma'_{sq}}(\mathbf{x})\hat{\Gamma}_{\sigma,m,n}(\mathbf{x},i)\left|\Psi\right\rangle_{\text{inv}} \otimes \left|\sigma'_{sq}(\mathbf{x})\right\rangle \otimes \left|\sigma''_{tr}(\mathbf{x}+\mathbf{i})\right\rangle \\
&= \sum_{q,r} \frac{1}{d_\sigma}\hat{\Gamma}_{\sigma,q,r}(\mathbf{x},i)\left|\Psi\right\rangle_{\text{inv}} \otimes \left|\sigma'_{sq}(\mathbf{x})\right\rangle \otimes \left|\sigma''_{tr}(\mathbf{x}+\mathbf{i})\right\rangle
\end{aligned} \tag{4.62}$$

4.3 Clebsch-Gordan sum in the group element basis

The relation between Clebsch-Gordan coefficients and matrix elements of the representations [275] is :

$$\frac{d_{\sigma''}}{|G|}\sum_{g\in G}\Gamma^{(\sigma)}_{mn}(g)\Gamma^{(\sigma')}_{kq}(g)\Gamma^{(\sigma'')}_{lr}(g)^* = \sum_\alpha \left\langle \sigma''_r,\alpha|\sigma_n,\sigma'_q\right\rangle \left\langle \sigma_m,\sigma'_k|\sigma''_l,\alpha\right\rangle . \tag{4.63}$$

The Clebsch-Gordan coefficients satisfy $\left\langle \sigma_n,\sigma'_q|\sigma''_r,\alpha\right\rangle^* = \left\langle \bar{\sigma}_n,\bar{\sigma}'_q|\bar{\sigma}''_r,\alpha\right\rangle$. We can also choose the phases of representation to satisfy $\left\langle \sigma''_r,\alpha|\sigma_n,\sigma'_q\right\rangle = \left\langle \sigma_n,\sigma'_q|\sigma''_r,\alpha\right\rangle^*$, which will be used for later discussions.

With Eq. (4.63), we show that the group multiplications Fourier transformed to the representation basis is equivalent to the addition of representations according to the Clebsch-

Gordan coefficients (Fig. 4.5).

$$\begin{aligned}\mathfrak{U}^L_{CG} =&\frac{\sqrt{d_\sigma d_{\sigma'_1} d_\tau d_{\tau'}}}{|G|^2}\Gamma^{(\sigma')}_{qr}(g_2g_1)\Gamma^{(\tau')}_{st}(g_2)\Gamma^{(\sigma)}_{mn}(g_1)^*\Gamma^{(\tau)}_{kl}(g_2)^*\big(\,|\sigma'_{qr}\rangle\otimes|\tau'_{st}\rangle\,\langle\sigma_{mn}|\otimes\langle\tau_{kl}|\,\big)\\ =&\frac{\sqrt{d_\sigma d_{\sigma'_1} d_\tau d_{\tau'}}}{|G|^2}\Gamma^{(\sigma')}_{qu}(g_2)\Gamma^{(\sigma')}_{ur}(g_1)\Gamma^{(\tau')}_{st}(g_2)\Gamma^{(\sigma)}_{mn}(g_1)^*\Gamma^{(\tau)}_{kl}(g_2)^*\big(\,|\sigma'_{qr}\rangle\otimes|\tau'_{st}\rangle\,\langle\sigma_{mn}|\otimes\langle\tau_{kl}|\,\big)\end{aligned} \tag{4.64}$$

where all the indices for group elements and group representations are summed over. Use the orthogonality Eq. (4.42) to sum g_1, giving

$$\begin{aligned}\mathfrak{U}^L_{CG} &= \frac{\sqrt{d_\tau d_{\tau'}}}{|G|}\Gamma^{(\sigma)}_{qm}(g_2)\Gamma^{(\tau')}_{st}(g_2)\Gamma^{(\tau)}_{kl}(g_2)^*\big(\,|\sigma_{qn}\rangle\otimes|\tau'_{st}\rangle\,\langle\sigma_{mn}|\otimes\langle\tau_{kl}|\,\big)\\ &= \frac{\sqrt{d_\tau d_{\tau'}}}{|G|}\big[\Gamma^{(\bar\sigma)}_{qm}(g_2)\Gamma^{(\tau')}_{st}(g_2)^*\,\Gamma^{(\tau)}_{kl}(g_2)\big]^*\big(\,|\sigma_{qn}\rangle\otimes|\tau'_{st}\rangle\,\langle\sigma_{mn}|\otimes\langle\tau_{kl}|\,\big),\end{aligned} \tag{4.65}$$

Finally apply Eq. (4.63) and convert the product of matrix elements to the Clebsch-Gordan coefficients,

$$\begin{aligned}\mathfrak{U}^L_{CG} &= \sqrt{d_\tau/d_{\tau'}}\big(\,\langle\tau'_t,\alpha|\bar\sigma_m,\tau_l\rangle\,\langle\bar\sigma_q,\tau_k|\tau'_s,\alpha\rangle\,\big)^*\big(\,|\sigma_{qn}\rangle\otimes|\tau'_{st}\rangle\,\langle\sigma_{mn}|\otimes\langle\tau_{kl}|\,\big)\\ &= \sqrt{d_\tau/d_{\tau'}}\,\langle\bar\tau'_t,\alpha|\sigma_m,\bar\tau_l\rangle\,\langle\sigma_q,\bar\tau_k|\bar\tau'_s,\alpha\rangle\,\big(\,|\sigma_{qn}\rangle\otimes|\tau'_{st}\rangle\,\langle\sigma_{mn}|\otimes\langle\tau_{kl}|\,\big)\end{aligned} \tag{4.66}$$

Thus through $\mathfrak{U}^L_{CG}$, σ in register 1 stays the same and τ in register 2 changes into τ'.

Thus, $\mathfrak{U}^L_{CG}$ "adds" the left vector in register 1 to register 2 according to the Clebsch-Gordan coefficients. For register 1, the process preserves quantum numbers σ, n but not necessarily m when the representation σ is not one-dimensional. The old flux σ_m is added to $\bar\tau_l$ and the new flux σ_q to $\bar\tau_k$. Similarly, $\mathfrak{U}^R_{CG}$ adds the right-vector in register 1 to register

2:

$$\begin{aligned}\mathfrak{U}^R_{CG} =& \frac{\sqrt{d_\sigma d_{\sigma'_1} d_\tau d_{\tau'}}}{|G|^2} \Gamma^{(\sigma')}_{qr}(g_1 g_2^{-1}) \Gamma^{(\tau')}_{st}(g_2) \Gamma^{(\sigma)}_{mn}(g_1)^* \Gamma^{(\tau)}_{kl}(g_2)^* \left(\left|\sigma'_{qr}\right\rangle \otimes \left|\tau'_{st}\right\rangle \langle \sigma_{mn}| \otimes \langle \tau_{kl}| \right) \\ =& \sqrt{d_\tau / d_{\tau'}} \left\langle \sigma_n, \tau_l | \tau'_t, \alpha \right\rangle \left\langle \tau'_s, \alpha | \sigma_r, \tau_k \right\rangle \left(|\sigma_{mr}\rangle \otimes \left|\tau'_{st}\right\rangle \langle \sigma_{mn}| \otimes \langle \tau_{kl}| \right) \end{aligned} \tag{4.67}$$

4.4 Comparison of quantum fidelities

4.4.1 Group-agnostic thresholds

LGT states can be stored in a set of G-registers in both the gauge-fixed and gauge-redundant digitization. The number of links needed is $N_L - N_T$ for the former and N_L for the latter. We further assume that errors on different registers are independent. Suppose the total rate for any error on a single register is ϵ. Then the quantum fidelities are lower bounded by the probability that no errors happen on any register:

$$F_{\text{fixed}} \geq (1-\epsilon)^{N_L - N_T} \tag{4.68}$$

$$F_{\text{red}} \geq (1-\epsilon)^{N_L} \tag{4.69}$$

With the gauge redundancy, certain configuration of $\hat{\Gamma}_\sigma$ errors are correctable via gauge symmetry checking and restoration. Suppose the correctable type error rate on a single register is ϵ_c. The lower bound for the fidelity after gauge-symmetry restoration is the probability that no error or only correctable errors happen:

$$F_{\text{restored}} \geq \sum_{n=0}^{N_L} Q_n \epsilon_c^n (1-\epsilon)^{N_L - n} = (1-\epsilon)^{N_L} \Xi \tag{4.70}$$

where Q_n is the number of ways to arrange n links with correctable errors in the lattice, such that the correctability condition is still satisfied, and Ξ is the factor by which the

gauge-symmetry restoration amplifies the fidelity:

$$\Xi = \sum_{n=0}^{N_L} Q_n z^n, \quad z = \frac{\epsilon_c}{1-\epsilon} \tag{4.71}$$

Comparing these two bounds Eq. (4.70) and Eq. (4.68), the condition for the gauge-symmetry restoration to give a higher fidelity than gauge fixing is

$$\Xi^{1/N_T} > (1-\epsilon)^{-1}. \tag{4.72}$$

This formula can be interpreted as an error threshold: the gauge redundancy increases the code distance of Γ_σ-type errors from 1 to 4. For the fidelity to increase with the increased code distance due to gauge redundancy, ϵ has to be below certain threshold.

The Q_n's are related to the independence polynomials of graphs (see Appendix 4.4.2 for details). We compute Q_n for a variety of L using the Python library `hobj` [276] up to $L = 20$ and $L = 11$ for 2d lattices with OBC and PBC, respectively, for both error-correction conditions. For 3d lattices, we are able to reach $L = 4$ for both OBC and PBC with MED condition, while only $L = 3$ for PBC with the KL condition due to limited computing resources. These Q_n are then used to compute the threshold: the ϵ where the two sides of Eq. (4.72) are equal at a given ϵ_c/ϵ. These are shown in black (blue) lines using OBC (PBC) in Fig. 4.6 and Fig. 4.7 for 2d and 3d lattices, respectively. Eq. (4.72) is satisfied in the parameter region below the lines, indicating that the gauge symmetry restoration provides higher fidelity than the gauge fixed case.

We observe two features from Fig. 4.6-4.7. First,the parameter regions to satisfy Eq. (4.72) only exist when $\epsilon_c/\epsilon \gtrsim 1/d$, which is consistent with the following analysis. Expanding Eq. (4.72) for small ϵ, with $Q_0 = 1, Q_1 = N_L$, we have:

$$1 + \frac{N_L}{N_T}\epsilon_c + O(\epsilon_c\epsilon) > 1 + \epsilon + O(\epsilon^2). \tag{4.73}$$

Thus, the correctable fraction of the total error rate for a single link, ϵ_c/ϵ, must satisfy

$$\frac{\epsilon_c}{\epsilon} > \frac{N_T}{N_L} \approx \frac{1}{d}, \tag{4.74}$$

with $\frac{N_T}{N_L} = \frac{1}{d}$ in the infinite volume limit as seen in Tab. 4.1. Second, in all the cases, the threshold ϵ increases as ϵ_c/ϵ increases. This is consistent with the qualitative reasoning that when a larger portion of errors are correctable, larger values of ϵ could be allowed while the redundancy still enables more correction than the errors it introduces.

Based on the error thresholds obtained at different L, we aim to extrapolate to $L \to \infty$ limit. We find that near $\epsilon = 0$, the threshold is a monotonic function of L in either boundary condition and approaches the same limit. In contrast, near $\epsilon_c/\epsilon = 1$ for 2d lattices, non-monotonic behavior is observed for small lattices with $L \leq 6$ due to finite volume effects. By restricting to the results for $L > 6$ at 2d lattice, we perform both quadratic and exponential extrapolations to obtain the threshold ϵ in the $L \to \infty$ limit which can be found in Fig. 4.6 (red line with the thickness quantifying error bar on extrapolations). For 3d lattice, as computing resources limit the calculations to only $L < 5$, the extrapolation to $L \to \infty$ cannot be reliably performed. For MED condition, the threshold curve with OBC near $\epsilon_c/\epsilon = 1$ exhibits a larger deviation from the PBC results at larger L, suggesting that $L < 5$ is far from the infinite limit. For the KL condition, calculations are limited to only $L = 2, 3$ with PBC, also precluding an extrapolation to infinity limit. Despite this, we expect the thresholds for $L \to \infty$ to be roughly bounded by the largest L results for OBC and PBC.

4.4.2 Correctable errors and independence polynomials

In this section, we explain our methods to compute Q_n – the number of possible ways to arrange n links with correctable errors in the lattice, such that the correctability condition is still satisfied, with tools of graph theory [276]. The method can be applied to lattices of

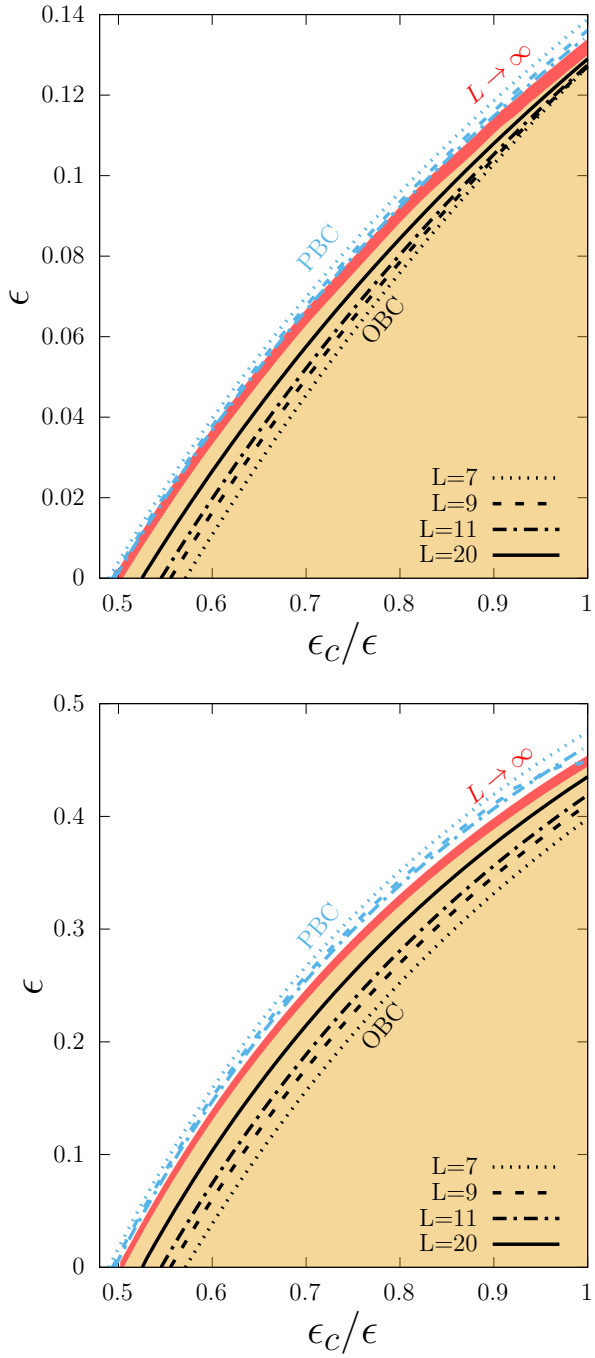

Figure 4.6: Error threshold lines in the $\epsilon - \epsilon_c/\epsilon$ plane below which $F_{\text{restored}} > F_{\text{fixed}}$, indicating that using gauge redundancy to detect and correct the errors is advantageous, for 2d lattices for (top) MED condition and (bottom) local KL condition. The shaded region is the infinite volume limit.

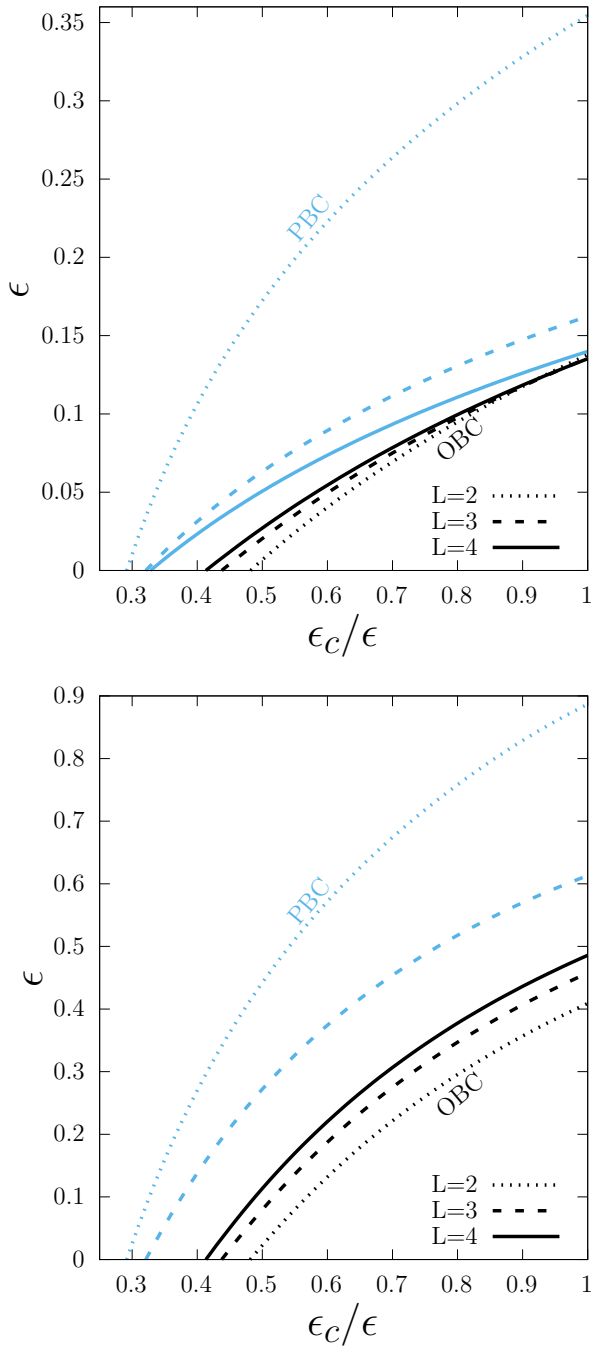

Figure 4.7: Error threshold lines in the $\epsilon - \epsilon_c/\epsilon$ plane below which $F_{\text{restored}} > F_{\text{fixed}}$, indicating that using gauge redundancy to detect and correct the errors is advantageous, for 3d lattices for (top) MED condition and (bottom) local KL condition.

generic shapes.

A graph consists of vertices and edges. An *independent subset* of vertices is a set of vertices in which no two vertices are adjacent to the same edge. The *independence polynomial* of a graph is

$$I(z) = \sum_n a_n z^n, \tag{4.75}$$

where a_n is the number of different independent subsets of n vertices in the graph.

For a finite lattice $\mathfrak{L}$, we create a corresponding graph $\mathfrak{L}'$ in the following way:

- convert each link of $\mathfrak{L}$ into a vertex of $\mathfrak{L}'$;
- for each pair of vertices in $\mathfrak{L}'$, create an edge adjacent to them, if the Γ_σ-type errors that occur simultaneously to the corresponding links in $\mathfrak{L}$ can break the correctability condition.

Thus, each way of arranging n erroneous links to satisfy the correctability condition corresponds to an independent subset of vertices in the new graph. This implies that Q_n is the number independent subsets of n vertices in the new graph and Ξ the independence polynomial.

For each lattice considered in Fig. 4.6 and Fig. 4.7, we construct the adjacency matrix of the corresponding graph $\mathfrak{L}'$ – an $N_L \times N_L$ matrix in which the element in row i and column j is 0 if the i, j-th vertices are independent, and 1 if they are adjacent to the same edge. We then use the Python library `hobj` [276] to compute the coefficients of the independence polynomials from the adjacent matrices. The connectivity for the MED condition would be higher than that for the KL condition.

4.4.3 ϵ, ϵ_c from error models

$\hat{N}_j$ on a G-register can always be decomposed as

$$\hat{N}_j = \sum_{g,\sigma} c_{j,g,\sigma} \hat{L}_g \hat{\Gamma}_\sigma. \tag{4.76}$$

The trace-preserving feature $\sum_j \hat{N}_j^\dagger \hat{N}_j = \mathbb{I}$ requires $\sum_{j,\sigma,g} |c_{j,g,\sigma}|^2 = 1$. When the noise channel is diagonal in this basis, i.e. for each $\hat{N}_j$ there is only one non-zero $c_{j,g,\sigma}$, such that we can relabel $c_{j,g,\sigma}$ to $c_{g,\sigma}$, the one-register noise channel can be written as

$$\mathcal{N}(\rho) = \sum_{g,\sigma} |c_{g,\sigma}|^2 \hat{L}_g \hat{\Gamma}_\sigma \rho (\hat{L}_g \hat{\Gamma}_\sigma)^\dagger. \tag{4.77}$$

The one register total error probability is

$$\epsilon = \sum_{g \neq \mathbb{I}, \sigma \neq \mathbb{I}} |c_{g,\sigma}|^2 = 1 - |c_{\mathbb{I},\mathbb{I}}|^2. \tag{4.78}$$

where $g \neq \mathbb{I}$ and $\sigma \neq \mathbb{I}$ mean, respectively, that the group element cannot be the identity, and the irreducible representation cannot be the trivial one. With this, the correctable error probability is

$$\epsilon_c = \sum_{\sigma \neq \mathbb{I}} |c_{\mathbb{I},\sigma}|^2 \tag{4.79}$$

We consider Z_N theory, where each G-register is a qudit with N states [255]. We represent the computational basis of the qudit as $|n\rangle$, where n is an integer in $[0, N-1]$. In the computational basis, define the clock shift operators

$$\hat{\chi} = \sum_{n=0}^{N-1} |n\rangle \langle (n+1) \bmod N| \tag{4.80}$$

and the phase shift operators

$$\hat{\nu} = \sum_{n=0}^{N-1} e^{2\pi i n/N} \left|n\right\rangle \left\langle n\right| . \tag{4.81}$$

For the group Z_N, both group elements g and group representations σ can be mapped to integers $[0, N-1]$. Thus we can choose to have the computational basis as either the group element or the electric basis. If we choose the group element basis, $\hat{L}_g$ are clock shifts

$$\hat{L}_g = (\hat{\chi})^g = \sum_{n=0}^{N-1} \left|n\right\rangle \left\langle (n+g) \bmod N\right| , \tag{4.82}$$

which preserves the gauge symmetry, and thus cannot be diagnosed by Gauss's law. The representation $\hat{\Gamma}_\sigma$ operators are phase shifts

$$\hat{\Gamma}_\sigma = (\hat{\nu})^\sigma = \sum_{n=0}^{N-1} e^{2\pi i n\sigma/N} \left|n\right\rangle \left\langle n\right| . \tag{4.83}$$

They break gauge symmetry unless they form closed Wilson loops.

If we choose the electric basis as the computational basis instead, as the phase shift is mapped to the $\hat{L}_g$ operator as $\hat{L}_g = (\hat{\nu})^g$, thus the phase shift errors would preserve the symmetry. While the clock shift is mapped to $\hat{\Gamma}_\sigma$ as $\hat{\Gamma}_\sigma = (\hat{\chi})^\sigma$, making the clock shift errors correctable.

Consider the error channel where single clock and phase shifts occur independently with

probabilities p_χ, p_ν :

$$\begin{aligned}\mathcal{N}(\rho) =&(1-p_\chi)(1-p_\nu)\rho \\ &+\frac{(1-p_\chi)p_\nu}{N-1}\sum_{i=1}^{N-1}(\hat{\nu})^i\rho(\hat{\nu})^{i\dagger} \\ &+\frac{(1-p_\nu)p_\chi}{N-1}\sum_{j=1}^{N-1}(\hat{\chi})^j\rho(\hat{\chi})^{j\dagger} \\ &+\frac{p_\nu p_\chi}{(N-1)^2}\sum_{i,j=1}^{N-1}(\hat{\nu})^i(\hat{\chi})^j\rho(\hat{\chi})^{j\dagger}(\hat{\nu})^{i\dagger}\end{aligned} \tag{4.84}$$

The one register total error probability is

$$\epsilon = 1-(1-p_\chi)(1-p_\nu) \tag{4.85}$$

In the group element basis, $(\hat{\nu})^\sigma$ are correctable, and thus

$$\epsilon_c = (1-p_\chi)p_\nu. \tag{4.86}$$

In the electric basis, $(\hat{\chi})^\sigma$ are correctable,

$$\epsilon_c = (1-p_\nu)p_\chi. \tag{4.87}$$

From this, we observe that the relative error probabilities of physical hardware can prefer different encodings. If the phase errors are more frequent than the clock errors ($p_\nu > p_\chi$), encoding in the group element basis will help to stay below the error thresholds with the total ϵ reasonably small.

The correctability of phase errors can be generalized to non-Abelian groups, if one chooses the group element basis encoding. This is because all operators diagonal in the group element

1-d representations		2-d representation	
$\hat{\Gamma}_{\text{triv}}$	$\hat{I}$	$\hat{\Gamma}_{2,1,1}$	$\hat{Z}_a\hat{Z}_b{}^{1/2}\frac{1+\hat{Z}_c}{2}$
$\hat{\Gamma}_{\text{i}-\text{ker}}$	$\hat{Z}_c$	$\hat{\Gamma}_{2,1,2}$	$\hat{Z}_a\hat{Z}_b{}^{1/2}\frac{1-\hat{Z}_c}{2}$
$\hat{\Gamma}_{\text{j}-\text{ker}}$	$\hat{Z}_b$	$\hat{\Gamma}_{2,2,1}$	$-\hat{Z}_a\hat{Z}_b{}^{3/2}\frac{1-\hat{Z}_c}{2}$
$\hat{\Gamma}_{\text{k}-\text{ker}}$	$\hat{Z}_b\hat{Z}_c$	$\hat{\Gamma}_{2,2,2}$	$\hat{Z}_a\hat{Z}_b{}^{3/2}\frac{1+\hat{Z}_c}{2}$

Table 4.2: Correctable errors $\hat{\Gamma}_\sigma$ for the quaternion group $\mathbb{Q}_8$ encoded in 3 qubits via $(-1)^a\mathbf{i}^b\mathbf{j}^c \to |abc\rangle$.

basis can be written as linear combinations of $\hat{\Gamma}_\sigma$. For example, in Tab. 4.2, we list the correctable errors for the 3-qubit encoding of the quaternion group $\mathbb{Q}_8 = \{(-1)^a\mathbf{i}^b\mathbf{j}^c\}$, where $a, b, c = 0$ or 1 [255]. It has four 1d representations and one 2d representation. All the Pauli-Z operators are correctable, as $\hat{Z}_b, \hat{Z}_c$ correspond to two 1-d representation operators, and $\hat{Z}_a$ is a linear combination of 2-d representation operators:

$$\hat{Z}_a = \frac{1}{1+i}(\hat{\Gamma}_{2,1,1} + \hat{\Gamma}_{2,1,2} - i\hat{\Gamma}_{2,2,1} + i\hat{\Gamma}_{2,2,2}). \tag{4.88}$$

Thus, for the error model that allows one of the three qubits to have a Pauli error,

$$\begin{aligned}\mathcal{N}(\rho) =&(1 - 3p_X - 3p_Y - 3p_Z)\rho + p_X \sum_{i=a,b,c} \hat{X}_i\rho\hat{X}_i \\ &+ p_Y \sum_{i=a,b,c} \hat{Y}_i\rho\hat{Y}_i + p_Z \sum_{i=a,b,c} \hat{Z}_i\rho\hat{Z}_i\end{aligned} \tag{4.89}$$

with the one-register error rate being $3(p_X + p_Y + p_Z)$, the correctable fraction is

$$\frac{\epsilon_c}{\epsilon} = \frac{p_Z}{p_X + p_Y + p_Z}. \tag{4.90}$$

If the qubits have more phase errors and fewer bit-flip errors, encoding in the group element basis is preferable.

4.5 Conclusions

In this chapter, we explore how the natural gauge redundancy of lattice gauge theories can become a tool to create partial error correction codes for quantum simulations. For generic groups, treating the gauge transformations in lattice gauge theories as stabilizers and the gauge-invariant subspace as the code space, we identify the correctable errors in one lattice link, as well as the MED and KL conditions for multiple link errors to remain correctable. We construct the quantum circuits to prepare gauge invariant states including redundant degrees of freedoms, as well as to detect and recover the correctable errors.

We calculate the error-rate thresholds below which keeping gauge redundancy is preferable to gauge fixing for error-correcting purposes, under both the MED and KL conditions. We do this by comparing the quantum fidelities when errors exist, which is the probability that either no error happens or only correctable errors happen. The thresholds depend on the correctable fraction of the error rate in a single link, ϵ_c/ϵ. We find a simple analytic relation at leading order in ϵ for when gauge redundancy is advantageous: $\epsilon_c/\epsilon \geq 1/d$ for a d dimensional lattice. Numerical results demonstrate that this relation is robust for realistic error rates. Thus for quantum devices where error correction is possible, $\epsilon \ll 1$, our results can be a guidance to design digitizations. To provide examples of how one may apply such thresholds, we obtain ϵ_c/ϵ explicitly for the discrete Abelian group $\mathbb{Z}_N$ and the non-Abelian group $\mathbb{Q}_8$ assuming certain reasonable error models.

Consideration of similar error thresholds should be generalized to other digitization schemes and error models. The quantitative values of the thresholds found in this chapter can vary depending on the computational tasks and the hardware. Future research directions should also take into account non-diagonal error channels, quantum architectures and inclusion of fermions on the lattice sites.

CHAPTER 5

OUTLOOK

In this thesis, I have given an overview of the quantum simulations of real-time dynamics of strongly interacting QFTs, and used classical and quantum methods to improve the efficiency and accuracy. They are examples of addressing theoretical and algorithmic challenges to pave the way for quantum advantage in the hard problems of particle physics. This field is still at its early days and there is much more to do.

On the theory front, there remains the challenge to efficiently approximate and approach the continuum theory with a finite number of qubits. Here, we can benefit from the lens of renormalization as well. For example, one can formulate the difference between the continuous and digitized theories as operators in effective field theories and study their behavior under renormalization group flows. Another fruitful approach is to directly study the phases and universality classes of the digitized theories and look for emergent continuous symmetries. Active explorations are underway, with both perturbative methods such as the background effective field theories, and non-perturbative methods including duality transformations and Euclidean LGTs. With such knowledge about the digitized theories, we can analyze the errors introduced by field digitization before performing large-scale quantum simulations.

While this thesis focuses on the application of beyond-NISQ devices in the future, the rapid experimental developments strongly motivate us to bridge the remaining gap between scientific goals and realistic quantum devices. Currently, it is the coherent time of quantum systems rather than the number of qubits that poses a more severe challenge. Thus, the preparation of the initial states, which are typically low-energy states in a very high dimensional system, is a bottleneck problem towards realistic real-time quantum simulations as it usually takes deep quantum circuits. There is considerable room for improvement and much shared interest with other research areas, such as quantum chemistry and quantum optimization.

Ultimately, solving relevant real-time dynamic problems of QCD will require large-scale QCs with at least tens of thousands of high-quality qubits. A promising paradigm to realize this is quantum networking, which distributes the quantum computation tasks to a number of smaller quantum processors with quantum communication among them. With local Hamiltonians, the real-time quantum simulations should be naturally distributable. Investigating how to perform quantum simulations of LGTs with quantum networking will benefit both scientific goals in particle physics and the broader development of quantum technology.

BIBLIOGRAPHY

[1]A. Polkovnikov and V. Gritsev, "Breakdown of the adiabatic limit in low-dimensional gapless systems", Nature Physics **4**, 477–481 (2008).

[2]S. Baum, M. Carena, N. R. Shah, C. E. M. Wagner, and Y. Wang, "Nucleation is more than critical: A case study of the electroweak phase transition in the NMSSM", JHEP **03**, 055 (2021).

[3]A. Riera, C. Gogolin, and J. Eisert, "Thermalization in nature and on a quantum computer", Phys. Rev. Lett. **108**, 080402 (2012).

[4]A. M. Czajka, Z.-B. Kang, H. Ma, and F. Zhao, "Quantum simulation of chiral phase transitions", JHEP **08**, 209 (2022).

[5]T. D. Cohen, H. Lamm, S. Lawrence, and Y. Yamauchi (NuQS), "Quantum algorithms for transport coefficients in gauge theories", Phys. Rev. D **104**, 094514 (2021).

[6]H. Lamm, S. Lawrence, and Y. Yamauchi (NuQS), "Parton physics on a quantum computer", Phys. Rev. Res. **2**, 013272 (2020).

[7]M. Kreshchuk, W. M. Kirby, G. Goldstein, H. Beauchemin, and P. J. Love, *Quantum Simulation of Quantum Field Theory in the Light-Front Formulation*, Feb. 2020.

[8]M. Echevarria, I. Egusquiza, E. Rico, and G. Schnell, *Quantum Simulation of Light-Front Parton Correlators*, Nov. 2020.

[9]C. W. Bauer, M. Freytsis, and B. Nachman, "Simulating Collider Physics on Quantum Computers Using Effective Field Theories", Phys. Rev. Lett. **127**, 212001 (2021).

[10]T. Li, X. Guo, W. K. Lai, X. Liu, E. Wang, H. Xing, D.-B. Zhang, and S.-L. Zhu (QuNu), "Partonic collinear structure by quantum computing", Phys. Rev. D **105**, L111502 (2022).

[11]T. V. Zache, D. González-Cuadra, and P. Zoller, *Fermion-qudit quantum processors for simulating lattice gauge theories with matter*, Mar. 2023.

[12]P. E. Gibbs, *Understanding Finite Baryonic Density Simulations in Lattice QCD*, May 1986.

[13]P. Gibbs, "Lattice Monte Carlo Simulations of {QCD} at Finite Baryonic Density", Phys. Lett. B **182**, 369–372 (1986).

[14]M. Troyer and U.-J. Wiese, "Computational complexity and fundamental limitations to fermionic quantum Monte Carlo simulations", Phys. Rev. Lett. **94**, 170201 (2005).

[15]X. Ji, Y. Liu, Y.-S. Liu, J.-H. Zhang, and Y. Zhao, "Large-momentum effective theory", Rev. Mod. Phys. **93**, 035005 (2021).

[16]P. de Forcrand, *Simulating qcd at finite density*, 2010.

[17]A. Alexandru, P. F. Bedaque, H. Lamm, S. Lawrence, and N. C. Warrington, "Fermions at Finite Density in 2+1 Dimensions with Sign-Optimized Manifolds", Phys. Rev. Lett. **121**, 191602 (2018).

[18]W. Detmold, G. Kanwar, H. Lamm, M. L. Wagman, and N. C. Warrington, "Path integral contour deformations for observables in $SU(N)$ gauge theory", Phys. Rev. D **103**, 094517 (2021).

[19]R. P. Feynman, "Simulating physics with computers", Int. J. Theor. Phys. **21**, 467–488 (1982).

[20]S. P. Jordan, H. Krovi, K. S. Lee, and J. Preskill, "BQP-completeness of Scattering in Scalar Quantum Field Theory", Quantum **2**, 44 (2018).

[21]M. C. Bañuls et al., "Simulating Lattice Gauge Theories within Quantum Technologies", Eur. Phys. J. D **74**, 165 (2020).

[22]C. W. Bauer et al., "Quantum Simulation for High-Energy Physics", PRX Quantum **4**, 027001 (2023).

[23]A. Di Meglio et al., *Quantum Computing for High-Energy Physics: State of the Art and Challenges. Summary of the QC4HEP Working Group*, July 2023.

[24]G. Ortiz, J. E. Gubernatis, E. Knill, and R. Laflamme, "Quantum algorithms for fermionic simulations", Phys. Rev. A **64**, 022319 (2001).

[25]A. T. Than, Y. Y. Atas, A. Chakraborty, J. Zhang, M. T. Diaz, K. Wen, X. Liu, R. Lewis, A. M. Green, C. A. Muschik, and N. M. Linke, *The phase diagram of quantum chromodynamics in one dimension on a quantum computer*, 2024.

[26]E. A. Martinez et al., "Real-time dynamics of lattice gauge theories with a few-qubit quantum computer", Nature **534**, 516–519 (2016).

[27]C. Kokail et al., *Self-Verifying Variational Quantum Simulation of the Lattice Schwinger Model*, 2018.

[28]N. Klco, E. F. Dumitrescu, A. J. McCaskey, T. D. Morris, R. C. Pooser, M. Sanz, E. Solano, P. Lougovski, and M. J. Savage, "Quantum-classical computation of Schwinger model dynamics using quantum computers", Phys. Rev. **A98**, 032331 (2018).

[29]H. Lamm and S. Lawrence, "Simulation of Nonequilibrium Dynamics on a Quantum Computer", Phys. Rev. Lett. **121**, 170501 (2018).

[30]A. Macridin, P. Spentzouris, J. Amundson, and R. Harnik, "Electron-Phonon Systems on a Universal Quantum Computer", Phys. Rev. Lett. **121**, 110504 (2018).

[31]N. Klco, J. R. Stryker, and M. J. Savage, "SU(2) non-Abelian gauge field theory in one dimension on digital quantum computers", Phys. Rev. D **101**, 074512 (2020).

[32]E. Gustafson, Y. Meurice, and J. Unmuth-Yockey, *Quantum simulation of scattering in the quantum Ising model*, 2019.

[33]E. Gustafson, P. Dreher, Z. Hang, and Y. Meurice, *Benchmarking quantum computers for real-time evolution of a* $(1+1)$ *field theory with error mitigation*, Oct. 2019.

[34]M. Kreshchuk, S. Jia, W. M. Kirby, G. Goldstein, J. P. Vary, and P. J. Love, *Simulating Hadronic Physics on NISQ devices using Basis Light-Front Quantization*, Nov. 2020.

[35]E. F. Dumitrescu, A. J. McCaskey, G. Hagen, G. R. Jansen, T. D. Morris, T. Papenbrock, R. C. Pooser, D. J. Dean, and P. Lougovski, "Cloud Quantum Computing of an Atomic Nucleus", Phys. Rev. Lett. **120**, 210501 (2018).

[36]A. Roggero and J. Carlson, "Linear Response on a Quantum Computer", (2018).

[37]H.-H. Lu et al., *Simulations of Subatomic Many-Body Physics on a Quantum Frequency Processor*, 2018.

[38]D. P. DiVincenzo, *Topics in quantum computers*, 1996.

[39]M. A. Nielsen and I. L. Chuang, *Quantum computation and quantum information: 10th anniversary edition* (Cambridge University Press, 2010).

[40]C. D. Bruzewicz, J. Chiaverini, R. McConnell, and J. M. Sage, "Trapped-ion quantum computing: progress and challenges", Applied Physics Reviews **6**, 10.1063/1.5088164 (2019).

[41]M. Caleffi, M. Amoretti, D. Ferrari, J. Illiano, A. Manzalini, and A. S. Cacciapuoti, "Distributed quantum computing: a survey", Computer Networks **254**, 110672 (2024).

[42]H. J. Kimble, "The quantum internet", Nature **453**, 1023–1030 (2008).

[43]C. M. Dawson and M. A. Nielsen, *The solovay-kitaev algorithm*, 2005.

[44]B. M. Terhal, "Quantum error correction for quantum memories", Rev. Mod. Phys. **87**, 307–346 (2015).

[45]J. Roffe, "Quantum error correction: an introductory guide", Contemporary Physics **60**, 226–245 (2019).

[46]*Scaling IonQ's quantum computers: the roadmap*, Dec. 2020.

[47]*The IBM Quantum Development Roadmap*, 2021.

[48]H. Neven, *Day 1 opening keynote by Hartmut Neven (quantum summer symposium 2020)*, Sept. 2020.

[49]Z. Cai, R. Babbush, S. C. Benjamin, S. Endo, W. J. Huggins, Y. Li, J. R. McClean, and T. E. O'Brien, *Quantum error mitigation*, 2022.

[50]M. Carena, H. Lamm, Y.-Y. Li, and W. Liu, *Lattice Renormalization of Quantum Simulations*, July 2021.

[51]M. Carena, H. Lamm, Y.-Y. Li, and W. Liu, *Improved Hamiltonians for Quantum Simulations*, Mar. 2022.

[52]M. Carena, H. Lamm, Y.-Y. Li, and W. Liu, "Quantum error thresholds for gauge-redundant digitizations of lattice field theories", Phys. Rev. D **110**, 054516 (2024).

[53]P. Lisboa and C. Michael, "Discrete subsets of su(3) for lattice gauge theory", Physics Letters B **113**, 303–304 (1982).

[54]A. F. Shaw, P. Lougovski, J. R. Stryker, and N. Wiebe, "Quantum Algorithms for Simulating the Lattice Schwinger Model", Quantum **4**, 306 (2020).

[55]Y. Tong, V. V. Albert, J. R. McClean, J. Preskill, and Y. Su, "Provably accurate simulation of gauge theories and bosonic systems", Quantum **6**, 816 (2022).

[56]Y. Ji, H. Lamm, and S. Zhu (NuQS), "Gluon Field Digitization via Group Space Decimation for Quantum Computers", Phys. Rev. D **102**, 114513 (2020).

[57]M. Carena, E. J. Gustafson, H. Lamm, Y.-Y. Li, and W. Liu, "Gauge theory couplings on anisotropic lattices", Phys. Rev. D **106**, 114504 (2022).

[58]C. W. Bauer, I. D'Andrea, M. Freytsis, and D. M. Grabowska, *A new basis for Hamiltonian SU(2) simulations*, July 2023.

[59]A. N. Ciavarella, *Quantum Simulation of Lattice QCD with Improved Hamiltonians*, July 2023.

[60]M. Hanada, J. Liu, E. Rinaldi, and M. Tezuka, *Estimating truncation effects of quantum bosonic systems using sampling algorithms*, Dec. 2022.

[61]Y. Ji, H. Lamm, and S. Zhu (NuQS), "Gluon digitization via character expansion for quantum computers", Phys. Rev. D **107**, 114503 (2023).

[62]P. Jordan and E. P. Wigner, "About the Pauli exclusion principle", Z. Phys. **47**, 631–651 (1928).

[63]S. Bravyi and A. Y. Kitaev, "Fermionic quantum computation", Annals of Physics **298**, 210–226 (2002).

[64]Y.-A. Chen and A. Kapustin, "Bosonization in three spatial dimensions and a 2-form gauge theory", Phys. Rev. B **100**, 245127 (2019).

[65]C. Muschik, M. Heyl, E. Martinez, T. Monz, P. Schindler, B. Vogell, M. Dalmonte, P. Hauke, R. Blatt, and P. Zoller, "U(1) Wilson lattice gauge theories in digital quantum simulators", New J. Phys. **19**, 103020 (2017).

[66]E. Zohar and J. I. Cirac, "Eliminating fermionic matter fields in lattice gauge theories", Phys. Rev. B **98**, 075119 (2018).

[67]E. Zohar and J. I. Cirac, "Removing Staggered Fermionic Matter in $U(N)$ and $SU(N)$ Lattice Gauge Theories", Phys. Rev. D **99**, 114511 (2019).

[68]J. Kogut and L. Susskind, "Hamiltonian formulation of Wilson's lattice gauge theories", Phys. Rev. D **11**, 395–408 (1975).

[69]S. P. Jordan, K. S. M. Lee, and J. Preskill, "Quantum Algorithms for Quantum Field Theories", Science **336**, 1130–1133 (2012).

[70]S. P. Jordan, K. S. M. Lee, and J. Preskill, "Quantum Computation of Scattering in Scalar Quantum Field Theories", Quant. Inf. Comput. **14**, 1014 (2014).

[71]L. García-Álvarez, J. Casanova, A. Mezzacapo, I. L. Egusquiza, L. Lamata, G. Romero, and E. Solano, "Fermion-Fermion Scattering in Quantum Field Theory with Superconducting Circuits", Phys. Rev. Lett. **114**, 070502 (2015).

[72]S. P. Jordan, K. S. M. Lee, and J. Preskill, *Quantum Algorithms for Fermionic Quantum Field Theories*, 2014.

[73]A. Hamed Moosavian and S. Jordan, "Faster Quantum Algorithm to simulate Fermionic Quantum Field Theory", Phys. Rev. **A98**, 012332 (2018).

[74]J. Bender, E. Zohar, A. Farace, and J. I. Cirac, "Digital quantum simulation of lattice gauge theories in three spatial dimensions", New J. Phys. **20**, 093001 (2018).

[75]J. Haah, M. B. Hastings, R. Kothari, and G. H. Low, *Quantum algorithm for simulating real time evolution of lattice Hamiltonians*, 2018.

[76]W. Du, J. P. Vary, X. Zhao, and W. Zuo, *Quantum Simulation of Nuclear Inelastic Scattering*, June 2020.

[77]A. M. Childs, Y. Su, M. C. Tran, N. Wiebe, and S. Zhu, "Theory of Trotter error with commutator scaling", Phys. Rev. X **11**, 011020 (2021).

[78]D. Coppersmith, *An approximate fourier transform useful in quantum factoring*, 2002.

[79]P. W. Shor, "Polynomial-time algorithms for prime factorization and discrete logarithms on a quantum computer", SIAM Journal on Computing **26**, 1484–1509 (1997).

[80]M. Pueschel, M. Roetteler, and T. Beth, *Fast quantum fourier transforms for a class of non-abelian groups*, 1998.

[81]E. M. Murairi, M. S. Alam, H. Lamm, S. Hadfield, and E. Gustafson, "Highly-efficient quantum fourier transformations for certain non-abelian groups", Phys. Rev. D **110**, 074501 (2024).

[82]H. Lamm, S. Lawrence, and Y. Yamauchi (NuQS), "General Methods for Digital Quantum Simulation of Gauge Theories", Phys. Rev. **D100**, 034518 (2019).

[83]X.-Q. Luo, S.-H. Guo, H. Kroger, and D. Schutte, "Improved lattice gauge field Hamiltonian", Phys. Rev. D **59**, 034503 (1999).

[84]J. Carlsson and B. H. McKellar, "Direct improvement of Hamiltonian lattice gauge theory", Phys. Rev. D **64**, 094503 (2001).

[85]E. Campbell, "Random compiler for fast Hamiltonian simulation", Phys. Rev. Lett. **123**, 070503 (2019).

[86]C. Cirstoiu, Z. Holmes, J. Iosue, L. Cincio, P. J. Coles, and A. Sornborger, "Variational fast forwarding for quantum simulation beyond the coherence time", npj Quantum Information **6**, 1–10 (2020).

[87]J. Gibbs, K. Gili, Z. Holmes, B. Commeau, A. Arrasmith, L. Cincio, P. J. Coles, and A. Sornborger, *Long-time simulations with high fidelity on quantum hardware*, 2021.

[88]Y.-X. Yao, N. Gomes, F. Zhang, T. Iadecola, C.-Z. Wang, K.-M. Ho, and P. P. Orth, "Adaptive variational quantum dynamics simulations", arXiv preprint arXiv:2011.00622 (2020).

[89]D. W. Berry, A. M. Childs, R. Cleve, R. Kothari, and R. D. Somma, "Simulating Hamiltonian dynamics with a truncated Taylor series", Phys. Rev. Lett. **114**, 090502 (2015).

[90]G. H. Low and I. L. Chuang, "Hamiltonian Simulation by Qubitization", Quantum **3**, 163 (2019).

[91]A. Peruzzo, J. McClean, P. Shadbolt, M.-H. Yung, X.-Q. Zhou, P. J. Love, A. Aspuru-Guzik, and J. L. O'brien, "A variational eigenvalue solver on a photonic quantum processor", Nature communications **5**, 4213 (2014).

[92]E. Farhi, J. Goldstone, S. Gutmann, and M. Sipser, "Quantum computation by adiabatic evolution", arXiv preprint quant-ph/0001106 (2000).

[93]E. Farhi, J. Goldstone, S. Gutmann, J. Lapan, A. Lundgren, and D. Preda, "A quantum adiabatic evolution algorithm applied to random instances of an np-complete problem", Science **292**, 472–475 (2001).

[94]D. S. Abrams and S. Lloyd, "A Quantum algorithm providing exponential speed increase for finding eigenvalues and eigenvectors", Phys. Rev. Lett. **83**, 5162–5165 (1999).

[95]N. Wiebe and C. Granade, "Efficient bayesian phase estimation", Phys. Rev. Lett. **117**, 010503 (2016).

[96]D. B. Kaplan, N. Klco, and A. Roggero, *Ground States via Spectral Combing on a Quantum Computer*, 2017.

[97]L. Lin and Y. Tong, "Near-optimal ground state preparation", Quantum **4**, 372 (2020).

[98]L. W. Anderson, M. Kiffner, T. O'Leary, J. Crain, and D. Jaksch, "Solving lattice gauge theories using the quantum Krylov algorithm and qubitization", Quantum **9**, 1669 (2025).

[99]E. Bilgin and S. Boixo, "Preparing Thermal States of Quantum Systems by Dimension Reduction", Physical Review Letters **105**, 170405, 170405 (2010).

[100]S. Harmalkar, H. Lamm, and S. Lawrence (NuQS), *Quantum Simulation of Field Theories Without State Preparation*, Jan. 2020.

[101]E. J. Gustafson and H. Lamm, "Toward quantum simulations of $\mathbb{Z}_2$ gauge theory without state preparation", Phys. Rev. D **103**, 054507 (2021).

[102]N. Klco and M. J. Savage, *Minimally-Entangled State Preparation of Localized Wavefunctions on Quantum Computers*, 2019.

[103]G. Clemente et al. (QuBiPF), "Quantum computation of thermal averages in the presence of a sign problem", Phys. Rev. D **101**, 074510 (2020).

[104]M. Motta, C. Sun, A. T. Tan, M. J. O'Rourke, E. Ye, A. J. Minnich, F. G. Brandao, and G. K.-L. Chan, "Determining eigenstates and thermal states on a quantum computer using quantum imaginary time evolution", Nature Physics **16**, 205–210 (2020).

[105]W. A. de Jong, K. Lee, J. Mulligan, M. Płoskoń, F. Ringer, and X. Yao, *Quantum simulation of non-equilibrium dynamics and thermalization in the Schwinger model*, June 2021.

[106]F. G. S. L. Brandao and M. J. Kastoryano, "Finite correlation length implies efficient preparation of quantum thermal states", ArXiv e-prints **365**, 1–16 (2016).

[107]A. Ciavarella, "Algorithm for quantum computation of particle decays", Phys. Rev. D **102**, 094505 (2020).

[108]J. S. Pedernales, R. Di Candia, I. L. Egusquiza, J. Casanova, and E. Solano, "Efficient quantum algorithm for computing n-time correlation functions", Phys. Rev. Lett. **113**, 020505 (2014).

[109]G. Ortiz, J. E. Gubernatis, E. Knill, and R. Laflamme, "Quantum algorithms for fermionic simulations", Phys. Rev. **A64**, 022319 (2001).

[110]K. Stannigel, P. Hauke, D. Marcos, M. Hafezi, S. Diehl, M. Dalmonte, and P. Zoller, "Constrained dynamics via the Zeno effect in quantum simulation: Implementing non-Abelian lattice gauge theories with cold atoms", Phys. Rev. Lett. **112**, 120406 (2014).

[111]J. R. Stryker, "Oracles for Gauss's law on digital quantum computers", Phys. Rev. **A99**, 042301 (2019).

[112]J. C. Halimeh and P. Hauke, *Reliability of lattice gauge theories*, Dec. 2019.

[113]H. Lamm, S. Lawrence, and Y. Yamauchi (NuQS), *Suppressing Coherent Gauge Drift in Quantum Simulations*, May 2020.

[114]M. C. Tran, Y. Su, D. Carney, and J. M. Taylor, "Faster digital quantum simulation by symmetry protection", PRX Quantum **2**, 010323 (2021).

[115]J. C. Halimeh, H. Lang, J. Mildenberger, Z. Jiang, and P. Hauke, *Gauge-Symmetry Protection Using Single-Body Terms*, July 2020.

[116]J. C. Halimeh and P. Hauke, *Staircase prethermalization and constrained dynamics in lattice gauge theories*, Apr. 2020.

[117]J. C. Halimeh, V. Kasper, and P. Hauke, *Fate of Lattice Gauge Theories Under Decoherence*, Sept. 2020.

[118]J. C. Halimeh, R. Ott, I. P. McCulloch, B. Yang, and P. Hauke, "Robustness of gauge-invariant dynamics against defects in ultracold-atom gauge theories", Phys. Rev. Res. **2**, 033361 (2020).

[119]M. Van Damme, J. C. Halimeh, and P. Hauke, *Gauge-Symmetry Violation Quantum Phase Transition in Lattice Gauge Theories*, Oct. 2020.

[120]V. Kasper, T. V. Zache, F. Jendrzejewski, M. Lewenstein, and E. Zohar, *Non-Abelian gauge invariance from dynamical decoupling*, Dec. 2020.

[121]J. C. Halimeh, H. Lang, and P. Hauke, *Gauge protection in non-Abelian lattice gauge theories*, June 2021.

[122]K. Osterwalder and R. Schrader, "Axioms for Euclidean Green's Functions", Commun. Math. Phys. **31**, 83–112 (1973).

[123]K. Osterwalder and R. Schrader, "Axioms for Euclidean Green's Functions. 2.", Commun. Math. Phys. **42**, 281 (1975).

[124]M. Luscher and P. Weisz, "Definition and General Properties of the Transfer Matrix in Continuum Limit Improved Lattice Gauge Theories", Nucl. Phys. **B240**, 349–361 (1984).

[125]M. Giordano and E. Meggiolaro, "A Nonperturbative foundation of the Euclidean-Minkowskian duality of Wilson-loop correlation functions", Phys. Lett. B **675**, 123–132 (2009).

[126]M. Giordano, "Renormalization of gauge theories on general anisotropic lattices and high-energy scattering in QCD", Phys. Rev. D **92**, 034514 (2015).

[127]G. Rossi and M. Testa, "Euclidean versus Minkowski short distance", Phys. Rev. **D98**, 054028 (2018).

[128]R. A. Briceño, M. T. Hansen, and C. J. Monahan, "Role of the Euclidean signature in lattice calculations of quasidistributions and other nonlocal matrix elements", Phys. Rev. **D96**, 014502 (2017).

[129]H. Hoshina, H. Fujii, and Y. Kikukawa, "Schwinger-Keldysh formalism for Lattice Gauge Theories", PoS **LATTICE2019**, 190 (2020).

[130]M. Jarrell and J. E. Gubernatis, "Bayesian inference and the analytic continuation of imaginary-time quantum Monte Carlo data", Phys. Rept. **269**, 133–195 (1996).

[131]H. B. Meyer, "Transport Properties of the Quark-Gluon Plasma: A Lattice QCD Perspective", Eur. Phys. J. A **47**, 86 (2011).

[132]Y. Burnier and A. Rothkopf, "Bayesian Approach to Spectral Function Reconstruction for Euclidean Quantum Field Theories", Phys. Rev. Lett. **111**, 182003 (2013).

[133]J. M. Pawlowski and A. Rothkopf, "Improved real-time dynamics from imaginary frequency lattice simulations", EPJ Web Conf. **175**, edited by M. Della Morte, P. Fritzsch, E. Gámiz Sánchez, and C. Pena Ruano, 07001 (2018).

[134]R.-A. Tripolt, P. Gubler, M. Ulybyshev, and L. Von Smekal, "Numerical analytic continuation of Euclidean data", Comput. Phys. Commun. **237**, 129–142 (2019).

[135]J. Bulava and M. T. Hansen, "Scattering amplitudes from finite-volume spectral functions", Phys. Rev. D **100**, 034521 (2019).

[136]J. Karpie, K. Orginos, A. Rothkopf, and S. Zafeiropoulos, "Reconstructing parton distribution functions from Ioffe time data: from Bayesian methods to Neural Networks", JHEP **04**, 057 (2019).

[137]M. Bruno and M. T. Hansen, *Variations on the Maiani-Testa approach and the inverse problem*, Dec. 2020.

[138]M. Asakawa, T. Hatsuda, and Y. Nakahara, "Maximum entropy analysis of the spectral functions in lattice QCD", Prog. Part. Nucl. Phys. **46**, 459–508 (2001).

[139]K. Sasaki, S. Sasaki, and T. Hatsuda, "Spectral analysis of excited nucleons in lattice QCD with maximum entropy method", Phys. Lett. B **623**, 208–217 (2005).

[140]M. Creutz, *Quarks, gluons and lattices*, Cambridge Monographs on Mathematical Physics (Cambridge Univ. Press, Cambridge, UK, June 1985).

[141]M. Luscher, "Construction of a Selfadjoint, Strictly Positive Transfer Matrix for Euclidean Lattice Gauge Theories", Commun. Math. Phys. **54**, 283 (1977).

[142]D. Harlow and H. Ooguri, *Symmetries in quantum field theory and quantum gravity*, 2018.

[143]N. E. Ligterink, N. R. Walet, and R. F. Bishop, "Towards a many body treatment of Hamiltonian lattice SU(N) gauge theory", Annals Phys. **284**, 215–262 (2000).

[144]J. A. L. McIntosh and L. C. L. Hollenberg, "Reaching the continuum limit in lattice gauge theory: Without a computer", Phys. Lett. B **538**, 207–212 (2002).

[145]A. Wichmann, D. Schutte, B. C. Metsch, and V. Wethkamp, "The Coupled cluster method in Hamiltonian lattice field theory: SU(2) glueballs", Phys. Rev. D **65**, 094511 (2002).

[146]J.-Q. Jiang, "0^{++} glueball wave function for improved SU(2) lattice gauge theory in (2+1) dimensions", Phys. Rev. D **86**, 034504 (2012).

[147]M. Beccaria, "Wave functions for SU(2) Hamiltonian lattice gauge theory", Phys. Rev. D **62**, 034510 (2000).

[148]J. Carlsson, J. A. L. McIntosh, B. H. J. McKellar, and L. C. L. Hollenberg, "An Analytic variational study of the mass spectrum in (2+1)-dimensional SU(3) Hamiltonian lattice gauge theory", Phys. Rev. D **67**, 114509 (2003).

[149]J. Carlsson and B. H. J. McKellar, "SU(N) glueball masses in (2+1)-dimensions", Phys. Rev. D **68**, 074502 (2003).

[150]J. Carlsson and B. H. J. McKellar, *SU(N) lattice gauge theory on a single cube*, Mar. 2003.

[151]J. R. Hiller, "Nonperturbative light-front Hamiltonian methods", Prog. Part. Nucl. Phys. **90**, 75–124 (2016).

[152]E. H. Fradkin and S. H. Shenker, "Phase Diagrams of Lattice Gauge Theories with Higgs Fields", Phys. Rev. D **19**, 3682–3697 (1979).

[153]D. Horn, M. Weinstein, and S. Yankielowicz, "Hamiltonian Approach to Z(N) Lattice Gauge Theories", Phys. Rev. D **19**, 3715 (1979).

[154]D. C. Hackett, K. Howe, C. Hughes, W. Jay, E. T. Neil, and J. N. Simone, "Digitizing Gauge Fields: Lattice Monte Carlo Results for Future Quantum Computers", Phys. Rev. A **99**, 062341 (2019).

[155]A. Alexandru, P. F. Bedaque, S. Harmalkar, H. Lamm, S. Lawrence, and N. C. Warrington (NuQS), "Gluon field digitization for quantum computers", Phys.Rev.D **100**, 114501 (2019).

[156]C. Morningstar and M. J. Peardon, "SU(3) glueballs on coarse, anisotropic lattices", Nucl. Phys. B Proc. Suppl. **53**, edited by C. Bernard, M. Golterman, M. Ogilvie, and J. Potvin, 917–920 (1997).

[157]T. M. R. Byrnes, M. Loan, C. J. Hamer, F. D. R. Bonnet, D. B. Leinweber, A. G. Williams, and J. M. Zanotti, "The Hamiltonian limit of (3+1)-D SU(3) lattice gauge theory on anisotropic lattices", Phys. Rev. D **69**, 074509 (2004).

[158]N. Bralic and L. Vergara, "Modeling High Temperatures on the Lattice", J. Phys. G **16**, 1805–1812 (1990).

[159]A. Hasenfratz and P. Hasenfratz, "The Scales of Euclidean and Hamiltonian Lattice QCD", Nucl. Phys. B **193**, 210 (1981).

[160]F. Karsch, "SU(N) Gauge Theory Couplings on Asymmetric Lattices", Nucl. Phys. B **205**, 285–300 (1982).

[161]C. Hamer, "Scales of Euclidean and Hamiltonian lattice gauge theory in three-dimensions", Phys. Rev. D **53**, 7316–7320 (1996).

[162]C. Morningstar, "Improved gluonic actions on anisotropic lattices", Nucl. Phys. B Proc. Suppl. **53**, edited by C. Bernard, M. Golterman, M. Ogilvie, and J. Potvin, 914–916 (1997).

[163]C. J. Morningstar and M. J. Peardon, "Efficient glueball simulations on anisotropic lattices", Phys. Rev. D **56**, 4043–4061 (1997).

[164]M. G. Alford, I. T. Drummond, R. R. Horgan, H. Shanahan, and M. J. Peardon, "Measuring the aspect ratio renormalization of anisotropic-lattice gluons", Phys. Rev. D **63**, 074501 (2001).

[165]T. R. Klassen, "The Anisotropic Wilson gauge action", Nucl. Phys. B **533**, 557–575 (1998).

[166]Y. Chen et al., "Glueball spectrum and matrix elements on anisotropic lattices", Phys. Rev. **D73**, 014516 (2006).

[167]Lüscher, Martin, "Properties and uses of the Wilson flow in lattice QCD", JHEP **08**, [Erratum: JHEP03,092(2014)], 071 (2010).

[168]S. Borsanyi, S. Durr, Z. Fodor, S. D. Katz, S. Krieg, T. Kurth, S. Mages, A. Schafer, and K. K. Szabo, *Anisotropy tuning with the Wilson flow*, May 2012.

[169]G. Kanwar and M. L. Wagman, *Real-time lattice gauge theory actions: unitarity, convergence, and path integral contour deformations*, Mar. 2021.

[170]P. Menotti and E. Onofri, "The Action of SU(N) Lattice Gauge Theory in Terms of the Heat Kernel on the Group Manifold", Nucl. Phys. B **190**, 288–300 (1981).

[171]K. Miller, "Least squares methods for ill-posed problems with a prescribed bound", SIAM Journal on Mathematical Analysis **1**, 52–74 (1970).

[172]F. L. Bauer and C. T. Fike, "Norms and exclusion theorems", Numerische Mathematik **2**, 137–141 (1960).

[173]A. C. Santos, "The ibm quantum computer and the ibm quantum experience", Revista Brasileira de Ensino de Física **39** (2017).

[174]A. W. Cross, L. S. Bishop, J. A. Smolin, and J. M. Gambetta, "Open quantum assembly language", arXiv preprint arXiv:1707.03429 (2017).

[175]Y. Nam, J.-S. Chen, N. C. Pisenti, K. Wright, C. Delaney, D. Maslov, K. R. Brown, S. Allen, J. M. Amini, J. Apisdorf, et al., "Ground-state energy estimation of the water molecule on a trapped ion quantum computer", arXiv preprint arXiv:1902.10171 (2019).

[176]F. Arute et al., "Quantum supremacy using a programmable superconducting processor", Nature **574**, 505–510 (2019).

[177]F. Arute et al., "Hartree-fock on a superconducting qubit quantum computer", Science **369**, 1084–1089 (2020).

[178]S. Lawrence, *A Puzzle: Gauge Theory on a Quantum Computer*, 2021.

[179]C. Christou, A. Feo, H. Panagopoulos, and E. Vicari, "The three loop β-function of $SU(N)$ lattice gauge theories with Wilson fermions", Nucl. Phys. B **525**, [Erratum: Nucl.Phys.B 608, 479–480 (2001)], 387–400 (1998).

[180]F. Casas and A. Murua, "An efficient algorithm for computing the baker–campbell–hausdorff series and some of its applications", Journal of Mathematical Physics **50**, 033513 (2009).

[181]C. Charles, E. J. Gustafson, E. Hardt, F. Herren, N. Hogan, H. Lamm, S. Starecheski, R. S. V. de Water, and M. L. Wagman, *Simulating $\mathbb{Z}_2$ lattice gauge theory on a quantum computer*, 2023.

[182]C. F. Groß, S. Romiti, L. Funcke, K. Jansen, A. Kan, S. Kühn, and C. Urbach, *Matching lagrangian and hamiltonian simulations in (2+1)-dimensional u(1) gauge theory*, 2025.

[183]K. Symanzik, "Continuum Limit and Improved Action in Lattice Theories. 1. Principles and phi**4 Theory", Nucl. Phys. B **226**, 187–204 (1983).

[184]M. Luscher and P. Weisz, "On-Shell Improved Lattice Gauge Theories", Commun. Math. Phys. **97**, [Erratum: Commun. Math. Phys.98,433(1985)], 59 (1985).

[185]M. Luscher and P. Weisz, "Computation of the Action for On-Shell Improved Lattice Gauge Theories at Weak Coupling", Phys. Lett. B **158**, 250–254 (1985).

[186]K. G. Wilson, "Confinement of quarks", Phys. Rev. D **10**, 2445–2459 (1974).

[187]G. P. Lepage, "Redesigning lattice qcd", Lecture Notes in Physics, 1–48.

[188]M. Creutz, "Gauge Fixing, the Transfer Matrix, and Confinement on a Lattice", Phys. Rev. **D15**, 1128 (1977).

[189]M. G. Alford, W. Dimm, G. P. Lepage, G. Hockney, and P. B. Mackenzie, "Lattice QCD on small computers", Phys. Lett. B **361**, 87–94 (1995).

[190]J. Carlsson, "Improvement and analytic techniques in Hamiltonian lattice gauge theory", Other thesis (Apr. 2003).

[191]E. Gustafson and R. V. de Water, *Improved fermion hamiltonians for quantum simulation*, 2024.

[192]E. Zohar, J. I. Cirac, and B. Reznik, "Quantum Simulations of Lattice Gauge Theories using Ultracold Atoms in Optical Lattices", Rept. Prog. Phys. **79**, 014401 (2016).

[193]K. Wei, E. Magesan, I. Lauer, S. Srinivasan, D. Bogorin, S. Carnevale, G. Keefe, Y. Kim, D. Klaus, W. Landers, et al., *Quantum crosstalk cancellation for fast entangling gates and improved multi-qubit performance*, June 2021.

[194]L. Lao, A. Korotkov, Z. Jiang, W. Mruczkiewicz, T. E. O'Brien, and D. E. Browne, *Software mitigation of coherent two-qubit gate errors*, Nov. 2021.

[195]L. Howe, M. Castellanos-Beltran, A. J. Sirois, D. Olaya, J. Biesecker, P. D. Dresselhaus, S. P. Benz, and P. F. Hopkins, *Digital control of a superconducting qubit using a Josephson pulse generator at 3 K*, Nov. 2021.

[196]M. S. Alam, S. Hadfield, H. Lamm, and A. C. Y. Li (SQMS), "Primitive quantum gates for dihedral gauge theories", Phys. Rev. D **105**, 114501 (2022).

[197]E. Zohar and M. Burrello, "Formulation of lattice gauge theories for quantum simulations", Phys. Rev. **D91**, 054506 (2015).

[198]A. F. Izmaylov, "On construction of projection operators", The Journal of Physical Chemistry A **123**, 3429–3433 (2019).

[199]I. L. Chuang and M. A. Nielsen, "Prescription for experimental determination of the dynamics of a quantum black box", J. Mod. Opt. **44**, 2455 (1997).

[200]A. Erhard, J. J. Wallman, L. Postler, M. Meth, R. Stricker, E. A. Martinez, P. Schindler, T. Monz, J. Emerson, and R. Blatt, "Characterizing large-scale quantum computers via cycle benchmarking", Nature Communications **10**, 5347 (2019).

[201]Y. Li and S. C. Benjamin, "Efficient variational quantum simulator incorporating active error minimization", Physical Review X **7**, 021050 (2017).

[202]S. Endo, S. C. Benjamin, and Y. Li, "Practical quantum error mitigation for near-future applications", Physical Review X **8**, 10.1103/physrevx.8.031027 (2018).

[203]M. R. Geller and Z. Zhou, "Efficient error models for fault-tolerant architectures and the pauli twirling approximation", Physical Review A **88**, 10.1103/physreva.88.012314 (2013).

[204]J. J. Wallman and J. Emerson, "Noise tailoring for scalable quantum computation via randomized compiling", Physical Review A **94**, 10.1103/physreva.94.052325 (2016).

[205]K. Yeter-Aydeniz, Z. Parks, A. Nair, E. Gustafson, A. F. Kemper, R. C. Pooser, Y. Meurice, and P. Dreher, *Measuring NISQ Gate-Based Qubit Stability Using a 1+1 Field Theory and Cycle Benchmarking*, Jan. 2022.

[206]*IBM's roadmap for building an open quantum software ecosystem*, Feb. 2021.

[207]E. Gustafson et al., "Large scale multi-node simulations of $\mathbb{Z}_2$ gauge theory quantum circuits using Google Cloud Platform", in IEEE/ACM Second International Workshop on Quantum Computing Software (Oct. 2021).

[208]E. Zohar, A. Farace, B. Reznik, and J. I. Cirac, "Digital lattice gauge theories", Phys. Rev. **A95**, 023604 (2017).

[209]E. J. Gustafson, H. Lamm, F. Lovelace, and D. Musk, "Primitive quantum gates for an SU(2) discrete subgroup: Binary tetrahedral", Phys. Rev. D **106**, 114501 (2022).

[210]T. Hartung, T. Jakobs, K. Jansen, J. Ostmeyer, and C. Urbach, "Digitising SU(2) gauge fields and the freezing transition", Eur. Phys. J. C **82**, 237 (2022).

[211]T. Jakobs, M. Garofalo, T. Hartung, K. Jansen, J. Ostmeyer, D. Rolfes, S. Romiti, and C. Urbach, *Canonical Momenta in Digitized SU(2) Lattice Gauge Theory: Definition and Free Theory*, Apr. 2023.

[212]C. Charles, E. J. Gustafson, E. Hardt, F. Herren, N. Hogan, H. Lamm, S. Starecheski, R. S. Van de Water, and M. L. Wagman, *Simulating $\mathbb{Z}_2$ lattice gauge theory on a quantum computer*, May 2023.

[213]E. J. Gustafson, H. Lamm, and F. Lovelace, *Primitive Quantum Gates for an $SU(2)$ Discrete Subgroup: Binary Octahedral*, Dec. 2023.

[214]E. Zohar, J. I. Cirac, and B. Reznik, "Cold-Atom Quantum Simulator for SU(2) Yang-Mills Lattice Gauge Theory", Phys. Rev. Lett. **110**, 125304 (2013).

[215]E. Zohar, J. I. Cirac, and B. Reznik, "Simulating Compact Quantum Electrodynamics with ultracold atoms: Probing confinement and nonperturbative effects", Phys. Rev. Lett. **109**, 125302 (2012).

[216]H. Singh and S. Chandrasekharan, "Qubit regularization of the $O(3)$ sigma model", Phys. Rev. D **100**, 054505 (2019).

[217]H. Singh, *Qubit $O(N)$ nonlinear sigma models*, Nov. 2019.

[218]A. J. Buser, T. Bhattacharya, L. Cincio, and R. Gupta, *Quantum simulation of the qubit-regularized O(3)-sigma model*, June 2020.

[219]J. F. Haase, L. Dellantonio, A. Celi, D. Paulson, A. Kan, K. Jansen, and C. A. Muschik, *A resource efficient approach for quantum and classical simulations of gauge theories in particle physics*, June 2020.

[220]A. Alexandru, P. F. Bedaque, A. Carosso, M. J. Cervia, and A. Sheng, "Qubitization strategies for bosonic field theories", Phys. Rev. D **107**, 034503 (2023).

[221]A. Alexandru, P. F. Bedaque, A. Carosso, M. J. Cervia, E. M. Murairi, and A. Sheng, *Fuzzy Gauge Theory for Quantum Computers*, Aug. 2023.

[222]U.-J. Wiese, "Towards Quantum Simulating QCD", Nucl. Phys. **A931**, 246–256 (2014).

[223]D. Luo, J. Shen, M. Highman, B. K. Clark, B. DeMarco, A. X. El-Khadra, and B. Gadway, *A Framework for Simulating Gauge Theories with Dipolar Spin Systems*, Dec. 2019.

[224]R. C. Brower, D. Berenstein, and H. Kawai, "Lattice Gauge Theory for a Quantum Computer", PoS **LATTICE2019**, 112 (2019).

[225]S. V. Mathis, G. Mazzola, and I. Tavernelli, "Toward scalable simulations of Lattice Gauge Theories on quantum computers", Phys. Rev. D **102**, 094501 (2020).

[226]J. C. Halimeh, M. Aidelsburger, F. Grusdt, P. Hauke, and B. Yang, *Cold-atom quantum simulators of gauge theories*, Oct. 2023.

[227]E. Zohar, J. I. Cirac, and B. Reznik, "Quantum simulations of gauge theories with ultracold atoms: local gauge invariance from angular momentum conservation", Phys. Rev. **A88**, 023617 (2013).

[228]D. B. Kaplan and J. R. Stryker, "Gauss's law, duality, and the hamiltonian formulation of u(1) lattice gauge theory", Phys. Rev. D **102**, 094515 (2020).

[229]J. Bender and E. Zohar, "Gauge redundancy-free formulation of compact qed with dynamical matter for quantum and classical computations", Phys. Rev. D **102**, 114517 (2020).

[230]A. Yamamoto, "Real-time simulation of (2+1)-dimensional lattice gauge theory on qubits", PTEP **2021**, 013B06 (2021).

[231]C. W. Bauer and D. M. Grabowska, *Efficient Representation for Simulating U(1) Gauge Theories on Digital Quantum Computers at All Values of the Coupling*, Nov. 2021.

[232]D. M. Grabowska, C. Kane, B. Nachman, and C. W. Bauer, *Overcoming exponential scaling with system size in Trotter-Suzuki implementations of constrained Hamiltonians: 2+1 U(1) lattice gauge theories*, Aug. 2022.

[233]C. Kane, D. M. Grabowska, B. Nachman, and C. W. Bauer, *Efficient quantum implementation of 2+1 U(1) lattice gauge theories with Gauss law constraints*, Nov. 2022.

[234]D. Paulson, L. Dellantonio, J. F. Haase, A. Celi, A. Kan, A. Jena, C. Kokail, R. van Bijnen, K. Jansen, P. Zoller, and C. A. Muschik, "Simulating 2d effects in lattice gauge theories on a quantum computer", PRX Quantum **2**, 030334 (2021).

[235]A. N. Ciavarella and C. W. Bauer, *Quantum Simulation of SU(3) Lattice Yang Mills Theory at Leading Order in Large N*, Feb. 2024.

[236]M. Kreshchuk, S. Jia, W. M. Kirby, G. Goldstein, J. P. Vary, and P. J. Love, *Light-Front Field Theory on Current Quantum Computers*, Sept. 2020.

[237]A. Ciavarella, N. Klco, and M. J. Savage, *A Trailhead for Quantum Simulation of SU(3) Yang-Mills Lattice Gauge Theory in the Local Multiplet Basis*, Jan. 2021.

[238]T. V. Zache, D. González-Cuadra, and P. Zoller, *Quantum and classical spin network algorithms for q-deformed Kogut-Susskind gauge theories*, Apr. 2023.

[239]T. Hayata and Y. Hidaka, *Breaking new ground for quantum and classical simulations of* SU(3) *Yang-Mills theory*, June 2023.

[240]E. Zohar and B. Reznik, "Confinement and lattice QED electric flux-tubes simulated with ultracold atoms", Phys. Rev. Lett. **107**, 275301 (2011).

[241]D. Banerjee, M. Bögli, M. Dalmonte, E. Rico, P. Stebler, U. .-. Wiese, and P. Zoller, "Atomic Quantum Simulation of U(N) and SU(N) Non-Abelian Lattice Gauge Theories", Phys. Rev. Lett. **110**, 125303 (2013).

[242]L. Tagliacozzo, A. Celi, P. Orland, and M. Lewenstein, "Simulations of non-Abelian gauge theories with optical lattices", Nature Commun. **4**, 2615 (2013).

[243]I. Raychowdhury and J. R. Stryker, "Solving gauss's law on digital quantum computers with loop-string-hadron digitization", Phys. Rev. Res. **2**, 033039 (2020).

[244]F. M. Surace, P. P. Mazza, G. Giudici, A. Lerose, A. Gambassi, and M. Dalmonte, "Lattice gauge theories and string dynamics in Rydberg atom quantum simulators", Phys. Rev. X **10**, 021041 (2020).

[245]Z. Davoudi, I. Raychowdhury, and A. Shaw, *Search for Efficient Formulations for Hamiltonian Simulation of non-Abelian Lattice Gauge Theories*, Sept. 2020.

[246]T. Bhattacharya, A. J. Buser, S. Chandrasekharan, R. Gupta, and H. Singh, *Qubit regularization of asymptotic freedom*, Dec. 2020.

[247]J. Zhou, H. Singh, T. Bhattacharya, S. Chandrasekharan, and R. Gupta, "Spacetime symmetric qubit regularization of the asymptotically free two-dimensional O(4) model", Phys. Rev. D **105**, 054510 (2022).

[248]S. Caspar and H. Singh, "From Asymptotic Freedom to θ Vacua: Qubit Embeddings of the O(3) Nonlinear σ Model", Phys. Rev. Lett. **129**, 022003 (2022).

[249]E. Mathew and I. Raychowdhury, "Protecting local and global symmetries in simulating (1+1)D non-Abelian gauge theories", Phys. Rev. D **106**, 054510 (2022).

[250]M. Van Damme, J. Mildenberger, F. Grusdt, P. Hauke, and J. C. Halimeh, *Suppressing nonperturbative gauge errors in the thermodynamic limit using local pseudogenerators*, Oct. 2021.

[251]J. C. Halimeh and P. Hauke, "Stabilizing Gauge Theories in Quantum Simulators: A Brief Review", in (Apr. 2022).

[252]S. Lieu, R. Belyansky, J. T. Young, R. Lundgren, V. V. Albert, and A. V. Gorshkov, "Symmetry breaking and error correction in open quantum systems", Phys. Rev. Lett. **125**, 240405 (2020).

[253]C. Bonati, A. Pelissetto, and E. Vicari, "Breaking of Gauge Symmetry in Lattice Gauge Theories", Phys. Rev. Lett. **127**, 091601 (2021).

[254]C. Bonati, A. Pelissetto, and E. Vicari, "Lattice gauge theories in the presence of a linear gauge-symmetry breaking", Phys. Rev. E **104**, 014140 (2021).

[255]E. J. Gustafson and H. Lamm, *Robustness of Gauge Digitization to Quantum Noise*, Jan. 2023.

[256]J. C. Halimeh and P. Hauke, "Reliability of lattice gauge theories", Physical Review Letters **125**, `10.1103/physrevlett.125.030503` (2020).

[257]A. Rajput, A. Roggero, and N. Wiebe, "Quantum error correction with gauge symmetries", npj Quantum Information **9**, 41 (2023).

[258]N. Klco and M. J. Savage, "Hierarchical qubit maps and hierarchically implemented quantum error correction", Phys. Rev. A **104**, 062425 (2021).

[259]A. Rajput, A. Roggero, and N. Wiebe, "Quantum error correction with gauge symmetries", npj Quantum Inf. **9**, 41 (2023).

[260]J. del Pino and O. Zilberberg, "Dynamical Gauge Fields with Bosonic Codes", Phys. Rev. Lett. **130**, 171901 (2023).

[261]A. J. Landahl and B. C. A. Morrison, *Logical fermions for fault-tolerant quantum simulation*, Oct. 2021.

[262]Y.-A. Chen, A. V. Gorshkov, and Y. Xu, *Error-correcting codes for fermionic quantum simulation*, 2022.

[263]P. W. Shor, *Fault tolerant quantum computation*, May 1996.

[264]D. Aharonov and M. Ben-Or, "Fault-tolerant quantum computation with constant error rate", SIAM Journal on Computing **38**, 1207–1282 (2008).

[265]E. Knill, R. Laflamme, and W. H. Zurek, "Resilient quantum computation", Science **279**, 342–345 (1998).

[266]N. Bao, C. Cao, A. Chatwin-Davies, G. Cheng, and G. Zhu, *Superselection rules, quantum error correction, and quantum chromodynamics*, 2023.

[267]J. Carlsson and B. H. J. McKellar, "Direct improvement of hamiltonian lattice gauge theory", Phys. Rev. D **64**, 094503 (2001).

[268]M. Carena, H. Lamm, Y.-Y. Li, and W. Liu, "Improved hamiltonians for quantum simulations of gauge theories", Phys. Rev. Lett. **129**, 051601 (2022).

[269]C. Gattringer and C. B. Lang, *Quantum chromodynamics on the lattice*, Vol. 788 (Springer, Berlin, 2010).

[270]N. Ligterink, N. Walet, and R. Bishop, "Toward a many-body treatment of hamiltonian lattice SU(n) gauge theory", Annals of Physics **284**, 215–262 (2000).

[271]V. Müller and W. Rühl, "The energy gap of su(2) lattice gauge theory in 2+1 dimensions", Nuclear Physics B **230**, 49–61 (1984).

[272]J. B. Bronzan, "Explicit hamiltonian for su(2) lattice gauge theory", Phys. Rev. D **31**, 2020–2028 (1985).

[273]Z. Cai, R. Babbush, S. C. Benjamin, S. Endo, W. J. Huggins, Y. Li, J. R. McClean, and T. E. O'Brien, *Quantum error mitigation*, 2023.

[274]E. Knill and R. Laflamme, "Theory of quantum error-correcting codes", Phys. Rev. A **55**, 900–911 (1997).

[275]P. M. van Den Broek and J. F. Cornwell, "Clebsch-gordan coefficients of symmetry groups", physica status solidi (b) **90**, 211–224 (1978).

[276]P. Butera and M. Pernici, *Sums of permanental minors using Grassmann algebra*, June 2014.